NICOLÁS GUARÍN-ZAPATA

WAVE PROPAGATION IN PERIODIC MATERIALS WITH GENERALIZED CONTINUA

Wave propagation in periodic materials with generalized continua

A dissertation submitted as a partial requirement for the degree of Doctor of Philosophy

Advisor: Juan David Gómez

School of Engineering, Universidad EAFIT

Contents

List of Figures

Abstract

The development in the field of architectured materials have renewed the interest in generalized continuum mechanics theories. We can identify popular examples in the area of phononic crystals and metamaterials. These are materials that, due to its designed microstructure, present mechanical properties that are unexpected at a macro-level, such as negative refraction, negative bulk moduls or negative effective-mass. From a wave propagation perspective, these materials are appealing since they present some phenomena such as dispersion, filtering, and directionality in some frequency ranges. From a physics point of view, these phenomena result from the interaction between the incident field with the microstructural elements that produce local dispersion and difraction. This work studies two generalized continuum mechanics models. One of them is based in the inclusion of additional degrees of freedom to the material point, while the other considers higher-order gradients in the deformation energy. Additionally, we present the finite element formulation for these models in the context of periodic materials. This is done through the Bloch-Floquet theorem —that allows to consider the periodicity of the material considering a single unit cell.

Keywords: Generalized continuum mechanics, Micropolar solids, Couple-stress theory, Periodic materials, Bloch analysis, Directional behavior analysis.

Preface

The present document summarizes the work on wave propagation on periodic materials under generalized continuum mechanics models. The use of generalized continua models allows having media that is inherently dispersive and that have length scales due to its microstructure. These facts made these models interesting to study within the fields of phononic crystals and metamaterials. To study wave propagation in these types of materials we need numerical techniques that allow us to obtain dispersion relations for each material model. That is why the present work focuses on the exploration of generalized continua models in the area of architected materials, particularly, for periodic composites. As such, the main goal is to extend Bloch's analysis for these types of models. In our case, we center on Micropolar elasticity and Consistent Couple Stress Theory (C-CST). Where the former model includes additional degrees of freedom at each material point, while in the latter the deformation energy depends on the curl of rotation field. The numerical method used for the purpose of Bloch's analysis is the finite element method. For this, we propose variational statements for both models and finite element formulations in two dimensions. We developed open-source routines with the micropolar and C-CST elements as part of SolidsPy, our own finite element suite.

This document has 4 chapters. In chapter 1 we propose a new method to study directional behavior of periodic materials, i.e., the dependence in wave speed with the propagation direction. Although, this method is not specific to generalized continua or elastodynamics. In chapter 2 we deal with the micropolar model. This includes deducing variational statements for periodic media using the Bloch-Floquet theorem, obtaining a finite element formulation, and showing dispersion relations for some simple composites. Chapter 3 is similar in essence to Chapter 2 in that it develops the theory for dealing with periodic materials using C-CST model with the finite element method. Hence, here we present variational statements, Bloch-Floquet theorem within the model, and dispersion relations for simple composites. In this model we need to use a different approach for the finite element formulation since higher continuity is required; we deal with this us-

ing a Lagrange multiplier approach. The final chapter presents some future research lines that might follow the present work. There are two appendices at the end of the document. One of them presents some generalities of general continuum models and specific details related to wave propagation for the micropolar an C-CST models. The last one present the software developed during the work presented here.

Each chapter in this document is self-contained and can be read independently. Hence, each chapter presents an introduction and, sometimes, a short literature review. At the end of each chapter, except chapter 1, there are some concluding remarks.

Directionality analysis for periodic materials

Introduction

There is an increasing interest in the study and design of periodic materials across disciplines [Banerjee, 2011, Joannopoulos et al., 2008, Deymier, 2013]. This interest is related to the appearance of unusual properties such as effective negative mass, negative refraction, negative Poisson equation, and acoustic/electromagnetic cloaking [Norris and Haberman, 2012, Hussein et al., 2014, Goldsberry and Haberman, 2018]. Thus, there is a trend in designing microstructures aiming to control the bulk properties [Milton and Cherkaev, 1995, Norris and Nagy, 2011, Willis, 2016, Valencia et al., 2019b, Guarín-Zapata et al., 2019]. Although direct numerical simulations, where the bulk of the material is considered and the complete microstructure is discretized are possible [Sigalas and Garcıa, 2000], the most common approach is to take advantage of the periodicity of the material and model a single cell [Pennec et al., 2010, Hussein et al., 2014]. This is achieved using Bloch's theorem [Bloch, 1929]. Bloch's theorem was originally used in solid-state physics [Brillouin, 2003, Kittel, 1996], but its use has been extended to electrodynamics [Joannopoulos et al., 2008], acoustics [Zhang and Liu, 2004, Deymier, 2013] and elastodynamics [Hussein et al., 2014, Valencia et al., 2019a, Guarín-Zapata et al., 2020].

Periodic materials are anisotropic because of discrete symmetries in their unit cells [Nye et al., 1985, Kittel, 1996, Moakher and Norris, 2006, Maurin et al., 2018]. This anisotropy behavior translates into directionality in wave propagation, i.e., the speed of waves depends on the direction of propagation. So, if we want to study the propagation of waves in a periodic material, we are interested in characterizing this directionality. Although there have been some efforts in defining descriptors that quantify the anisotropy level of materials [Zener, 1948, Kanit et al., 2006, Ranganathan and Ostoja-Starzewski, 2008], they are not perfect because they reduce all the information to a single number and do not provide information about the preferred direction of propagation or symmetries present. Guarín-Zapata et al. [Guarín-Zapata et al., 2019] used a qualitative approach to compare anisotropy

for different transversely isotropic materials and select them to tune the behavior of helicoidal composites. This was used for transversely isotropic materials, where the dispersion relations can be obtained analytically [Auld, 1973], and used to analyze a single layer of a composite. For heterogeneous materials and materials with other symmetries besides isotropy and transverse isotropy, this type of information is not available analytically and numerical simulations are required. Thus, a general tool to analyze the bulk anisotropy of materials is desired.

This work presents a method to compute a qualitative descriptor of material directionality for desired frequency ranges from dispersion (hyper-) surfaces. This starting point is a common output when using Bloch's theorem to analyze periodic materials. We start by describing some generalities of periodic materials and Bloch's theorem, which is commonly used to describe the bulk behavior using a single unit cell. Then, we describe the propagation of waves in anisotropic elastic materials in two and three dimensions. Following this section, we present the proposed method to analyze the directionality of periodic materials and present some tests for the method in analytically and numerically obtained dispersion relations. Although all the examples presented are from the field of elastodynamics this method applies to analyze the directionality for any material that uses dispersion (hyper-) surfaces as input.

Periodic materials

A periodic material is defined by the spatial repetition of a given motif in one, two, or three dimensions. The motifs refer to heterogeneities in the material properties at the microstructural level and can contain different materials, topologies, and shapes. For example, in the case of electromagnetic waves, we have *photonic crystals* and the periodicity of electric permittivity and magnetic permeability [Joannopoulos et al., 2008]. For elastic waves, the term is *phononic crystals* and we have periodicity in the stiffness and mass density of the material [Deymier, 2013]. These materials are completely described by a lattice and an elementary or unit cell. The lattice is defined by a set of base vectors, which allow the construction of the whole material applying successive translation operations [Brillouin, 2003]. To study this type of material it is common to take advantage of the periodicity of the material properties and express the solution using Bloch's theorem [Brillouin, 2003].

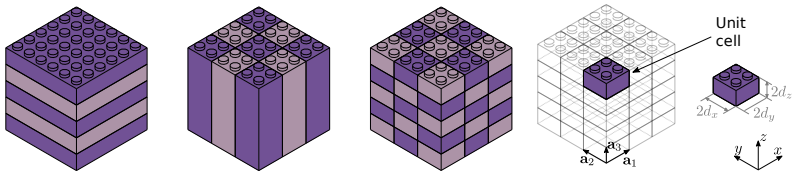

(a) (b) (c) (d)

Figure 1: 3D material with different periodicities. Regardless of the space dimensionality its periodicity could be in (a) one (b) two or (c) three space dimensions. (d) The purple lego-brick defines the fundamental unit cell which allows construction or filling of space after applying translation operations according to the lattice vector $\mathbf{a}$.

Bloch's theorem

Let us consider a generalized wave equation of the form

$$\mathcal{L}\mathbf{u}(\mathbf{x}) = -\omega^2\mathbf{u}(\mathbf{x})\,, \tag{1}$$

where $\mathcal{L}$ is a positive definite operator [1], $\mathbf{u}$ is the field of interest, and ω is the angular frequency. Bloch's theorem establishes that solutions to (1) are of the form

$$\mathbf{u}(\mathbf{x}) = \mathbf{w}(\mathbf{x})e^{i\mathbf{k}\cdot\mathbf{x}}\,, \tag{2}$$

where $\mathbf{w}(\mathbf{x})$ is a function with the same periodicity of the material. Opposite sides of the unit cell and separated by a vector $\mathbf{a}$ and, as a consequence,

$$\mathbf{u}(\mathbf{x}+\mathbf{a}) = \mathbf{u}(\mathbf{x})e^{i\mathbf{k}\cdot\mathbf{a}}\,.$$

Where $\mathbf{u}(\mathbf{x}+\mathbf{a})$ and $\mathbf{u}(\mathbf{x})$ give the field at $\mathbf{x}+\mathbf{a}$ and $\mathbf{x}$, while $\mathbf{a} = \mathbf{a}_1 n_1 + \mathbf{a}_2 n_2 + \mathbf{a}_3 n_3$ is the lattice translation vector shown in Figure 1(d). The term $e^{i\mathbf{k}\cdot\mathbf{a}}$ represents a phase shift between opposite sides of the unit cell. This relationship between opposite sides of the fundamental cell stated in the theorem through the boundary terms permits the characterization of the fundamental properties of the material with the analysis of a single cell.

Computationally, equation (1) is commonly translated to a generalized eigenvalue problem through a numerical method such as the Finite Element Method. And we end up with a system of the form

$$[K]\{\mathbf{U}\} = \omega^2[M]\{\mathbf{U}\}\,,$$

where ($[K]$ is the stiffness matrix and $[M]$ is the mass matrix. Bloch's theorem can be applied through boundary conditions imposed strongly by including directly the phase shifts at the element level or performing row and column operations in these matrices [Valencia et al., 2019a]; or weakly imposing them through Lagrange multipliers or penalty methods [Michel et al., 1999, Sukumar and Pask, 2009]. After this process, we end up with the following system

$$[K_R(\mathbf{k})]\{\mathbf{U}_R\} = \omega^2[M_R(\mathbf{k})]\{\mathbf{U}_R\}\,,$$

where $\mathbf{k}$ is the wave vector which is progressively assigned successive values, in such a way that the first Brillouin zone is fully covered. Each

[1] Steven G. Johnson. Notes on the algebraic structure of wave equations. Technical report, Massachusetts Institute of Technology, 2010; and J.N. Reddy. *Applied Functional Analysis and Variational Methods in Engineering*. Krieger Publishing, 1 edition, 1991

evaluation for a particular wave vector and the solution of the related eigenvalue problem yields tuples of the form $(\mathbf{k}, \omega_n)$ representing a plane wave propagating at frequency ω_n. The subindex n refers to the nth eigenvalue computed for the input wave vector $\mathbf{k}$, this is depicted in Figure 2.

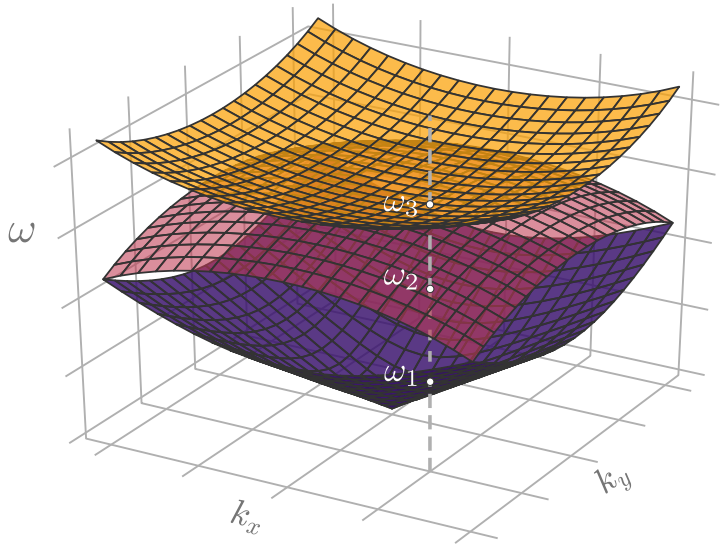

Figure 2: Schematic depicting the multiple branches obtained in a Bloch analysis. For a single point in the wavevector space there are multiple values for the frequency.

Having multiple dispersion surfaces is common for problems in electrodynamics or elastodynamics [Joannopoulos et al., 2008, Banerjee, 2011]. In the case of homogeneous materials we have two transverse modes for electromagnetic waves and two transverse modes plus a longitudinal one for elastic waves. Nevertheless, Bloch analysis introduces an additional complication since the computations are done in the first Brillouin zone. Here, wavevectors are determined up to an additive constant that is written in terms of the lattice vectors

$$\mathbf{a}_1 n_1 + \mathbf{a}_2 n_2 + \mathbf{a}_3 n_3 \quad \forall n_1, n_2, n_3 \in \mathbb{Z}\,.$$

This means that $\mathbf{k}$ and $\mathbf{k} + \mathbf{a}_1 n_1 + \mathbf{a}_2 n_2 + \mathbf{a}_3 n_3$, are assigned to the same point in the first Brillouin zone. Figure 3 illustrates this effect for the first three dispersion surfaces for a homogeneous material.

As shown in Figure 3, when using Bloch analysis we obtain dispersion surfaces ordered by frequency. This might lead to conclude that materials are anisotropic when they are not, as shown in Figure 4. For low wavenumbers, we can see that the material is isotropic/anisotropic when looking at the first mode. Nevertheless, this is not the case when looking at the second and third modes. Furthermore, anisotropy in one material might be more pronounced in one propagation mode than in others.

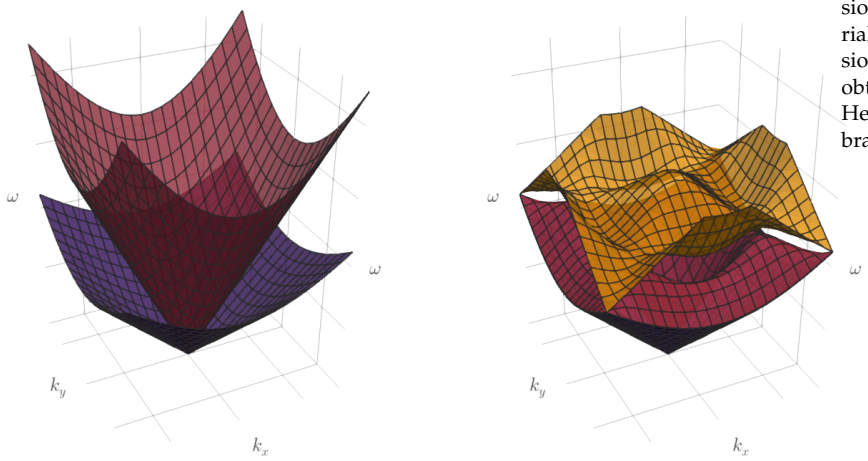

Figure 3: Comparison of the dispersion surfaces for a homogeneous material computed with the classical expression (left) with the dispersion surfaces obtained using Bloch analysis (right). Here were are showing the first three branches.

This apparent anisotropy is more difficult to analyze if we consider wave propagation in three dimensions instead of two, as can be seen in Figure 5.

Elastic wave propagation in anisotropic media

As mentioned before, periodic materials are inherently anisotropic due to their microstructure. Their *level* of anisotropy obeys the symmetries present. Following, in this section we describe the propagation of waves for elastic solids of general anisotropy.

Let us consider a wave that propagates in a solid. In this case, the conservation of density of momentum in the absence of body forces is written as

$$\sigma_{ij,i} = \rho \frac{\partial^2 u_i}{\partial t^2} \,,$$

with σ_{ij} the stress tensor, u_i the displacement vector, and ρ the mass density. In the case of a linear elastic material, Hooke's law is given by

$$\sigma_{ij} = c_{ijkl} u_{k,l} \,,$$

where c_{ijkl} is the stiffness tensor that can have up to 21 constants in the case of general anisotropy.

If we assume a plane-wave solution of the form

$$u_j = U_j e^{ik(n_m x_m - v_p t)} \,;$$

where $k = |\mathbf{k}|$ is the wavenumber, n_m is a unit vector in the direction of $\mathbf{k}$, and v_p is the phase speed; we end up with the Christoffel wave

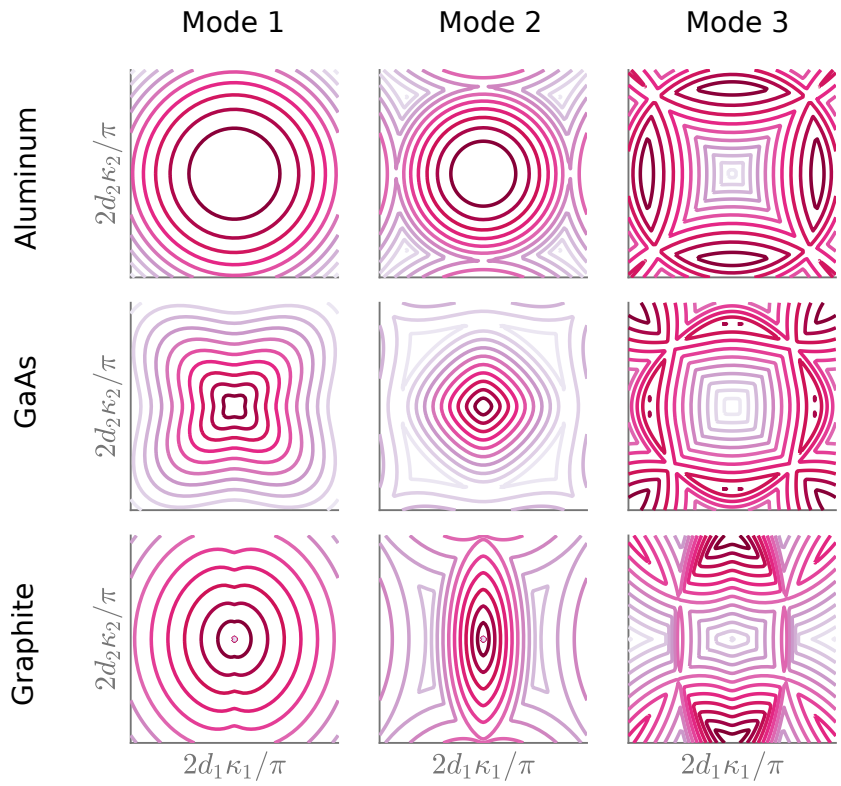

Figure 4: Comparison of the contours of iso-frequency for the first three dispersion modes for isotropic, cubic and orthotropic materials. **(Top)** Contours for aluminum, an isotropic example. **(Middle)** Contours for GaAs, a cubic example. **(Bottom)** Contours for graphite, an orthotropic example.

equation [Buchwald, 1959, Auld, 1973, Carcione, 2007]:

$$[\Gamma_{ij} - \rho v_p^2 \delta_{ij}] U_j = 0\,,$$

where $\Gamma_{ij} = c_{ijkl} n_k n_l$ is the Christoffel stiffness tensor or acoustic tensor, and δ_{ij} is the Kronecker delta. This is an eigenvalue problem, where the eigenvalues ρv_p^2 gives the phase speeds for the material. The corresponding characteristic polynomial is

$$\det\left[\Gamma_{ij} - \rho v_p^2 \delta_{ij}\right] = 0\,. \tag{3}$$

From (3) we conclude that thera are three propagating waves, each one with a different polarization. These directions are orthogonal since Γ_{ij} is symmetric. From the three polarizations, we have two quasi-transverse (qS) waves and one quasi-longitudinal (qP) wave. Where the prefix *quasi* implies that two of the modes are close to orthogonal to the wavevector and the other is close to parallel to it. As we can see, the value of Γ_{ij} depends on the direction of propagation implying that the phase speed depends on the direction of the wave (see Figure 6).

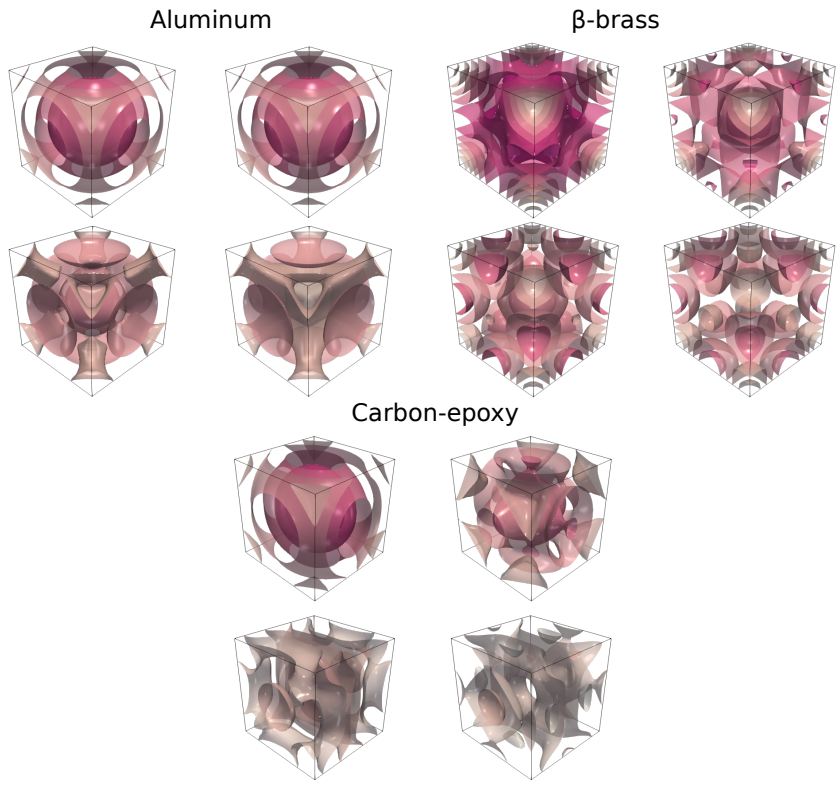

Figure 5: Comparison of the surface of iso-frequency for four dispersion modes for isotropic, cubic and transverse isotropic materials.

We can rewrite (3) as

$$\Omega(\omega, \mathbf{k}) = \det\left[\Gamma_{ij} - \rho\frac{\omega^2}{\|\mathbf{k}\|^2}\delta_{ij}\right], \tag{4}$$

taking into account that the phase speed is defined as $v_p^2 = \omega^2/\|\mathbf{k}\|^2$. The group velocity is defined as [Auld, 1973]

$$\mathbf{v}_g = \frac{\nabla_{\mathbf{k}}\Omega}{\partial\Omega/\partial\omega}, \tag{5}$$

and for lossless media it represents the direction of energy flow.

Method for directionality

Elastic anisotropy plays a role in different applications such as metallurgy [Zener, 1948], geophysics [Thomsen, 1986], wave propagation in composites [Guarín-Zapata et al., 2019], and metamaterials [Casadei and Rimoli, 2013], among others. Thus, for a particular application, one might need a material with more or less anisotropy, and the question of how anisotropic different materials are arises naturally.

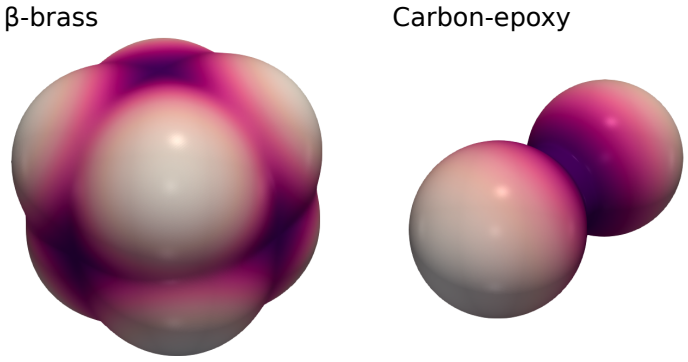

Figure 6: Comparison of the surface of relative phase speed for the quasi-longitudinal (qP) mode for cubic and transverse isotropic materials.

Some existing measures of anisotropy

One of the first measures of anisotropy was the Zener ratio [Zener, 1948] which is defined for cubic materials and is written as

$$a_r = \frac{2C_{44}}{C_{11} - C_{12}} = \frac{C_{44}}{C_{66}}\,.$$

From an intuitive perspective, it is defined as the ratio between the classical shear modulus and the *new one* that appears in cubic materials. The Zener ratio is one for isotropic materials. One extension of the Zener ratio for materials with more general anisotropy replaces the elastic coefficients by averages while retaining the form of the original ratio [Kanit et al., 2006]

$$a_{\text{gen}} = \frac{2Y_{44}}{Y_{11} - Y_{12}}\,,$$

with

$$Y_{11} = \frac{C_{11} + C_{22} + C_{33}}{3}\,, Y_{12} = \frac{C_{12} + C_{23} + C_{13}}{3}\,, Y_{44} = \frac{C_{44} + C_{55} + C_{66}}{3}\,.$$

There are other proposed metrics for measuring anisotropy such as the ratio of the maximum and minimum phase speed for the quasi-transverse modes [Ledbetter and Migliori, 2006] or the norm of the projection to the closest isotropic tensor [Carcione, 2007]. Ranganathan and Ostoja-Starzewski compute some of these metrics for several crystals and compare them with a new metric termed universal anisotropy index (UAI). Although these metrics seem to be usable for general anisotropic materials they were conceived with homogeneous materials in mind.

Regarding the anisotropy of composites, it is common to present the directionality as group velocity polar histograms based on iso-frequency contours [Ruzzene and Scarpa, 2005, Ruzzene et al., 2003].

Furthermore, Casadei and Rimoli computed an anisotropy index considering each propagation mode separately. This measure is, essentially, the standard deviation for each wave propagation mode. The main drawback with these approaches is that they considered just the first two or three modes of propagation, that is, low frequencies. Since phononic crystals can present dispersion it is expected that the anisotropy (directionality) depends on the frequency.

Method for directionality

Valencia et al. proposed a method to characterize the directionality of phononic crystals that considers the contribution of multiple modes, not just the low-frequency ones as in previous works [Ruzzene and Scarpa, 2005, Ruzzene et al., 2003]. Thus, the approach allows a more complete description of the directional response in a material and is valid in the low and high-frequency regimes. They defined the wave propagation directionality, D, as

$$D = \sum_{\substack{i \\ e>tol}} d_i(\theta)\,, \quad d_i(\theta) = C(\nabla M_i) \tag{6}$$

where M_i is the ith mode in the dispersion relation, ∇M_i is its gradient with respect to the wavevector $\mathbf{k}$, tol is a predefined tolerance, $\theta = [0, 2\pi]$ is the angle defining the propagation direction. In this definition, the operator C associates each vector to its direction (θ) and adds it to the previous vector sharing the same direction. Consequently, $d_i = C\left(\nabla M_i\right)$ corresponds to a weighted polar histogram representing the distribution of group velocity for mode M_i in any propagation direction. The weight is given by the number of times a particular direction appears in the (discrete) dispersion relations. Thus, the method can be summarized as:

- Start from the frequency surface and compute the gradient to obtain group velocities.
- Sort the (discrete) gradient by angle and add their magnitudes when they share the angle.

These steps are depicted in Figure 7.

One problem with this is method is that it is considering group velocity vectors for regions with wavevector of different magnitudes. For example, when considering a square unit cell it will include more vectors associated to directions $(1,1)$, $(-1,1)$, $(-1,-1)$ and $(1,-1)$. This makes the method depends on the shape of the unit cell chosen. Our proposed improvement is to average vectors instead of accumulating them. This is similar to restrict the analysis to wavevectors enclosed by a sphere with constant wavevector magnitude—in solid state physics

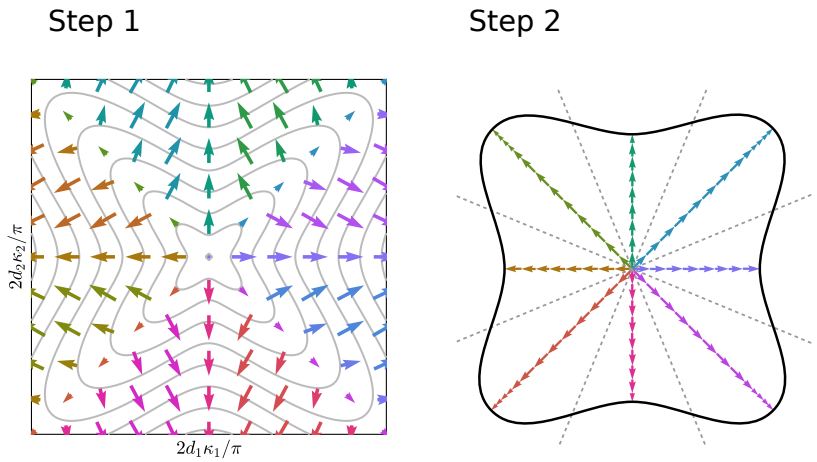

Figure 7: In **Step 1** we compute the gradient of the the ith mode of the dispersion curve. Then, in **Step 2** the group velocity vector are rearranged according to their direction and added. The resulting envelope curve represents the directionality for that mode.

states enclosed by a constant-energy surface are considered to compute the density of states [Kittel, 1996]. As an example, let us compare the computed directionality for the first dispersion surface as shown in Figure 8.

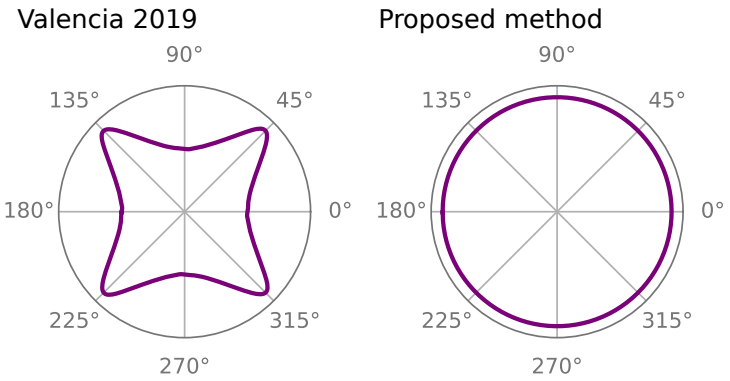

Figure 8: Comparison of the directionality computed using (**left**) Valencia's method and (**right**) our approach.

Thus, the modified method can be summarized as:

- Start from the frequency surface and compute the gradient to obtain group velocities.
- Sort the (discrete) gradient by angle and average their magnitudes when they share the angle.

One natural question that arises after is how to extend the method to three dimensions. One difference when going from two to three dimensions is that there does not exist a uniform partition of the sphere. For instance, if the spherical coordinates parameterization is

used there is a higher density of polygons in the poles. This is expected since the area differential in spherical coordinates is given by $dA = r \sin\theta \, d\varphi \, d\theta$, where θ is the zenithal angle and φ the azimuthal angle [Arfken et al., 2005]. To avoid this problem we used a triangulated mesh for the sphere that is close to uniform [Schlömer, 2020]. Figure 9 provides a comparison of two meshes.

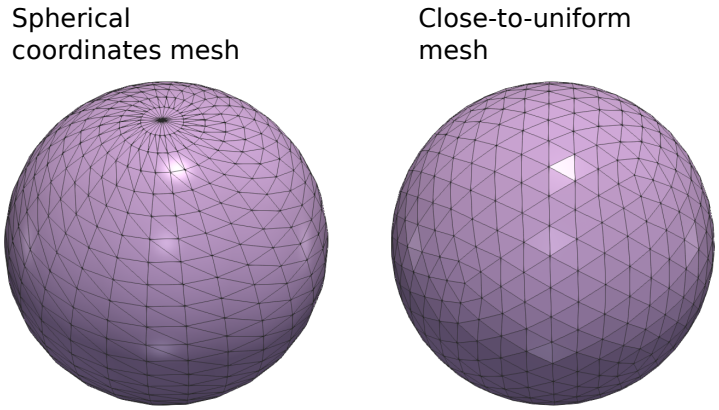

Figure 9: Comparison of a mesh of a sphere using a mesh that follows spherical coordinates and a close-to-uniform mesh. Notice the higher density of element in the pole of the left mesh.

Another difference between two and three dimensions is the absence of a *natural* order for the points[2]. To solve this problem we computed the spherical angles for each point in the sphere and created a k-D tree [Scopatz and Huff, 2015, Virtanen et al., 2020]. Then, at the moment of evaluating the direction of each group velocity vector, we made a nearest-neighbor search for its angles (θ, φ) to assign the vector to a point on the sphere as was done in the two-dimensional case.

[2] The preimage of the circle (1D) is an ordered set, that is, an interval—that follows the order of the real numbers. We cannot define this relation directly for the preimage of a sphere (2D).

Results

To test the method, we computed the directionality for materials with different symmetry classes in two and three dimensions. First, we test the method using homogeneous materials that allow to us (semi) analytically obtain the dispersion relations and then we try it with results obtained using the finite element method for a micropolar elastic material. That also shows that the method does not depend on the equations being analyzed and only needs as input the dispersion relations.

Results for analytic dispersion relations

We want to solve the determinant in (4) for ω to determine the dispersion relations. We rewrite the equation for completeness,

$$\Omega(\omega, \mathbf{k}) = \det\left[\Gamma_{ij} - \rho\frac{\omega^2}{\|\mathbf{k}\|^2}\delta_{ij}\right] = 0\,.$$

This corresponds to solving a third-degree polynomial equation for each wavenumber $\mathbf{k}$ (see the appendix at the end of this chapter for explicit forms of these equations). Then, for homogeneous materials, these relations can be solved semi-analytically and can be written as

$$\omega \equiv \omega(\mathbf{k})\,.$$

On the other hand, when these relationships are obtained from Bloch's theorem the dispersion relationships also contain information from different Brillouin zones leading to relations of the form

$$\omega_{m_1,m_1} \equiv \omega(\mathbf{k}_{m_1,m_2})\,, \tag{7}$$

in two dimensions, where the subscripts m_1, m_2 correspond to integer numbers referring to waves coming from adjacent Brillouin zones. In the case of three dimensions the relations are of the form

$$\omega_{m_1,m_2,m_3} \equiv \omega(\mathbf{k}_{m_1,m_2,m_3})\,. \tag{8}$$

In the case of a square/cube unit cell with side d, we have the following generalized definition of the wavevector [Langlet, 1993]:

$$\mathbf{k}_{m_1,m_2} = \left(k_x + \frac{m_1\pi}{d}, k_y + \frac{m_2\pi}{d}\right)\,,$$
$$\mathbf{k}_{m_1,m_2,m_3} = \left(k_x + \frac{m_1\pi}{d}, k_y + \frac{m_2\pi}{d}, k_z + \frac{m_3\pi}{d}\right)\,,$$

where k_x, k_y, and k_z are the components of the wave vector.

Figure 10 presents a comparison of directionality for a periodic material with a square unit cell for aluminum (isotropic), GaAs (cubic) and Graphite (orthotropic). We can see that the directionality curves present the same symmetries than the material class in each case (see the appendix at the end of this chapter for the material properties). The curve corresponding to the isotropic material is (almost) symmetric with respect to any rotation in the plane. In the case of the cubic material, the curve remains the same after rotations of 90°. Finally, for the orthotropic material we can see a two planes of symmetry corresponding to the x and y axes.

Figure 11 presents a comparison of directionality for a periodic material with a for β-brass (cubic) and cadmium (transverse isotropic). For the cubic material figure 11 presents a top view and an isometric

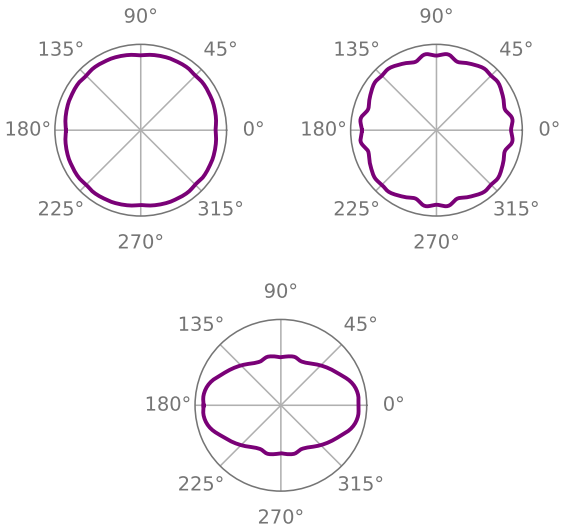

Figure 10: Comparison of directionality for a periodic material with a square unit cell for isotropic, cubic and orthotropic materials. (**Left**) Directionality for aluminum, an isotropic example. (**Center**) Directionality or GaAs, a cubic example. (**Right**) Directionality for graphite, an orthotropic example.

view of the surface, the frontal and lateral views are omitted since it presents a symmetry with respect to rotations of 90°. In the case of the transverse isotropic material a third-angle projection plus the isometric view are presented. We can see that the directionality surfaces present the same symmetries as the material class in each case, in particular, the surface is (almost) symmetric with respect to the z-axis (see the appendix at the end of the chapter for the material properties used).

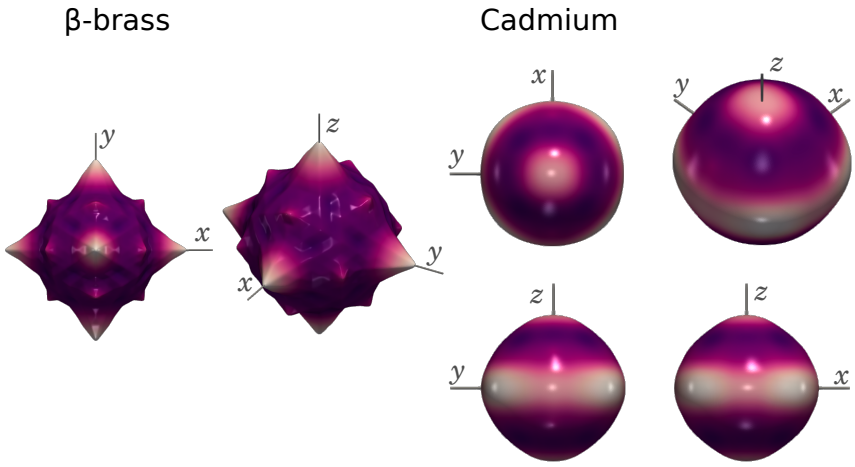

Figure 11: Comparison of the directionality surfaces for (**Left**) β-brass (**Right**) and cadmium.

Results for numerically-obtained dispersion relations

As a final result, we computed the directionality curves for cellular materials with circular pores. We changed the diameter of the pore while the size of the cell is kept fixed. The material used is a micropolar one with the following properties [Guarín-Zapata et al., 2020]:

$$\rho = 2770\ \text{kg/m}^3\,, \qquad \lambda = 5.12 \times 10^{10}\ \text{Pa}\,,$$
$$\mu = 2.76 \times 10^{10}\ \text{Pa}\,, \qquad \alpha = 3.07 \times 10^{9}\ \text{Pa}\,,$$
$$\gamma + \epsilon = 7.66 \times 10^{10}\ \text{N}\,, \qquad J = 306.5\ \text{kg/m}\,.$$

Figure 12 presents the computed directionality curves for increasing porosity values, namely: 0.000, 0.196, 0.503 and 0.709. A porosity of 0.0 represents a homogeneous material, used as a reference in this case. As expected, the directionality of the material increases with porosity, and the higher values for the averaged group speed happens along the x and y axes where we have continuous paths for the wave to propagate [Valencia et al., 2019b]. Notice that the resulting curves are symmetric with respect to rotations of 90°. The same symmetry group can be seen in the unit cell.

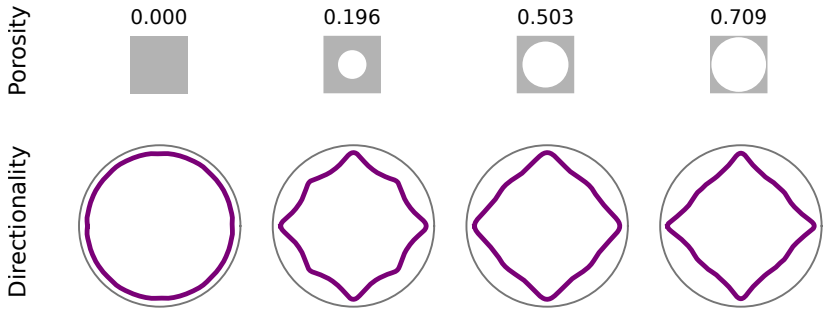

Figure 12: Directionality curves for a cellular material with increasing porosity.

For comparison, we present the isofrequency contours for the first three branches of the dispersion relations for this material in Figure 13 [Guarín-Zapata et al., 2020].

Conclusions

We presented a method to visualize the directionality of waves in periodic materials modifying the work of Valencia et al. and extending it to the three-dimensional case. This method takes as input dispersion (hyper-) surfaces obtained using a Bloch analysis and outputs a curve/surface with the bulk directionality encoded on it. As such, it can be used for dispersion curves obtained in different physical contexts such as elastodynamics of electrodynamics. The approach used

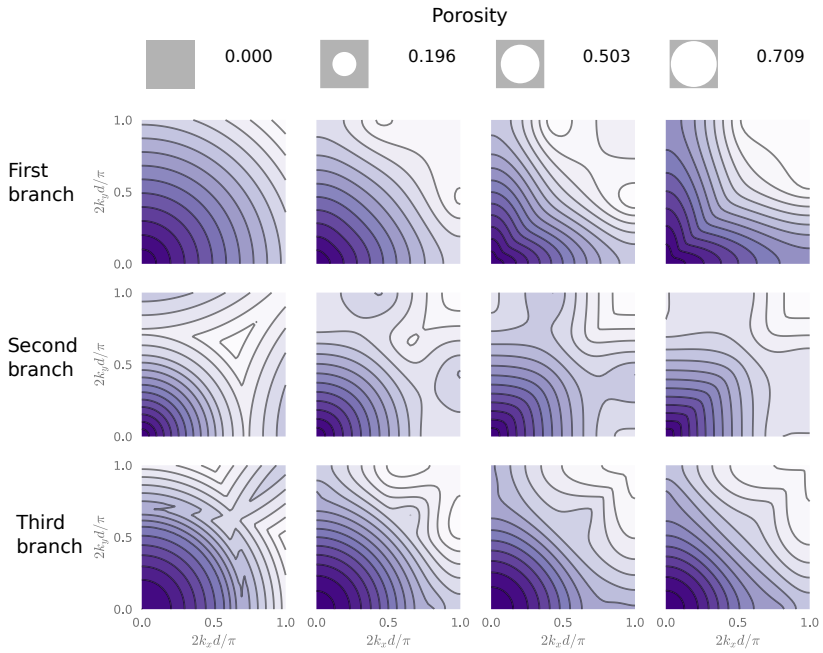

Figure 13: Curves of isofrequency for a cellular material with increasing porosity for the first three branches. These are the plots usually used to analyze directionality in periodic materials. Originally published by [Guarín-Zapata et al., 2020].

in this work does not separate modes M_i and wave types; instead, it deals with several modes at once allowing to present the directionality for a broadband frequency range and not just the low-frequency limit, as is common. Our approach provides a qualitative tool that is useful to describe the global behavior of waves when propagating through the analyzed material; it is intended to be used as a complement to dispersion curves and surfaces.

Explicit form for the Christoffel equations

Three dimensions

For a triclinic material with a stifness tensor given by

$$[C] = \begin{bmatrix} C_{11} & C_{12} & C_{13} & C_{14} & C_{15} & C_{16} \\ C_{12} & C_{22} & C_{23} & C_{24} & C_{25} & C_{26} \\ C_{13} & C_{23} & C_{33} & C_{34} & C_{35} & C_{36} \\ C_{14} & C_{24} & C_{34} & C_{44} & C_{45} & C_{46} \\ C_{15} & C_{25} & C_{35} & C_{45} & C_{55} & C_{56} \\ C_{16} & C_{26} & C_{36} & C_{46} & C_{56} & C_{66} \end{bmatrix},$$

in Voigt notation, a density ρ and a wavevector $\mathbf{k}$, the equation that need to be solved is [Auld, 1973]

$$\det\left(\|\mathbf{k}\|^2\begin{bmatrix}\alpha & \delta & \varepsilon\\ \delta & \beta & \xi\\ \varepsilon & \xi & \gamma\end{bmatrix}\begin{bmatrix}u_1\\ u_2\\ u_3\end{bmatrix} - \rho\omega^2\begin{bmatrix}1 & 0 & 0\\ 0 & 1 & 0\\ 0 & 0 & 1\end{bmatrix}\begin{bmatrix}u_1\\ u_2\\ u_3\end{bmatrix}\right) = 0\,, \quad (9)$$

with

$$\begin{aligned}
\alpha =& C_{11}n_1^2 + C_{66}n_2^2 + C_{55}n_3^2 + 2C_{56}n_1n_3 + 2C_{15}n_3n_1 + 2C_{16}n_1n_2\,,\\
\beta =& C_{66}n_1^2 + C_{22}n_2^2 + C_{44}n_3^2 + 2C_{24}n_2n_3 + 2C_{46}n_3n_1 + 2C_{26}n_1n_2\,,\\
\gamma =& C_{55}n_1^2 + C_{44}n_2^2 + C_{33}n_3^2 + 2C_{34}n_2n_3 + 2C_{35}n_3n_1 + 2C_{45}n_1n_2\,,\\
\delta =& C_{16}n_1^2 + C_{26}n_2^2 + C_{33}n_3^2 + (C_{46}+C_{25})n_2n_3 + (C_{14}+C_{56})n_3n_1\\
&+ (C_{12}+C_{66})n_1n_2\,,\\
\varepsilon =& C_{15}n_1^2 + C_{46}n_2^2 + C_{35}n_3^2 + (C_{45}+C_{36})n_2n_3 + (C_{13}+C_{55})n_2n_1\\
&+ (C_{14}+C_{56})n_1n_2\,,\\
\zeta =& C_{56}n_1^2 + C_24n_2^2 + C_{34}n_3^2 + (C_{44}+C_{23})n_2n_3 + (C_{36}+C_{45})n_3n_1\\
&+ (C_{25}+C_{46})n_1n_2\,,
\end{aligned}$$

where $\hat{\mathbf{n}} = (n_1, n_2, n_3) = \frac{\mathbf{k}}{\|\mathbf{k}\|}$.

In the case of orthotropic materials aligned with the coordinate system these expressions can be simplified to

$$\begin{aligned}
\alpha =& C_{11}n_1^2 + C_{66}n_2^2 + C_{55}n_3^2\,,\\
\beta =& C_{66}n_1^2 + C_{22}n_2^2 + C_{44}n_3^2\,,\\
\gamma =& C_{55}n_1^2 + C_{44}n_2^2 + C_{33}n_3^2\,,\\
\delta =& (C_{12}+C_{66})n_1n_2\,,\\
\varepsilon =& (C_{13}+C_{55})n_3n_1\,,\\
\zeta =& (C_{44}+C_{23})n_2n_3\,,
\end{aligned}$$

this can be further simplified for cubic materials.

$$\begin{aligned}
\alpha =& C_{11}n_1^2 + C_{44}(1-n_1^2)\,,\\
\beta =& C_{11}n_2^2 + C_{44}(1-n_2^2)\,,\\
\gamma =& C_{11}n_3^2 + C_{44}(1-n_3^2)\,,\\
\delta =& (C_{12}+C_{44})n_1n_2\,,\\
\varepsilon =& (C_{12}+C_{44})n_3n_1\,,\\
\zeta =& (C_{12}+C_{44})n_2n_3\,.
\end{aligned}$$

For materials with tranverse isotropic symmetry the equations can be solved analytically [Carcione, 2007]. For a wave propagating in the

plane 1-3, and taking $n_2 = 0$, we have

$$\begin{aligned}
\omega_{\text{qP}}^2 =& \frac{\|\mathbf{k}\|^2(C_{11}n_1^2 + C_{33}n_3^2 + C_{55} + \sqrt{M})}{2\rho}\,,\\
\omega_{\text{qS}}^2 =& \frac{\|\mathbf{k}\|^2(C_{11}n_1^2 + C_{33}n_3^2 + C_{55} - \sqrt{M})}{2\rho}\,,\\
\omega_{\text{S}}^2 =& \frac{\|\mathbf{k}\|^2(C_{66}n_1^2 + C_{55}n_3^2)}{\rho}\,,\\
M =& [(C_{11} - C_{55})n_1^2 + (C_{55} - C_{33})n_3^2]^2 + 4[(C_{13} + C_{55})^2 n_1 n_3]^2\,.
\end{aligned}$$

Two dimensions

In the case of a monoclinic material we could align the symmetry plane to obtain the following two-dimensional problem

$$\det\left(\|\mathbf{k}\|^2 \begin{bmatrix}\alpha & \delta\\ \delta & \beta\end{bmatrix} - \rho\omega^2 \begin{bmatrix}1 & 0\\ 0 & 1\end{bmatrix}\right) = 0\,,$$

that can be solved analytically as

$$\omega^2 = \frac{\|\mathbf{k}\|^2}{2\rho}[\alpha + \beta \pm \sqrt{(\alpha - \beta)^2 + 4\delta^2}]$$

with

$$\begin{aligned}
\alpha =& C_{11}n_1^2 + C_{66}n_2^2 + 2C_{16}n_1 n_2\,,\\
\beta =& C_{66}n_1^2 + C_{22}n_2^2 + 2C_{26}n_1 n_2\,,\\
\delta =& C_{16}n_1^2 + C_{26}n_2^2 + (C_{12} + C_{66})n_1 n_2\,,
\end{aligned}$$

that reduces to

$$\begin{aligned}
\alpha =& C_{11}n_1^2 + C_{66}n_2^2\,,\\
\beta =& C_{66}n_1^2 + C_{22}n_2^2\,,\\
\delta =& (C_{12} + C_{66})n_1 n_2\,,
\end{aligned}$$

for orthotropic materials and

$$\begin{aligned}
\alpha =& C_{11}n_1^2 + C_{66}n_2^2\,,\\
\beta =& C_{66}n_1^2 + C_{11}n_2^2\,,\\
\delta =& (C_{12} + C_{66})n_1 n_2\,,
\end{aligned}$$

for cubic materials.

Material properties

Following we present the properties used along the paper.

Two dimensions

- Aluminum:

$$[C] = \begin{bmatrix} 112.35 & 60.49 & 0 \\ 60.49 & 112.35 & 0 \\ 0 & 0 & 25.9 \end{bmatrix} \text{ GPa}, \quad \rho = 2700 \text{ kg/m}^3.$$

- GaAs:

$$[C] = \begin{bmatrix} 118.8 & 59.4 & 0 \\ 59.4 & 118.8 & 0 \\ 0 & 0 & 53.7 \end{bmatrix} \text{ GPa}, \quad \rho = 5320 \text{ kg/m}^3.$$

- Graphite:

$$[C] = \begin{bmatrix} 235 & 3.69 & 0 \\ 3.69 & 26 & 0 \\ 0 & 0 & 28.2 \end{bmatrix} \text{ GPa}, \quad \rho = 1790 \text{ kg/m}^3.$$

Three dimensions

- Aluminum:

$$[C] = \begin{bmatrix} 112.35 & 60.49 & 60.49 & 0 & 0 & 0 \\ 60.49 & 112.35 & 60.49 & 0 & 0 & 0 \\ 60.49 & 60.49 & 112.35 & 0 & 0 & 0 \\ 0 & 0 & 0 & 25.9 & 0 & 0 \\ 0 & 0 & 0 & 0 & 25.9 & 0 \\ 0 & 0 & 0 & 0 & 0 & 25.9 \end{bmatrix} \text{ GPa}, \quad \rho = 2700 \text{ kg/m}^3.$$

- β-brass:

$$[C] = \begin{bmatrix} 52 & 27.5 & 27.5 & 0 & 0 & 0 \\ 27.5 & 52 & 27.5 & 0 & 0 & 0 \\ 27.5 & 27.5 & 52 & 0 & 0 & 0 \\ 0 & 0 & 0 & 173 & 0 & 0 \\ 0 & 0 & 0 & 0 & 173 & 0 \\ 0 & 0 & 0 & 0 & 0 & 173 \end{bmatrix} \text{ GPa}, \quad \rho = 7600 \text{ kg/m}^3.$$

- Cadmium:

$$[C] = \begin{bmatrix} 115.9 & 41.05 & 41 & 0 & 0 & 0 \\ 41.05 & 115.9 & 41 & 0 & 0 & 0 \\ 41 & 41 & 51.2 & 0 & 0 & 0 \\ 0 & 0 & 0 & 19.95 & 0 & 0 \\ 0 & 0 & 0 & 0 & 19.95 & 0 \\ 0 & 0 & 0 & 0 & 0 & 37.43 \end{bmatrix} \text{ GPa}, \quad \rho = 8650 \text{ kg/m}^3.$$

- Carbon-Epoxy:

$$[C] = \begin{bmatrix} 12.37 & 6.15 & 6.19 & 0 & 0 & 0 \\ 6.15 & 21.37 & 6.19 & 0 & 0 & 0 \\ 6.19 & 6.19 & 146.30 & 0 & 0 & 0 \\ 0 & 0 & 0 & 4.80 & 0 & 0 \\ 0 & 0 & 0 & 0 & 4.80 & 0 \\ 0 & 0 & 0 & 0 & 0 & 3.11 \end{bmatrix} \text{GPa}, \quad \rho = 1900 \text{ kg/m}^3.$$

Waves in periodic micropolar solids

Introduction

The increasing growth and strong development of the field of architected materials during recent years has created a renewed interest in generalized or extended versions of classical continuum mechanics theories. Popular examples of these emerging disciplines can be identified in the area of phononic crystals and metamaterials [Hussein et al., 2014, Srivastava, 2015]. These are materials which by virtue of their architected microstructure exhibit unexpected mechanical properties at the macro level, such as negative refraction, negative bulk modulus or negative mass [Banerjee, 2011]. For example, the conversion from axial deformation into twist, would require chirality, which in turn would require an asymmetric stress tensor [Lakes, 2001, Frenzel et al., 2017]. From the wave propagation perspective, these materials are attractive since they exhibit dispersive phenomena, such as filtering and directional effects over fixed frequency ranges [Gonella and Ruzzene, 2008]. Physically, such phenomena result from the interactions of the incident field with the microstructural elements producing local scattering and diffraction. Another wave phenomenon of interest is cloaking, where the propagation is directed around an object rendering it *invisible*. This is another application where there is a need for asymmetric stresses. For electromagnetic waves, this can be achieved through transformation optics [Schurig et al., 2006].

Nevertheless, it has been shown that in the case of elastic bodies the equations are not invariant [Milton and Willis, 2007]. Additional requirements, related with micro rotations, exist in this case, and the equations that satisfy the invariance are termed Willis equations that can be expressed as micropolar elasticity under some assumptions [Norris and Shuvalov, 2011]. Recently, [Yavari and Golgoon, 2018] has proposed that micropolar elasticity does not satisfy the invariant requirements needed for elastic cloaking and [Sklan et al., 2018] presented an approached that keeps the symmetry of the stress tensor without perfect cloaking.

The validation and effective use of these materials, particularly in

dynamic analysis simulations involves two general steps. In the first place, it is necessary to conduct a design or characterization of the material in terms of its band structure or frequency-wave vector relation for a representative unit cell. This analysis step is typically conducted via Bloch analysis of the unit cell, which comprises solving a series of eigenvalue problems for a numerical model of the cell that explicitly includes all its microstructural elements. The solution from these analyses identify propagation frequencies associated to variations of the wave vector along the boundaries of the unit cell after considering the spatial periodicity of the material. The second analysis step involves the solution of a time-domain boundary value problem, which requires the consideration of a large number of material cells filling out the particular domain. Clearly, from a numerical point of view, the inclusion of the microstructural details in the numerical model implies prohibitive computational costs, thus requiring continuum based mechanical models with intrinsic capabilities to reproduce dispersive behavior.

Dispersion at the macroscopic level can be understood in terms of scattering and diffraction arising when the wave length of the free wave field approaches characteristic dimensions of the microstructural elements and, as a result, its treatment in terms of continuum mechanics requires theories involving constitutive length scale parameters. Broadly speaking, these class of models can be classified into (i) gradient based theories and (ii) enriched kinematics models. In the former, local kinematic descriptions retaining higher order displacement gradients are introduced resulting also in higher order stress tensors [Truesdell and Toupin, 1960, Aero and Kuvshinski, 1961, Toupin, 1962, Mindlin and Tiersten, 1962, Koiter, 1964, Mindlin, 1964, 1965, Mindlin and Eshel, 1965, Eringen, 1966, Yang et al., 2002, Hadjesfandiari and Dargush, 2011, Hadjesfandiari et al., 2015]. Alternatively, in the latter approach, the material point is endowed with additional degrees of freedom [Cosserat and Cosserat, 1909, Voigt, 1910, Eringen, 1966, Nowacki, 1986].

This family of non-classical or generalized continuum models have been used in a wide range of applications in several research problems [Nix and Gao, 1998, Fleck and Hutchinson, 1997, Fleck et al., 1994, Stolken and Evans, 1998, Takeo, 1998a,b, Takeo and Ito, 1997, Midya, 2004, Merkel et al., 2011, Trovalusci et al., 2015, Iliopoulos et al., 2016, 2017]. However, there is a need to examine the strengths and weaknesses of the various models and to propose physical experiments that would be helpful in their critical assessment.

In this work we explore the capabilities of the micropolar model to capture dispersive behavior by virtue of its kinematic variables and particularly through the additional constitutive parameters. For that

purpose, we address several theoretical and simulation aspects relevant to wave propagation in such micropolar medium. We start by reviewing the field equations for the model with special emphasis placed in the displacement-based equations of motion as these reveal phase velocities associated to the possible free wave modes, that is with uncouple waves in the case of unbounded domains. Following that section, we also discuss Bloch periodicity in the context of the micropolar theory. We show the relation between displacements and rotations, together with its corresponding traction components along the different regions of the unit cell properly accounting for the infinite character of the analysis domain in terms of a single material cell. Also, as will be shown later, the dispersion analysis via the Bloch theorem involves the solution of the frequency-domain reduced wave equation and thus it is useful to show the Hermitian and positive definite character of the boundary value problem. The theoretical aspects of the paper also describe the variational statement and details for its finite element discretization, when conducting Bloch analysis. In the final part of the paper, we use the finite element formulation to test the capability of the micropolar model to capture dispersive behavior. First, and as a verification exercise of the formulation, we find the numerical and analytic band structure for a homogeneous micropolar continuum. The homogeneous cell analysis is also used to identify appropriate mesh properties in Bloch analysis of micropolar media. In a subsequent analysis aimed at producing further dispersion in the model, we also consider material cells with simple microstructures, namely a bilayer composite and a porous material composed of a circular cavity embedded in a micropolar matrix. These are simple microstructures, which facilitate the study of the variation of the dispersive properties by introducing changes in material and geometric parameters. In both cases, we find band structures for different values of the mechanical and geometric parameters and track the variation of the cut-off frequency associated to the microrotational waves.

Micropolar Model

The micropolar model used in this work introduces rotational mechanical interaction between material points in terms of a couple-tractions vector $m_i^{(\hat{n})}$ defined through a generalized Cauchy's postulate as [3]:

$$\lim_{\Delta S(\hat{n})\to 0} \frac{\Delta M_i}{\Delta S(\hat{n})} = m_i^{(\hat{n})} \tag{10}$$

where $\Delta S(\hat{n})$ is a small element of area oriented with $\hat{n}$ and ΔM_i is the resultant moment. The couple-tractions are completely described by

[3] G. Thomas Mase, Ronald E. Smelser, and George E. Mase. *Continuum mechanics for engineers*. CRC press, 2009

the couple-stress tensor μ_{ij} according to

$$m_j^{(\hat{n})} = \mu_{ij}\hat{n}_i. \tag{11}$$

In (10) above, $\Delta S(\hat{n})$ represents a surface material element with outward normal $\hat{n}$. Considering now the classical force per unit surface tractions vector $t_j^{(\hat{n})}$ related to the Cauchy stress tensor σ_{ij}, such as

$$t_j^{(\hat{n})} = \sigma_{ij}\hat{n}_i \tag{12}$$

leads to momentum and moment of momentum balance equations for the micropolar solid [Nowacki, 1986]:

$$\sigma_{ji,j} + f_i = \rho\ddot{u}_i \tag{13a}$$
$$\sigma_{jk}\epsilon_{ijk} + \mu_{ji,j} + c_i = J\ddot{\theta}_i \tag{13b}$$

and where u_i is the displacement vector and θ_i is the microrrotation vector; f_i and c_i are forces and moments per unit volume; ρ and J are the mass and rotational inertial densities, respectively, and ϵ_{ijk} is the Levi-Civita permutation tensor. In the model proposed by Hadjesfandiari and Dargush the term c_i is shown to be equivalent to a body force, while J is eliminated at the onset. Here we retain the original form of the equations given in Nowacki [1986], where both terms are retained. Denoting displacements and microrotation vectors at a field point $\mathbf{x}$ and at the time instant t by $u_i(\mathbf{x}, t)$ and $\theta_i(\mathbf{x}, t)$, respectively, we have that the local deformation γ_{ji} at the material point is now the difference between the displacement gradients $u_{i,j}$ and the microrotation (vector) θ_k

$$\gamma_{ji} = u_{i,j} - \epsilon_{kji}\theta_k\,. \tag{14}$$

Also, notice that the consideration of the independent microrotational field introduces an additional kinematic variable in the form of a generalized curvature-twist κ_{ji} describing the change of microrotation per unit length

$$\kappa_{ji} = \theta_{i,j}. \tag{15}$$

In a linear isotropic elastic micropolar medium the constitutive equations take the following form [Nowacki, 1986]:

$$\sigma_{ji} = (\mu + \alpha)\gamma_{ji} + (\mu - \alpha)\gamma_{ij} + \lambda\gamma_{kk}\delta_{ij}\,, \tag{16a}$$
$$\mu_{ji} = (\eta + \varepsilon)\kappa_{ji} + (\eta - \varepsilon)\kappa_{ij} + \beta\kappa_{kk}\delta_{ij}\,. \tag{16b}$$

where μ and λ are the known Lamé parameters from classical elasticity, while α, β, η and ε are extra material parameters from the micropolar model and representative of additional particle interactions. The set of constitutive equations can also be written in the following

alternative form:

$$\sigma_{ji} = \mu\gamma^S_{ij} + 2\alpha\gamma^A_{ij} + \lambda\gamma_{kk}\delta_{ij}\,,$$
$$\mu_{ji} = \eta\kappa^S_{ij} + 2\varepsilon\kappa^A_{ij} + \beta\kappa_{kk}\delta_{ij}\,,$$

where the superscripts S and A denote the symmetric and skew-symmetric parts of the associated second order tensors. We can mention that β is a parameter only related to torsion, using a parallel with classical elasticity it resembles the role of λ. On the other hand, η is related to torsion and bending while ε is only related to bending modulus. Furthermore, α is known as micropolar couple modulus and quantifies the coupling between micro and macrorotation — see [Lakes, 1991, Hassanpour and Heppler, 2017, 2014] for further discussion on the interpretation of these parameters.

Using (46) together with (41a) and (15) in the linear and angular momentum balance equations leads to displacement time-domain equations of motion:

$$(\lambda+2\mu)u_{k,ki} - \epsilon_{ijk}\epsilon_{klm}(\mu+\alpha)u_{m,lj} + 2\alpha\epsilon_{ijk}\theta_{k,j} + f_i = \rho\ddot{u}_i\,, \quad (17a)$$
$$(\beta+2\eta)\theta_{k,ki} - \epsilon_{ijk}\epsilon_{klm}(\eta+\varepsilon)\theta_{m,lj} + 2\alpha\epsilon_{ijk}u_{k,j} - 4\alpha\theta_i + c_i = J\ddot{\theta}_i\,. \quad (17b)$$

With boldface characters denoting vector fields, the equations of motion can also be written for completeness in explicit form as:

$$(\lambda+2\mu)\boldsymbol{\nabla}\boldsymbol{\nabla}\cdot\mathbf{u} - (\mu+\alpha)\boldsymbol{\nabla}\times\boldsymbol{\nabla}\times\mathbf{u} + 2\alpha\boldsymbol{\nabla}\times\boldsymbol{\theta} + \mathbf{f} = \rho\frac{\partial^2\mathbf{u}}{\partial t^2}, \quad (18a)$$
$$(\beta+2\eta)\boldsymbol{\nabla}\boldsymbol{\nabla}\cdot\boldsymbol{\theta} - (\eta+\varepsilon)\boldsymbol{\nabla}\times\boldsymbol{\nabla}\times\boldsymbol{\theta} + 2\alpha\boldsymbol{\nabla}\times\mathbf{u} - 4\alpha\boldsymbol{\theta} + \mathbf{c} = J\frac{\partial^2\boldsymbol{\theta}}{\partial t^2}\,. \quad (18b)$$

When considering plane problems the term $\boldsymbol{\nabla}\boldsymbol{\nabla}\cdot\boldsymbol{\theta}$ is zero and the behavior will not depend on the parameter β, see the last section of this chapter for the explicit expressions for plane problems.

Notice in (17b) and (18b) the appearance of the dilatation $\boldsymbol{\nabla}\cdot\boldsymbol{\theta}$, which implicitly assumes that $\boldsymbol{\theta}$ is not, in fact, a pure rotation (or microrotation). On the other hand, if $\boldsymbol{\nabla}\cdot\boldsymbol{\theta} = 0$ is enforced, then the resulting theory would suffer from the same type of indeterminacy as the original couple stress theory [Mindlin and Tiersten, 1962]. Following the current convention, however, $\boldsymbol{\theta}$ will continue to be called the microrotation in this paper.

In order to conduct Bloch analysis, and more specifically to determine the dispersion relations for a micropolar solid, it is convenient to neglect the body force and couple densities and to assume a time dependence of the form $e^{-i\omega t}$ for both the displacement and rotation field, therefore yielding the following reduced frequency-domain ver-

sion of the equations of motion:

$$\begin{aligned}(\lambda+2\mu)\boldsymbol{\nabla}\boldsymbol{\nabla}\cdot\mathbf{u}-(\mu+\alpha)\boldsymbol{\nabla}\times\boldsymbol{\nabla}\times\mathbf{u}+2\alpha\boldsymbol{\nabla}\times\boldsymbol{\theta}&=-\rho\omega^2\mathbf{u}\,,\\(\beta+2\eta)\boldsymbol{\nabla}\boldsymbol{\nabla}\cdot\boldsymbol{\theta}-(\eta+\varepsilon)\boldsymbol{\nabla}\times\boldsymbol{\nabla}\times\boldsymbol{\theta}+2\alpha\boldsymbol{\nabla}\times\mathbf{u}-4\alpha\boldsymbol{\theta}&=-J\omega^2\boldsymbol{\theta}\,.\end{aligned}\tag{19}$$

For convenience in later developments and to aid the comparison with similar formulations available in the literature, it is convenient to use also the alternative form:

$$\begin{aligned}c_1^2\boldsymbol{\nabla}\boldsymbol{\nabla}\cdot\mathbf{u}-c_2^2\boldsymbol{\nabla}\times\boldsymbol{\nabla}\times\mathbf{u}+K^2\boldsymbol{\nabla}\times\boldsymbol{\theta}&=-\omega^2\mathbf{u}\,,\\c_3^2\boldsymbol{\nabla}\boldsymbol{\nabla}\cdot\boldsymbol{\theta}-c_4^2\boldsymbol{\nabla}\times\boldsymbol{\nabla}\times\boldsymbol{\theta}+Q^2\boldsymbol{\nabla}\times\mathbf{u}-2Q^2\boldsymbol{\theta}&=-\omega^2\boldsymbol{\theta}\end{aligned}\tag{20}$$

and where: c_1 represents the phase/group speed for the longitudinal wave (P) that is non-dispersive as in the classical case, c_2 represents the high-frequency limit ($k\to\infty$) phase/group speed for a transverse wave (S) that is dispersive unlike the classical counterpart, c_3 represents the high-frequency limit ($k\to\infty$) phase/group speed for a longitudinal-rotational wave (LR) with a corkscrew-like motion that is dispersive and does not have a classical counterpart, c_4 represents the high-frequency limit ($k\to\infty$) phase/group speed for a transverse-rotational wave (TR) that is dispersive and does not have a classical counterpart, Q represents the cut-off frequency for rotational waves appearance, and K quantifies the difference between the low-frequency and high-frequency phase/group speed for the S-wave —see fig. 14 for a qualitative description. These parameters are defined by:

$$\begin{aligned}c_1^2&=\frac{\lambda+2\mu}{\rho},\quad c_3^2=\frac{\beta+2\eta}{J},\\c_2^2&=\frac{\mu+\alpha}{\rho},\quad c_4^2=\frac{\eta+\varepsilon}{J},\\Q^2&=\frac{2\alpha}{J},\quad K^2=\frac{2\alpha}{\rho}\,.\end{aligned}$$

We should highlight that c_3 does not play a role for waves in the plane. As mentioned before, $\boldsymbol{\nabla}\boldsymbol{\nabla}\cdot\boldsymbol{\theta}=0$ in that case.

The Principle of Virtual Work (PVW) for a micropolar solid follows after considering the translational and rotational equilibrium equations, using the virtual fields δu_i and $\delta\theta_i$ as weighting functions and integrating over the volume V with the aid of the divergence theorem. Denoting the kinematic measures in a micropolar solid by γ_{ij}^S, γ_{ij}^A and κ_{ij} corresponding to the classical infinitesimal strain tensor, the skew-symmetric part of the relative deformation tensor — i.e., the difference between the displacement gradient and the micro-displacement gradient — and the generalized curvature-twist tensor allow us to write this

principle in the form

$$\int_V \sigma_{ij}^S \delta\gamma_{ij}^S \,\mathrm{d}V + \int_V \sigma_{ij}^A \delta\gamma_{ij}^A \,\mathrm{d}V + \int_V \mu_{ij}\delta\kappa_{ij} \,\mathrm{d}V - \int_S t_i\delta_i \,\mathrm{d}S - \int_S m_i\delta\theta_i \,\mathrm{d}S - \omega^2 \int_V \rho u_i \delta u_i \,\mathrm{d}V - \omega^2 \int_V J\theta_i\delta\theta_i \,\mathrm{d}V = 0 \tag{21}$$

where σ_{ij}^S is the symmetric part of the stress tensor, while σ_{ij}^A is the skew-symmetric part of the stress tensor.

Formulation for Periodic Materials

Here we review the relevant aspects of the analysis of spatially periodic materials in terms of the theory of phononic crystals, and particularly the so-called Bloch-Floquet periodic boundary conditions applied to the micropolar solid. For an in-depth discussion of periodic materials the reader is referred to classical sources [Brillouin, 1953, Kittel, 1996], while a comprehensive review is provided in [4]. In that theory, the key concept is established by Bloch's theorem, providing a relationship between the fields on opposite sides of the cell and taking into account spatial periodicity in a wave propagation problem. Therefore, the characterization of the micropolar medium is to be conducted after assuming that the material is the result of the spatial and periodic repetition of a fundamental unit cell. Under this assumption, a fundamental cell containing a motif repeats itself (in one, two, or three space dimensions) according to a spatial period defined in terms of a lattice vector. The *motif* refers to a microstructural heterogeneity which could contain different materials and geometries, as well as fluids and/or solids of the classical or Cosserat type. The dispersive properties of such a periodic material, given in terms of frequency-wave number relations (or band diagram), can be found from the analysis of a single fundamental cell after using Bloch's theorem, which establishes that a function $\mathbf{u}(\mathbf{x})$ can be expressed in the form

$$\mathbf{u}(\mathbf{x}) = \mathbf{w}(\mathbf{x})e^{i\mathbf{k}\cdot\mathbf{x}}\,, \tag{22}$$

where $\mathbf{w}(\mathbf{x})$ is the Bloch function that has the same periodicity of the material and $\mathbf{k}$ is a wave vector. Accordingly, the solution is the product of a periodic function with the periodicity of the lattice and a plane wave, that is also periodic. As a consequence, the field variables in the differential equation satisfy the relation

$$\mathbf{\Phi}(\mathbf{x}+\mathbf{a}) = \mathbf{\Phi}(\mathbf{x})e^{i\mathbf{k}\cdot\mathbf{a}}\,,$$

connecting the variable $\mathbf{\Phi}$ at opposite sides of the unit cell set apart by a vector $\mathbf{a}$. In this case, $\mathbf{\Phi}$ refers to the principal variable (or any

[4] Mahmoud I. Hussein, Michael J. Leamy, and Massimo Ruzzene. Dynamics of phononic materials and structures: Historical origins, recent progress, and future outlook. *Applied Mechanics Reviews*, 66(4):040802, 2014

of its spatial derivatives) involved in the physical problem. It then follows that if one wants to characterize the material in terms of its wave propagation velocities to obtain values that can be used in a homogenized continuum model, it suffices to analyze a single cell. In the case of the micropolar medium, Bloch's theorem states that the eigenfunctions of (19) can be expressed in the form

$$u_r(\mathbf{x}) = u_r(\mathbf{x}+\mathbf{a})e^{i\mathbf{k}\cdot\mathbf{a}},$$
$$\theta_r(\mathbf{x}) = \theta_r(\mathbf{x}+\mathbf{a})e^{i\mathbf{k}\cdot\mathbf{a}},$$

where $\mathbf{a}$ is a vector that represents the periodicity of the material. That is, the solution is the same at opposite sides of the unit cell, except for a phase shift factor $e^{i\mathbf{k}\cdot\mathbf{a}}$. Due to the linearity of the differential equations we also have the following Bloch-periodic boundary conditions for the corresponding traction vectors

$$t_r(\mathbf{x}) = -t_r(\mathbf{x}+\mathbf{a})e^{i\mathbf{k}\cdot\mathbf{a}},$$
$$m_r(\mathbf{x}) = -m_r(\mathbf{x}+\mathbf{a})e^{i\mathbf{k}\cdot\mathbf{a}}.$$

Thus, in the case of the micropolar solid, Bloch's theorem reduces to the following set of boundary conditions for displacements, microrotations, force-tractions and couple-tractions:

$$u_r(\mathbf{x}) = u_r(\mathbf{x}+\mathbf{a})e^{i\mathbf{k}\cdot\mathbf{a}}, \tag{23a}$$
$$\theta_r(\mathbf{x}) = \theta_r(\mathbf{x}+\mathbf{a})e^{i\mathbf{k}\cdot\mathbf{a}}, \tag{23b}$$
$$t_r(\mathbf{x}) = -t_r(\mathbf{x}+\mathbf{a})e^{i\mathbf{k}\cdot\mathbf{a}}, \tag{23c}$$
$$m_r(\mathbf{x}) = -m_r(\mathbf{x}+\mathbf{a})e^{i\mathbf{k}\cdot\mathbf{a}}. \tag{23d}$$

The set of conditions summarized in (23) will be satisfied in a variational sense using a finite element formulation. Subsequently, a numerical model of the unit cell resulting in a generalized eigenvalue problem will be solved for various specifications of the wave vector. The details of such an implementation will be discussed next.

Hermiticity of the equations

Since the dynamic analysis of the micropolar medium involves solution of the frequency domain reduced wave equation subject to Bloch periodic boundary conditions, as given by (23), it becomes necessary to rewrite the PVW (21) so it can be used to properly represent inner products in complex-valued vector spaces. Using the operator $*$ to

denote complex conjugate, we can write:

$$\delta\Pi(\omega, u_i, \hat{u}_i) = \int_V \tau_{ij}^* \hat{e}_{ij}\, \mathrm{d}V + \int_V \sigma_{ij}^* \hat{\gamma}_{ij}^A\, \mathrm{d}V + \int_V \mu_{ij}^* \hat{\kappa}_{ij}\, \mathrm{d}V - \int_S t_i^* \hat{u}_i\, \mathrm{d}S - \int_S m_i^* \hat{\theta}_i\, \mathrm{d}S - \omega^2 \int_V \rho u_i^* \hat{u}_i\, \mathrm{d}V - \omega^2 \int_V J\theta_i^* \hat{\theta}_i\, \mathrm{d}V \equiv 0\,. \tag{24}$$

In the principle of virtual work given by (24) u_i and $\hat{u}_i$ represent the actual and virtual fields respectively. In the sense of (24), $\delta\Pi$ could be understood as the variation of the Lagrangian functional of the micropolar system. As will be demonstrated next, if we interchange the variables u_i and $\hat{u}_i$, we find that

$$\delta\Pi(\omega, u_i, \hat{u}_i) = \delta\Pi(\omega, \hat{u}_i, u_i)$$

which implies that the operator is Hermitian (self-adjoint) under Bloch periodic boundary conditions also resulting in Hermitian matrices when discretized via finite elements.

The proof of Hermiticity follows after one uses Bloch periodicity conditions between the tractions and displacements (see (23)) into the boundary terms in (24), which yields

$$\begin{aligned} &\int_S t_r^*(\mathbf{x}) u_r(\mathbf{x})\, \mathrm{d}S + \int_S m_r^*(\mathbf{x}) \theta_r(\mathbf{x})\, \mathrm{d}S = \\ &\sum_p \left\{ \int_{S_p} \left[t_r^*(\mathbf{x}) u_r(\mathbf{x}) + t_r^*(\mathbf{x}+\mathbf{a}_p) u_r(\mathbf{x}+\mathbf{a}_p) \right] \mathrm{d}S_p + \right. \\ &\left. \int_{S_p} \left[m_r^*(\mathbf{x}) \theta_r(\mathbf{x}) + m_r^*(\mathbf{x}+\mathbf{a}_p) \theta_r(\mathbf{x}+\mathbf{a}_p) \right] \mathrm{d}S_p \right\}, \end{aligned} \tag{25}$$

where the index p refers to each pair of opposite sides of the boundary. Introducing the phase shifts and elaborating further gives:

$$\begin{aligned} &\int_S t_r^*(\mathbf{x}) u_r(\mathbf{x})\, \mathrm{d}S + \int_S m_r^*(\mathbf{x}) \theta_r(\mathbf{x})\, \mathrm{d}S = \\ &\sum_p \left\{ \int_{S_p} u_r(\mathbf{x}) \left[t_r^*(\mathbf{x}) + e^{-i\mathbf{k}\cdot\mathbf{a}} t_r^*(\mathbf{x}+\mathbf{a}_p) \right] \mathrm{d}S_p + \right. \\ &\left. \int_{S_p} \theta_r(\mathbf{x}) \left[m_r^*(\mathbf{x}) + e^{-i\mathbf{k}\cdot\mathbf{a}} m_r^*(\mathbf{x}+\mathbf{a}_p) \right] \mathrm{d}S_p \right\} \end{aligned} \tag{26}$$

which after taking the complex conjugate reduces to the Bloch-equilibrium condition (or the relationship between the traction vectors at opposite

faces of the cell) for the terms enclosed by the square brackets. This leads to the vanishing of the boundary terms proving the Hermiticity condition.

Positive definiteness

To demonstrate positive (semi)-definiteness it is convenient to define the total potential and kinetic energy functionals $U([u,\theta],[u,\theta])$ and $T([u,\theta],[u,\theta])$ such that

$$U([u,\theta],[u,\theta]) = \int_V \gamma_{ij}^{S*} C_{ijkl} \gamma_{ij}^{S} \,\mathrm{d}V + \int_V \alpha \gamma_{ij}^{A*} \gamma_{ij}^{A} \,\mathrm{d}V + \int_V \kappa_{ij}^{*} D_{ijkl} \kappa_{ij} \,\mathrm{d}V \,,$$
$$T([u,\theta],[u,\theta]) = \int_V \rho u_i^{*} u_i \,\mathrm{d}V + \int_V J \theta_i^{*} \theta_i \,\mathrm{d}V \,.$$

For the potential functional to be positive definite we need that the constitutive tensors are positive definite. For an isotropic material, this implies the following constraints in the material parameters:

$$\mu > 0\,, \quad \alpha > 0\,, \quad \eta > 0\,, \quad \varepsilon > 0\,,$$
$$3\lambda + 2\mu > 0\,, \quad 3\beta + 2\eta > 0\,.$$

It should be noted that there exist differences in notation in the literature for material parameters. Particularly, the symbols used by Eringen are known to be confusing since the symbol μ is used for a combination of the classic Lamé parameter and a micropolar parameter. The use of this symbol have led to incorrect inequalities, as presented by Cowin and Hassanpour and Heppler.

In order to have the condition $[u,\theta] \neq 0$, the functional T should be different from zero implying that

$$\omega_r^2 = \frac{U([u_r,\theta_r],[u_r,\theta_r])}{T([u_r,\theta_r],[u_r,\theta_r])}\,, \tag{27}$$

meaning that ω is always greater than or equal to zero. This result is in agreement with the physical meaning of angular frequency given to ω. On the other hand, the potential energy could be zero in the case of rigid body motion implying that the form U is positive semi-definite, while the form T is positive definite and so are their discrete counterparts.

FEM formulation

Finite element equations for the micropolar solid are straightforward to obtain after introducing the displacement and microrotation interpolation functions ${}_uN_i^k$ and ${}_\theta N_i^k$. Here the superscript k makes reference to the contribution from the kth node of a given element, while

the right subscript i indicates the tensorial nature of the variable being interpolated. The displacement and microrotation vectors at a given point inside the element can now be written in terms of the nodal variables u^k and θ^k as

$$u_i = {}_u N_i^k u^k, \quad \theta_i = {}_\theta N_i^k \theta^k \,. \tag{28}$$

where the summation convention for repeated indices applies for both physical and interpolation subscripts and superscripts. For the actual numerical implementation, it is convenient to express the microrotation vector θ_i in terms of its dual skew-symmetric rotation tensor θ_{ij}, such that

$$\theta_{ij} = \epsilon_{qij}\, {}_\theta N_q^k \theta^k \equiv R_{ij}^k \theta^k \,.$$

Kinematic descriptions in terms of derivatives of the primary fields u_i and θ_i follow from suitable combinations of derivatives of the primary interpolation functions. Thus,

$$\begin{aligned} \gamma_{ij}^S = B_{ij}^k u^k, \quad \omega_{ij} = \hat{W}_{ij}^k u^k, \\ \kappa_{ij} = M_{ij}^k \theta^k, \quad \gamma_{ij}^A = \hat{W}_{ij}^k u^k + R_{ij}^k \theta^k. \end{aligned} \tag{29}$$

where the tensor ω_{ij} denotes the skew-symmetric part of the displacement gradient. Substitution of (28) and (29) into (21) yields the PVW in terms of virtual nodal variables δu^k and $\delta\theta^k$

$$\begin{aligned} \delta u^k \int_v B_{ij}^k \sigma_{ij}^S \,\mathrm{d}V + \delta u^k \int_V \hat{W}_{ij}^k \sigma_{ij}^A \,\mathrm{d}V + \delta\theta^k \int_V R_{ij}^k \sigma_{ij}^A \,\mathrm{d}V \\ + \delta\theta^k \int_V M_{ij}^k \mu_{ij} \,\mathrm{d}V - \omega^2 \delta u^k \int_V \rho\, {}_u N_i^k u_i \,\mathrm{d}V - \omega^2 \delta\theta^k \int_V J\, {}_\theta N_i^k \theta_i \,\mathrm{d}V \\ - \delta u^k \int_S {}_u N_i^k t_i \,\mathrm{d}S - \delta\theta^k \int_S {}_\theta N_i^k m_i \,\mathrm{d}S = 0 \,. \end{aligned} \tag{30}$$

Using the arbitrary character of the virtual fundamental fields δu^k and $\delta\theta^k$ in (30), gives the following set of weak equilibrium equations in terms of nodal forces and couples consistent with the stresses and couple stresses;

$$\begin{aligned} \hat{f}_\tau^k + \hat{f}_\sigma^k - \hat{f}_I^k - \hat{T}^k = 0 \,, \\ \hat{m}_\sigma^k + \hat{m}_\mu^k - \hat{m}_I^k - \hat{q}^k = 0 \,. \end{aligned} \tag{31}$$

where the different terms become obvious after comparing (30) and (31). These equations describing equilibrium of forces and moments for the k-th degree of freedom can be written in the following matrix form

$$\begin{bmatrix} K_{uu}^{kp} & K_{u\theta}^{kp} \\ K_{\theta u}^{kp} & K_{\theta\theta}^{kp} \end{bmatrix} \begin{Bmatrix} u^p \\ \theta^p \end{Bmatrix} - \omega^2 \begin{bmatrix} M_{uu}^{kp} & 0 \\ 0 & M_{\theta\theta}^{kp} \end{bmatrix} \begin{Bmatrix} u^p \\ \theta^p \end{Bmatrix} = \begin{Bmatrix} f_{ext} \\ q_{ext} \end{Bmatrix}, \tag{32}$$

which results after writing the stress-strain relationships for the micropolar solid in terms of constitutive tensors C_{ijkl}, G_{ijkl} and D_{ijkl} as

$$\begin{aligned} \sigma_{ij} &= C_{ijkl}\gamma^S_{kl} + G_{ijkl}\gamma^A_{kl}\,, \\ \mu_{ij} &= D_{ijkl}\kappa_{kl}\,. \end{aligned} \tag{33}$$

For completeness, all of the terms in the matrix equation for the micropolar solid are given in the appendix of this chapter.

Imposition of the Bloch periodic boundary conditions in the system given by (31) results in a generalized eigenvalue problem of the form [Guarín-Zapata and Gomez, 2015]:

$$\left[K_R - \omega^2 M_R\right]\{\mathbf{U}_R\} = \mathbf{0}\,. \tag{34}$$

Dispersion relations for a micropolar cellular material

We now conduct a series of numerical simulations intended to test the capabilities of the micropolar model as a numerical vehicle to introduce dispersive behavior through a continuum based approach. For that purpose, we consider first the simplest case of a homogeneous material cell. This ideal case is also useful as a verification problem for the numerical implementation as that model has a closed-form dispersion relation. At the same time, the homogeneous case is used to assess the convergence of the band structure predicted by the numerical model. In a subsequent analysis, and intended to identify the sensitivity of the micropolar material parameters in the band structure, we also performed Bloch analysis for a bilayer composite. In this case, the band structures were found for different values of a single mechanical parameter, while keeping constant values for the remaining ones. As a final test, we extended our analysis to a cellular material with a microstructure corresponding to a circular pore embedded in an otherwise micropolar medium. In this case, we wanted to test the sensitivity of the dispersive response to the relative size of the pore with respect to the length scale constitutive parameter implicit in the material model.

Homogeneous material

In a homogeneous micropolar solid, dispersion relations can be obtained in closed-form (See fig. 14). Following, we present the expressions for a two-dimensional solid. The frequency-wavenumber rela-

tionships can be written in compact form as

$$\omega^{P}_{m,n} = c_1 k_{m,n}\,,$$
$$\omega^{S}_{m,n} = \sqrt{\frac{A}{2} - \frac{1}{2}\sqrt{A^2 - 4B}}\,,$$
$$\omega^{TR}_{m,n} = \sqrt{\frac{A}{2} + \frac{1}{2}\sqrt{A^2 - 4B}}\,,$$

where the constants A and B correspond to

$$A = 2Q^2 + (c_2^2 + c_4^2)k^2_{m,n}\,,$$
$$B = 2Q^2 c_2^2 k^2_{m,n} - K^2 Q^2 k^2_{m,n} + c_2^2 c_4^2 k^4_{m,n}\,,$$

and TR refers to transverse-rotational.

One difference between wave propagation in micropolar and classical elasticity is the appearance of new (rotational) propagating waves that are dispersive. These waves appear above a cut-off frequency given by $\omega_0^2 = 2Q^2$ [Nowacki, 1986]. Besides the two propagation modes mentioned above there is another one with the following frequency-wavenumber relation

$$\omega^{LR}_{m,n} = \sqrt{2Q^2 + c_3^2 k^2_{m,n}}\,,$$

where LR refers to longitudinal-rotational. This wave only exists in 3D, and will not be present in the following results.

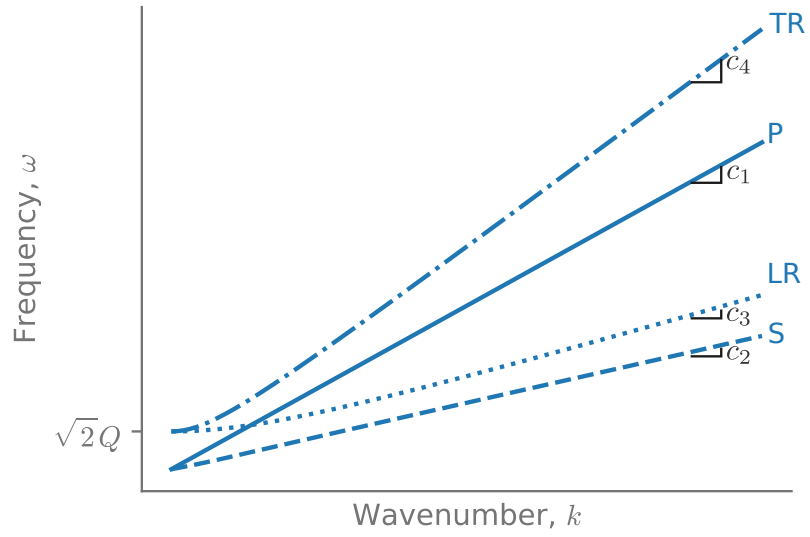

Figure 14: Qualitative depiction of the dispersion relations for a micropolar material. The different branches are: (P) non-dispersive longitudinal wave with phase/group speed c_1 as in the classical case, (S) dispersive transverse wave with limiting ($k \to \infty$) phase/group speed c_2, (LR) dispersive longitudinal-rotational (corkscrew-like) wave with limiting ($k \to \infty$) phase/group speed c_3, (TR) dispersive transverse-rotational wave wave with limiting ($k \to \infty$) phase/group speed c_4.

When conducting Bloch analysis for a 2D cell, the Bloch theorem requires that the wave number vector is swept over the first Brillouin

zone [Brillouin, 1953]. As a result, the m and n subscripts in the frequency and wave number terms represent values of the wave number along adjacent Brillouin zones and refer to waves coming from these adjacent Brillouin zones. These wave numbers are given by:

$$k_{m,n} = \sqrt{\left(k_x + \frac{m\pi}{d}\right)^2 + \left(k_y + \frac{n\pi}{d}\right)^2}. \tag{35}$$

Typical dispersion relationships are shown in fig. 15 for the mechanical parameters reported in Kulesh [2009] and corresponding to:

$$\rho = 10^5 \text{ kg/m}^3, \quad \lambda = 2.8 \times 10^{10} \text{ N/m}^2, \quad \mu = 4 \times 10^9 \text{ N/m}^2,$$
$$J = 10^4 \text{ kg/m}, \quad \eta + \varepsilon = 1.62 \times 10^9 \text{ N}, \quad \alpha = 2 \times 10^9 \text{ N/m}^2.$$

The figure 15 shows the cut-off frequency associated with the micro-rotational wave, together with the limit cases for the phase and group speeds.

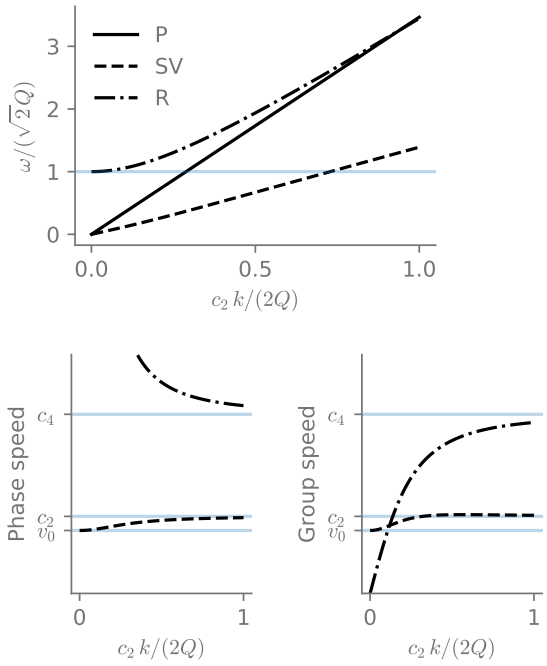

Figure 15: Dispersion relations for a homogeneous micro-polar material material with properties: $\rho = 1 \times 10^5$, $J = 1 \times 10^4$, $\lambda = 2.8 \times 10^{10}$, $\eta + \varepsilon = 1.62 \times 10^9$, $\mu = 4 \times 10^9$, $\alpha = 2 \times 10^9$ as in Kulesh [2009]. The plot on the left shows the frequency-wave number relation for the non-dispersive P-wave (continuous line) and the dispersive SV and micro-rotational wave (dashed lines). The microrotational wave is only triggered above the normalized frequency of 1. The plots in the middle and right part of the figure show the phase and group speeds for the dispersive modes.

Figure 16 compares now the analytic and numerical band structure for the micro-polar solid for the following set of material parameters:

$$\rho = 2770 \text{ kg/m}^3, \quad \lambda = 5.12 \times 10^{10} \text{ N/m}^2, \quad \mu = 2.76 \times 10^{10} \text{ N/m}^2,$$
$$J = 306.5 \text{ kg/m}, \quad \eta + \varepsilon = 7.66 \times 10^9 \text{ N}, \quad \alpha = 3.07 \times 10^9 \text{ N/m}^2.$$

The numerical curves were obtained with a mesh of 34×34 bilinear elements. The values for the classical model material parameters are

those of aluminum, while the ones for the micropolar model have been adjusted to yield a normalized cut-off frequency of 2. The figure also shows the unit material cell and the first Brillouin zone. The numerical implementation accurately predicts the propagation modes, including the micro-rotational wave, together with the analytic value of the cut-off frequency.

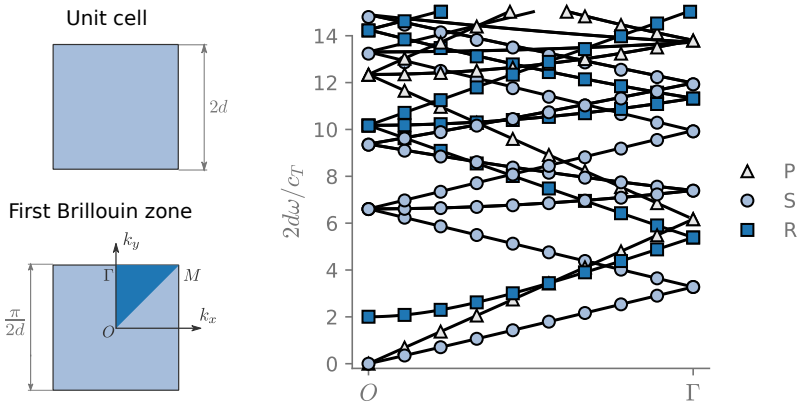

Figure 16: Dispersion relations for a homogeneous micro-polar material model. Solid lines represent FEM results while markers correspond to the analytic solution. The left part of the figure shows the unit material cell and the first Brillouin zone.

As an additional verification, we also tested the convergence in the calculation of the dispersion relations after considering the first 12 modes for a sequence of meshes of 2×2, 4×4, 8×8, and 16×16 elements. The error in the eigenvalue computation was measured according to

$$e = \frac{\|\boldsymbol{\omega}_{\text{ref}} - \boldsymbol{\omega}_h\|_2}{\|\boldsymbol{\omega}_{\text{ref}}\|_2},$$

where $\boldsymbol{u}_h$ is the set of eigenvalues (dispersion relation) for a mesh of characteristic element size h and $\boldsymbol{u}_{\text{ref}}$ is the solution corresponding to the 32×32 elements mesh, which has been taken as reference. The results for this sequence, together with the variation in the error parameter, are displayed in fig. 17. The estimated convergence rate for the eigenvalues is 1.81.

Variation of micropolar parameters in a bilayer composite

We considered a bilayer composite made with two materials that share all the properties, except for one of the micropolar parameters. Thus, we varied J, α and $\xi \equiv \eta + \varepsilon$, while keeping the other parameters fixed. Notice that the composite represents a homogeneous material in the case that both layers share the same material properties. Figure 18 shows the unit cell and the first Brillouin zone for this set of analyses.

The properties in material 2, as presented in fig. 18, are fixed. The

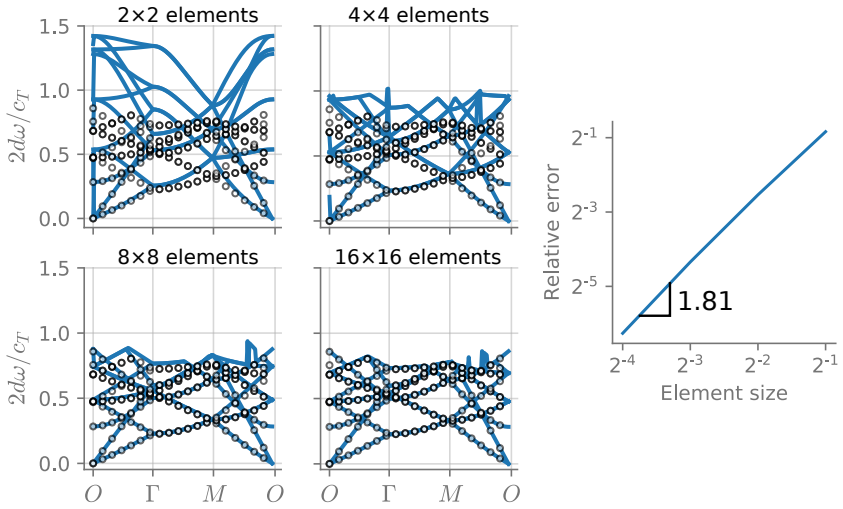

Figure 17: Convergence of the first 12 modes in the dispersion relations for a sequence of meshes with: 2×2, 4×4, 8×8, and 16×16 elements — presented as solid blue lines in the background. The results are compared with a mesh that has 32×32 elements — presented as dots in the foreground. The estimated convergence rate for the eigenvalues in the 2-norm is 1.81.

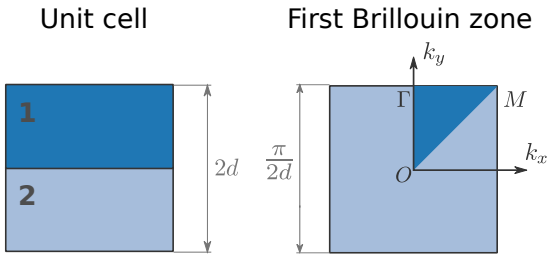

Figure 18: (Left) Schematic of the unit cell for the bilayer material. (Right) Illustration of the first Brillouin zone and the irreducible Brillouin zone.

values used are the following:

$$\rho_1 = \rho_2 = 2770\ \text{kg/m}^3\,, \qquad \lambda_1 = \lambda_2 = 5.12 \times 10^{10}\ \text{Pa}\,,$$
$$\mu_1 = \mu_2 = 2.76 \times 10^{10}\ \text{Pa}\,, \qquad \alpha_2 = 3.07 \times 10^{9}\ \text{Pa}\,,$$
$$\xi_2 = 7.66 \times 10^{10}\ \text{N}\,, \qquad J_2 = 306.5\ \text{kg/m}\,.$$

Figure 19 presents the results for variations in $J_1 \in \{30, 100, 300, 1000, 3000\}$ kg/m. The results are compared with those of the homogeneous cell shown by the black dots, while the dispersion curves resulting from variations in J_1 are described by the continuous blue line. As J_1 increases the cut-off frequency for the microrotational wave decreases, which is due to the overall increase in the inertial density. We can also highlight that for larger values of J_1 the dispersion for the SV and TR waves increases (see the results for $J_1/J_2 = 10$). This is a result of the interaction between TR and SV waves, but P waves are not affected since they do not interact when the incidence is perpendicular.

As a second modification to the set of material properties we now changed $\alpha_1 \in \{3.41 \times 10^8, 1.02 \times 10^9, 3.07 \times 10^9, 9.21 \times 10^9, 2.76 \times 10^{10}\}$ Pa. The corresponding results, in terms of dispersion curves are shown

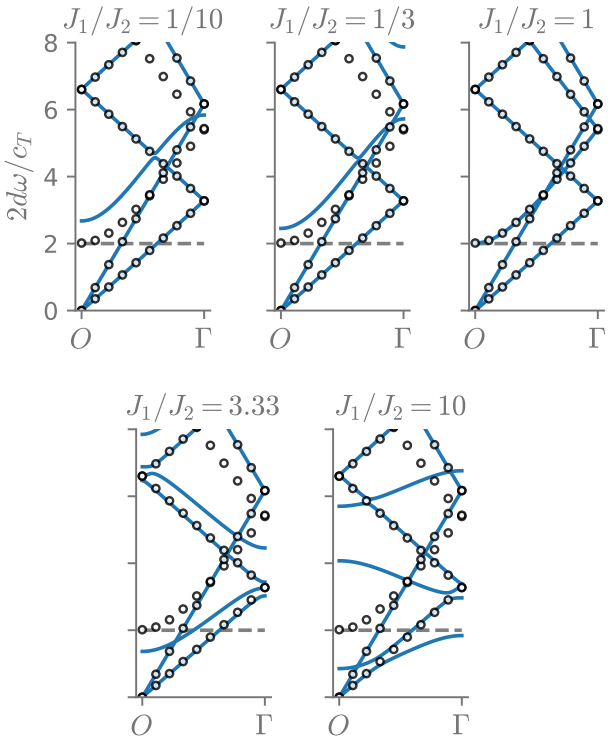

Figure 19: Dispersion curves for a bilayer composite made with two micropolar materials. All material parameters are fixed except for the inertial density J_1, which takes values in $\{30, 100, 300, 1000, 3000\}$ kg/m. The dispersion curves for the different values of J_1 correspond to the continuous blue line, while black dots show reference results corresponding to a homogeneous material cell. The increase in J_1 produces an overall increase in the inertial density accompanied by a decrease in the cut-off frequency of the microrotational wave.

in fig. 20. It is now evident how the cut-off frequency presents an opposite trend as compared with the variations in J_1, that is, the cut-off frequency increases as the ratio α_1/α_2 increases. This is also an expected result considering the overall increase in α for the composite. Furthermore, we see that we can increase the size of the (partial) bandgap by increasing the ratio α_1/α_2.

We considered as a last variation changes in the parameter $\xi_1 = \eta_1 + \epsilon_1 \in \{8.51 \times 10^8, 2.55 \times 10^9, 7.66 \times 10^9, 2.30 \times 10^{10}, 6.89 \times 10^{10}\}$ N. Although this parameter changes the dispersive response, the cut-off frequency for the micro-rotational wave remains unmodified, as Q is independent of ξ and therefore the cut-off frequency is independent of the overall modulus of the composite. Although we see some (partial) bandgaps when changing the ratio ξ_1/ξ_2, it is more interesting to highlight how the hybridization between SV and TR modes changes across the different values of the ratio.

Variation of microstructural length

Although the micropolar medium introduces dispersive behavior through the presence of length scale parameters, additional frequency dependence of the wave propagation velocity in the medium can be obtained if we explicitly consider the presence of microstructural features em-

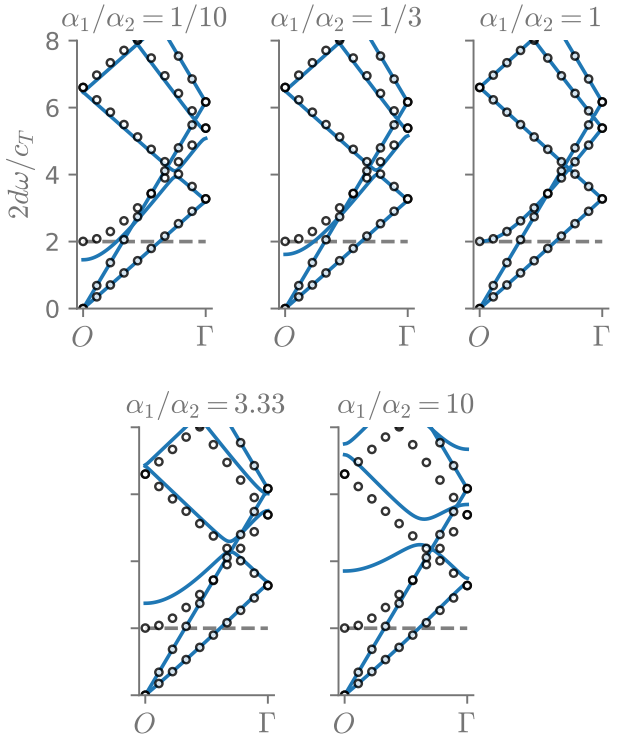

Figure 20: Dispersion curves for a bilayer composite made with two micropolar materials. All material parameters are fixed except for α_1, which takes values in $\{3.41 \times 10^8, 1.02 \times 10^9, 3.07 \times 10^9, 9.21 \times 10^9, 2.76 \times 10^{10}\}$ Pa. The dispersion curves for the different values of α_1 correspond to the continuous blue line, while the black dots show reference results corresponding to a homogeneous material cell. The overall increase of the α parameter for the composite produces a decrease in the cut-off frequency and an increase in the dispersion for the SV waves.

bedded in the micropolar medium (fig. 22). Here we explore a material cell which is composed of a circular pore of diameter d embedded inside a micropolar medium.

We will assume a pore with a diameter that is $1/2$ of the cell length or equivalently a porosity of $\pi/16 \approx 0.196$. This value is kept fixed as we modify the size of the unit cell. We will use the following set of mechanical parameters for the micropolar model:

$$\rho = 2770 \text{ kg/m}^3\,, \qquad \lambda = 5.12 \times 10^{10} \text{ Pa}\,,$$
$$\mu = 2.76 \times 10^{10} \text{ Pa}\,, \qquad \alpha = 3.07 \times 10^9 \text{ Pa}\,,$$
$$\eta + \varepsilon = 7.66 \times 10^{10} \text{ N}\,, \qquad J = 306.5 \text{ kg/m}\,.$$

For the size effect analysis, it is convenient to express the mechanical parameter in terms of a constitutive length scale present in the micropolar model as discussed in [5] and given by:

$$\ell^2 \equiv \frac{\eta + \varepsilon}{2\mu} = 0.3725 \text{ m}\,,$$

in which $2\mu\ell^2$ represents the rotational stiffness of the material [Trovalusci et al., 2015]. Notice that a change in the size of the unit cell implies a change in the pore diameter and therefore a change in the ratio between the intrinsic length scale ℓ and the characteristic microstructural

[5] S. C. Cowin. Stress functions for Cosserat elasticity. *International Journal of Solids and Structures*, 6(4):389–398, 1970a

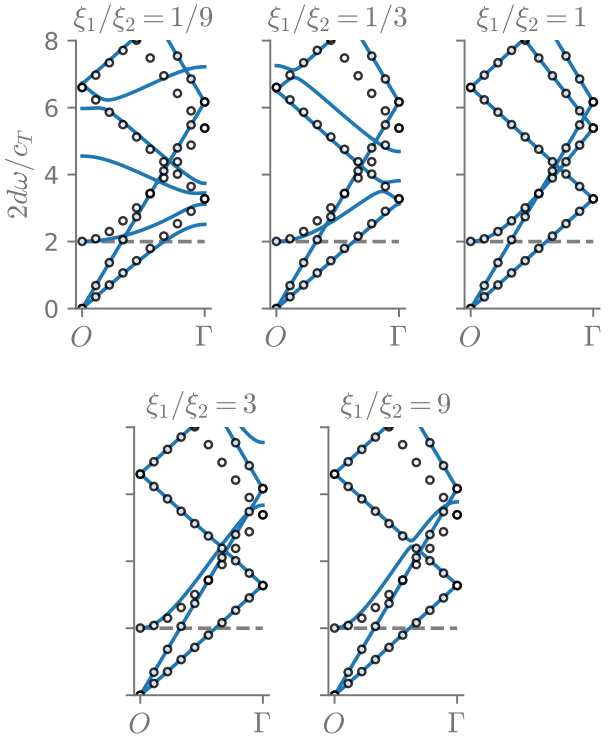

Figure 21: Dispersion curves for a bilayer composite made with two micropolar materials. All material parameters are fixed except for ξ_1, which takes values in $\{8.51 \times 10^8, 2.55 \times 10^9, 7.66 \times 10^9, 2.30 \times 10^{10}, 6.89 \times 10^{10}\}$ N. The dispersion curves for the different values of ξ_1 correspond to the continuous blue line, while the black dots show reference results corresponding to a homogeneous material cell. In this case the cut-off frequency remains unmodified as Q is independent of ξ.

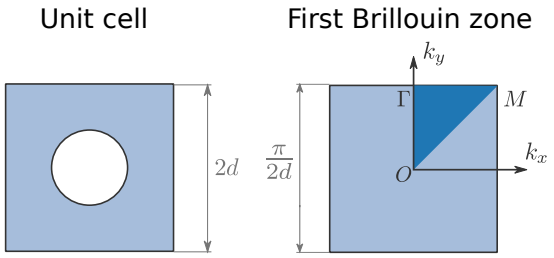

Figure 22: (Left) Schematic of the unit cell for the porous material. (Right) Illustration of the first Brillouin zone and the irreducible Brillouin zone.

dimension d/ℓ. This variation in the dispersion relations with the ratio d/ℓ is shown in fig. 23.

Directionality in cellular material with a circular pore

As a final result, we computed the directionality curves for cellular materials with circular pores—see previous chapter for further details on the definition of the directionality. We changed the diameter of the pore keeping fixed the size of the cell. The material properties used are the same as in the previous section. We compare the directionality results in a qualitative fashion, showing how different directions present different phase/group speeds when changing the porosity. This comparison is only valid for small wavenumber, because near the edges of

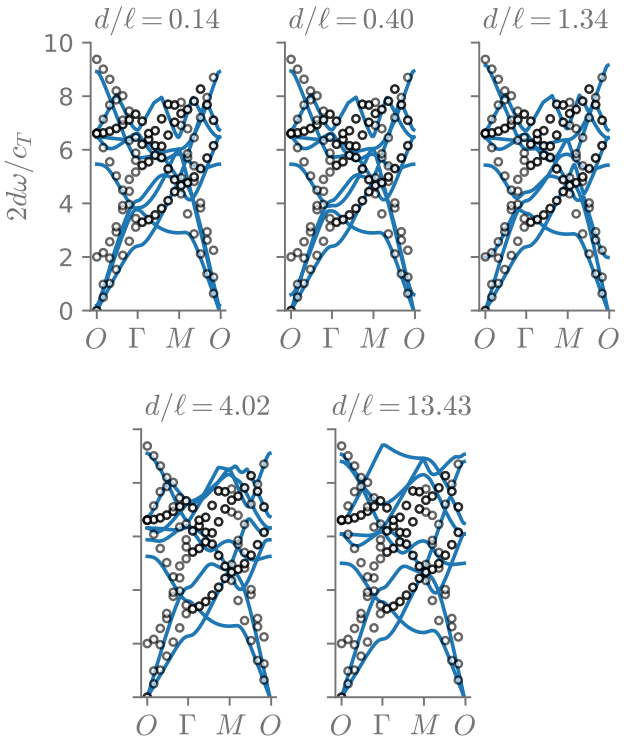

Figure 23: Variation in the band structure for a micropolar periodic cellular material with circular pores for different values of the ratio d/ℓ.

the first Brillouin zone the different branches might intersect and the resulting contours would contain information from mixed modes.

Figure 24 presents the directionality curves for the first three branches of the dispersion relations for cellular materials with increasing porosity with values: 0.000, 0.196, 0.503 and 0.709. A porosity of 0 represents a homogeneous material, used as reference in this case. The directionality (anisotropy) of the material increases for higher porosity values.

The first branch presents lower phase speed along the vertical and horizontal directions, while the opposite happens for the second mode. This is expected since these two modes represent quasi-transversal and quasi-longitudinal propagations modes for small wavenumbers. Furthermore, the first mode is the one that presents a higher change in directionality. We can also see that the anisotropy for the third branch is more sensitive to the wavenumber than the porosity, being (almost) isotropic for small wavenumbers.

Conclusions

We discussed several theoretical and simulation aspects related to a Cosserat-like micropolar medium. In particular, we address the model capabilities to capture dispersive behavior through its kinematic as-

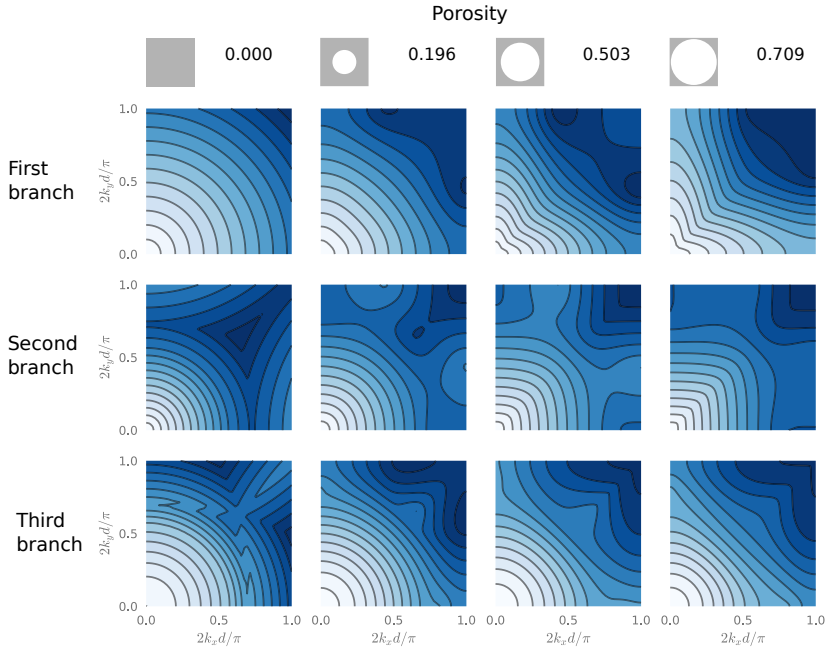

Figure 24: Directionality curves for cellular materials with increasing porosity for the first three branches. The corresponding porosities are: 0.000, 0.196, 0.503 and 0.709. The porosity increases from left to right and is presented at the top. A porosity of 0 represents a homogeneous material, used as reference in this case.

sumptions and constitutive parameters. For that purpose, we used the theory of phononic crystals, where the band structure of the material is found from the analysis of Floquet-Bloch periodicity conditions. Within that context we considered unit material cells corresponding to a homogeneous material, a bilayer composite and a porous cell composed of a circular cavity embedded in a micropolar matrix. The dispersive properties in each case were measured in terms of the variation in the cut-off frequency of the microrotational wave for the different considered values of the mechanical and geometric parameters of the model. We found that the ability of the micropolar medium to capture dispersive behavior can be increased mainly through changes in the rotational inertia of the material and the length scale parameter associated to its bending stiffness. Furthermore, these results can serve as a benchmark for a program of physical experiments on periodic solids to explore the existence of microrotational waves, as predicted by micropolar theory.

Terms for the finite element equilibrium equations in the micropolar solid

The discrete finite element equilibrium equations for the micropolar solid were written as

$$\begin{bmatrix} K_{uu}^{kp} & K_{u\theta}^{kp} \\ K_{\theta u}^{kp} & K_{\theta\theta}^{kp} \end{bmatrix} \begin{Bmatrix} u^p \\ \theta^p \end{Bmatrix} - \omega^2 \begin{bmatrix} M_{uu}^{kp} & 0 \\ 0 & M_{\theta\theta}^{kp} \end{bmatrix} \begin{Bmatrix} u^p \\ \theta^p \end{Bmatrix} = \begin{Bmatrix} f_{ext} \\ q_{ext} \end{Bmatrix}, \tag{36}$$

where each one of the terms are defined next as follows,

$$K_{uu}^{kp} = \int_V B_{ij}^k C_{ijrs} B_{rs}^p \,\mathrm{d}V + \int_V \hat{W}_{ij}^k G_{ijrs} \hat{W}_{rs}^p \,\mathrm{d}V \equiv \int_V B_{ij}^k C_{ijrs} B_{rs}^p \,\mathrm{d}V + \int_V \mu_c \hat{W}_{ij}^k \hat{W}_{ij}^p \,\mathrm{d}V \ ,$$

which is symmetric.

$$\begin{aligned} K_{u\theta}^{kp} &= \int_V \hat{W}_{ij}^k G_{ijrs} R_{rs}^p \,\mathrm{d}V \equiv \int_V \alpha \hat{W}_{ij}^k R_{rs}^p \,\mathrm{d}V \\ K_{\theta u}^{kp} &= \int_V R_{ij}^k G_{ijrs} \hat{W}_{rs}^p \,\mathrm{d}V \equiv \int_V \alpha R_{ij}^k \hat{W}_{rs}^p \,\mathrm{d}V \ , \end{aligned}$$

with $K_{u\theta}^{kp} = \left(K_{\theta u}^{kp}\right)^T$.

$$K_{\theta\theta}^{kp} = \int_V R_{ij}^k G_{ijrs} R_{rs}^p \,\mathrm{d}V + \int_V M_{ij}^k D_{ijrs} M_{rs}^p \,\mathrm{d}V \equiv \int_V \alpha R_{ij}^k R_{rs}^p \,\mathrm{d}V + \int_V M_{ij}^k D_{ijrs} M_{rs}^p \,\mathrm{d}V \ ,$$

which is also symmetric.

Similarly, the inertial terms, which are both symmetric, are defined as

$$\begin{aligned} M_{uu}^{kp} &= \int_V \rho \ {}_u N_i^k \ {}_u N_i^p \,\mathrm{d}V \\ M_{\theta\theta}^{kp} &= \int_V J \ {}_\theta N_i^k \ {}_\theta N_j^p \,\mathrm{d}V \, . \end{aligned}$$

Finally, the external force and couple vectors read

$$\begin{aligned} f_{ext}^p &= \int_S \ {}_u N_i^p t_i \,\mathrm{d}S \ , \\ q_{ext}^p &= \int_S \ {}_\theta N_i^p m_i \,\mathrm{d}S \ . \end{aligned}$$

In-plane equations of motion

The equations of motion for waves in the plane are the following:

$$\frac{\lambda+2\mu}{\rho}\left[\frac{\partial^2 u_x}{\partial x^2}+\frac{\partial^2 u_y}{\partial y \partial x}\right]-\frac{\mu+\alpha}{\rho}\left[\frac{\partial^2 u_y}{\partial y \partial x}-\frac{\partial^2 u_x}{\partial y^2}\right]+\frac{2\alpha}{\rho}\frac{\partial \theta_z}{\partial y}=-\omega^2 u_x\,,$$
$$\frac{\lambda+2\mu}{\rho}\left[\frac{\partial^2 u_x}{\partial y \partial x}+\frac{\partial^2 u_y}{\partial y^2}\right]-\frac{\mu+\alpha}{\rho}\left[\frac{\partial^2 u_x}{\partial y \partial x}-\frac{\partial^2 u_y}{\partial x^2}\right]-\frac{2\alpha}{\rho}\frac{\partial \theta_z}{\partial y}=-\omega^2 u_y\,,$$
$$\frac{2\alpha}{J}\left[\frac{\partial u_y}{\partial x}-\frac{\partial u_x}{\partial y}\right]+\frac{\eta+\varepsilon}{J}\left[\frac{\partial^2 \theta_z}{\partial x^2}+\frac{\partial^2 \theta_z}{\partial y^2}\right]-\frac{4\alpha}{J}\theta_z=-\omega^2\theta_z\,,$$

notice that the equations do not involve the parameter β.

We can write the constitutive equations in extended Voigt's notation as

$$\begin{Bmatrix}\sigma_{xx}\\ \sigma_{yy}\\ \sigma_{xy}\\ \sigma_{yx}\\ \mu_{zx}\\ \mu_{zy}\end{Bmatrix}=\begin{bmatrix}\lambda+2\mu & \lambda & 0 & 0 & 0 & 0\\ \lambda & \lambda+2\mu & 0 & 0 & 0 & 0\\ 0 & 0 & \mu+\alpha & \mu-\alpha & 0 & 0\\ 0 & 0 & \mu-\alpha & \mu+\alpha & 0 & 0\\ 0 & 0 & 0 & 0 & \eta+\varepsilon & 0\\ 0 & 0 & 0 & 0 & 0 & \eta+\varepsilon\end{bmatrix}\begin{Bmatrix}\gamma_{xx}\\ \gamma_{yy}\\ \gamma_{xy}\\ \gamma_{yx}\\ \kappa_{zx}\\ \kappa_{zy}\end{Bmatrix},$$

where

$$\gamma_{xx}=\frac{\partial u_x}{\partial x},\quad \gamma_{yy}=\frac{\partial u_y}{\partial y},$$
$$\gamma_{xy}=\frac{\partial u_y}{\partial x}+\theta_z,\quad \gamma_{yx}=\frac{\partial u_x}{\partial y}-\theta_z,$$
$$\kappa_{zx}=\frac{\partial \theta_z}{\partial x},\quad \kappa_{zy}=\frac{\partial \theta_z}{\partial y}.$$

Waves in periodic C-CST solids

Introduction

There has been significant interest, especially in recent years, to develop spatially periodic band gap materials and structures, based upon Floquet-Bloch theory [Floquet, 1883, Bloch, 1929]. Recent developments in the field of architected materials aimed at achieving novel mechanical properties often rely on enhancements that include effects neglected by classical theories. Continuum models with local microstructural interactions have become increasingly popular after the advance and growth in the field of metamaterials, as summarized in the monograph by Banerjee. A family of models that has regained popularity in the last few years is the so-called Cosserat-based theories, which are mainly founded on the formulation by Cosserat and Cosserat. In a wide sense, these material models consider microstructural effects through a generalization of Cauchy's postulate to include additional mechanical interactions involving couples per unit surface or couple-stresses. In the present work, we focus on a pure continuum mechanics representation by widening the modeling capabilities of consistent-couple stress theory (C-CST), originally formulated in [6]. In particular, we establish a principle of stationary correlated action for the corresponding reduced wave equation of elastodynamics and extend the theory to spatially periodic materials, thus providing an objective physical basis to characterize material through its dispersive behaviour.

[6] Ali R Hadjesfandiari and Gary F Dargush. Couple stress theory for solids. *International Journal of Solids and Structures*, 48(18):2496–2510, 2011

The entire family of Cosserat elasticity models depart from the classical Cauchy models in the consideration of microstructural effects, which are unavoidably expected to occur once the specimen dimensions become comparable to the material microstructural features. These effects cannot be addressed in classical theories. On the other hand, microstructural effects are introduced through the extension of dynamic and kinematic descriptors from classical continuum mechanics on a range of alternative models. Voigt was probably the first to postulate a model with asymmetric mechanical interactions in terms of couple-stresses: the interaction between two material points in this

continuum encompassed couples per unit contact surface in addition to the classical Cauchy forces per unit surface. In a landmark contribution, the Cosserat brothers [Cosserat and Cosserat, 1909] formulated a mathematical theory involving couple-stresses in which new kinematic variables were introduced in the form independent micro-rotations. Various later extensions from these theories were also developed by Eringen, Nowacki, Mindlin, Eringen and Suhubi in micropolar, microstretch and micromorphic theories. Alongside, a different branch of developments resulted in a set of couple stress theories in the work by Toupin, Mindlin and Tiersten, Koiter, who used the gradients of the true continuum rotation field to provide the required kinematic enrichment.

Recent developments from Hadjesfandiari and Dargush have resulted in a consistent version of the models by Toupin, Mindlin and Tiersten, Koiter in terms of couple-stresses. The consistency of this model is reflected in the determinacy of all the force-stress and couple-stress components, the identification of the necessary and sufficient set of natural and essential boundary conditions and the elimination of redundant force components. This present work seeks to extend C-CST and to explore its capability to study continuum distributions of matter under dynamic response. An objective approach for evaluating the usefulness and robustness of a continuum mechanics model is through the determination of its band structure in terms of its dispersion relationships. These indicate the kinematic response of the material through an identification of the wave propagation modes that can exist within the model and the frequency dependency of the group and phase velocities of these potential waves. An effective technique, relying on the assumption of spatial periodicity, is based on Bloch's theorem from solid state physics [Brillouin, 1953], where the problem of finding the band structure reduces to solving a series of generalized eigenvalue problems for a variation of the wave vector in the reciprocal space. In the case of the C-CST model, this problem poses several computational challenges. First, since the enriched kinematic variables are now curvatures, corresponding to particular second order gradients of the displacement field, the displacement-based finite element formulation now would require C^1 interelement continuity. As shown by Darrall et al., this numerical issue can be resolved by introducing Lagrange multiplier techniques, however it is not obvious how to incorporate these within Bloch analysis. Second, as a result of enforcing the kinematic constraint in terms of Lagrange multipliers, the computational framework lacks inertial components associated with the rotational interactions. Since there is only a mass matrix associated with the translational degrees of freedom, special attention is needed in solving the eigenproblem.

Here we establish a new variational principle in the temporal frequency domain for reduced couple stress elastodynamics and then extend the finite element algorithm from Darrall et al. to the case of spatially periodic material cells with Bloch boundary conditions. We examine first the closed form dispersion relationships for the homogeneous version of the model. This homogeneous model already involves electromechanical effects through a length scale material parameter, however additional effects can be considered in terms of explicit representations of geometric features at the fundamental material cell level. We then formulate a variational statement together with the imposition of Bloch periodic boundary conditions that satisfies Hermiticity and positive definiteness. Subsequently, this statement is modified by introducing an artificial independent rotation field tied to the continuum displacement field through the enforcement of a Lagrange multiplier field that is shown to equal the skew-symmetric part of the force-stresses. The resulting numerical framework is tested by comparing its results with those obtained in closed form for the homogeneous case and by applying it to a porous periodic material cell design, which displays interesting band gap behavior.

Governing equations

Forces and moments in the C-CST solid

The fundamental signature of the extended continuum model considered in this work is the presence of rotational mechanical interaction, in addition to the classical translational interaction between material points in the continuum. Following a generalized Cauchy's postulate [Mindlin and Tiersten, 1962, Koiter, 1964] we define force and couple traction vectors $t_i^{(\hat{n})}$ and $m_i^{(\hat{n})}$ respectively as

$$t_i^{(\hat{n})} = \lim_{\Delta S(\hat{n})\to 0} \frac{\Delta R_i}{\Delta S(\hat{n})} \tag{37a}$$

$$m_i^{(\hat{n})} = \lim_{\Delta S(\hat{n})\to 0} \frac{\Delta M_i}{\Delta S(\hat{n})}\,, \tag{37b}$$

and where $\Delta S(\hat{n}))$ is a small element of area oriented with $\hat{n}$ while ΔR_i and ΔM_i are the resultant force and moment. However, only the tangential components of $m_i^{(\hat{)})}$ exist (Figure 25).

Note that while the force-tractions vector $t_i^{(\hat{n})}$ is a polar vector, the couple-tractions vector $m_i^{(\hat{n})}$ is an axial vector. Force-tractions and couple-tractions are also described by projections of the non-symmetric

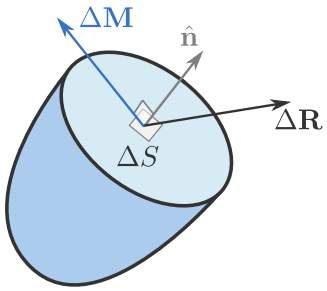

Figure 25: In the C-CST model microstructural effects are described through rotational interactions in terms of resultant moments at the material point in addition to resultant forces. These resultants act at the surface element ΔS over a plane whose normal is $\hat{n}$.

force-stress tensor σ_{ij} and the couple-stress μ_{ij} tensors according to:

$$t_i^{(\hat{n})} = \sigma_{ji} n_j \,, \tag{38a}$$

$$m_i^{(\hat{n})} = \mu_{ji} n_j \,, \tag{38b}$$

where μ_{ij} is skew-symmetric. Thus, $\mu_{ij} = -\mu_{ji}$ and the couple-stress tensor can be written as a polar vector with

$$\mu_k = \frac{1}{2} \epsilon_{kji} \mu_{ji} \,,$$

where ϵ_{ijk} is the Levi-Civita permutation symbol.

Consideration of the linear and angular balance equations for an arbitrary part of the material continuum of volume V, bounded by external surface S leads to the following stress and couple stress equilibrium equations for the C-CST model:

$$\begin{aligned} \sigma_{ji,j} + f_i &= \rho \ddot{u}_i \,, \\ \mu_{ji,j} + \epsilon_{ijk} \sigma_{jk} &= 0 \,, \end{aligned} \tag{39}$$

where f_i are forces per unit volume, and ρ is the mass density. Notice that, in contrast to micropolar models [Guarín-Zapata et al., 2020] where there is a rotational inertial density and a body couple term, in this model the balance equations already include those contributions. This particular aspect of the C-CST model is discussed in the original paper by Hadjesfandiari and Dargush where it is also proved that from

$$\epsilon_{ijk} (\mu_{k,j} + \sigma_{jk}) = 0 \,, \tag{40}$$

it follows that $\mu_{k,j} + \sigma_{jk}$ is symmetric and as a result its skew-symmetric part is zero leading to

$$\sigma_{[ji]} = -\mu_{[i,j]} \,.$$

This also gives the skew-symmetric part of the force-stress tensor in terms of the couple-stress vector. The force-stress tensor also can be described by its dual vector representation

$$s_i = \frac{1}{2} \epsilon_{ijk} \mu_{k,j} \,.$$

Kinematics and constitutive relations

In the linear C-CST model, kinematics is described by the classical infinitesimal strain (e_{ij}) and rotation (θ_{ij}) tensors

$$e_{ij} = \frac{1}{2}(u_{i,j} + u_{j,i})\,, \tag{41a}$$

$$\theta_{ij} = \frac{1}{2}(u_{i,j} - u_{j,i})\,, \tag{41b}$$

and by the mean curvature tensor

$$\kappa_{ij} = \frac{1}{2}(\theta_{i,j} - \theta_{j,i})\,, \tag{42}$$

where

$$\theta_i = \frac{1}{2}\epsilon_{ijk}\theta_{kj}\,.$$

Equation (42) can also be written in polar form, as an engineering curvature vector [Darrall et al., 2014]

$$\kappa_i = \epsilon_{ijk}\theta_{j,k} = \frac{1}{2}(u_{i,kk} - u_{k,ik}) \tag{43}$$

since

$$\kappa_i = \epsilon_{ijk}\kappa_{jk}\,.$$

For a linear elastic centrosymmetric C-CST continuum, the constitutive equations can be written as

$$\begin{aligned} \sigma_{(ij)} &= C_{ijkl}e_{kl}\,, \\ \mu_i &= D_{ij}\kappa_j\,, \end{aligned} \tag{44}$$

where C_{ijjkl} is the stiffness tensor as in classical (anisotropic) elasticity, and D_{ij} is an additional material tensor that accounts for couple-stress effects. In the expressions above, parentheses as subindices are used to indicate the symmetric part of the tensor. In the case of a linear isotropic elastic C-CST continuum,

$$\begin{aligned} C_{ijkl} &= \lambda\delta_{ij}\delta_{kl} + \mu(\delta_{ik}\delta_{jl} + \delta_{il}\delta_{jk}), \\ D_{ij} &= \eta\delta_{ij}, \end{aligned} \tag{45}$$

where μ and λ are the Lamé parameters as in classical elasticity, while η is the additional material coefficient that accounts for couple-stress effects. Then, the constitutive equations for isotropy can be simplified to

$$\begin{aligned} \sigma_{(ij)} &= \lambda e_{kk}\delta_{ij} + 2\mu e_{ij}\,, \\ \mu_i &= 4\eta\kappa_i\,. \end{aligned} \tag{46}$$

Displacement equations of motion

At this point it may be convenient to alternate between index and explicit vector notation. In the latter, the gradient operator reads $\nabla = \frac{\partial}{\partial x_i}$ in Cartesian coordinates. In these terms, the time domain displacement equations of motion are obtained after using the constitutive relations (46) in the equilibrium equations (39) yielding

$$(\lambda + 2\mu)\nabla(\nabla \cdot \mathbf{u}) - \mu\nabla \times \nabla \times \mathbf{u} + \eta\nabla^2\nabla \times \nabla \times \mathbf{u} = \rho\ddot{\mathbf{u}}\,. \tag{47}$$

Defining the phase/group speed for the longitudinal (P) wave c_1 (which is not dispersive), the low-frequency ($k \to 0$) phase/group speed for the transverse wave (S) c_2 (which is dispersive) and the intrinsic material length scale parameter l (which is not present in classical elasticity), such that

$$c_1^2 = \frac{\lambda + 2\mu}{\rho}\,, \qquad c_2^2 = \frac{\mu}{\rho}\,, \qquad l^2 = \frac{\eta}{\mu}\,, \tag{48}$$

allows us to write (47) in the form

$$c_1^2\nabla(\nabla \cdot \mathbf{u}) - c_2^2(1 - l^2\nabla^2)\nabla \times \nabla \times \mathbf{u} = \ddot{\mathbf{u}}\,. \tag{49}$$

Dispersion relations for unbounded domains

Using a Helmholtz decomposition, the displacement field can be written in terms of the scalar and vector potentials φ and $\mathbf{H}$ [Arfken et al., 2005] as

$$\mathbf{u} = \nabla\varphi + \nabla \times \mathbf{H}\,, \quad \nabla \cdot \mathbf{H} = 0\,,$$

and replacing this in (49) gives the following set of uncoupled wave equations

$$c_1^2\nabla^2\varphi = \ddot{\varphi}\,, \tag{50}$$
$$c_2^2(1 - l^2\nabla^2)\mathbf{H} = \ddot{\mathbf{H}}\,, \tag{51}$$

where it is observed that the equation for the rotational potential follows a higher-order wave equation that is inherently dispersive. This becomes evident after assuming a solution of the form $\mathbf{u} = \tilde{\mathbf{u}}e^{ikx - i\omega t}$ which gives the dispersion relations

$$\omega_P^2 = c_1^2k^2\,, \tag{52}$$
$$\omega_S^2 = c_2^2k^2(1 + k^2l^2)\,. \tag{53}$$

Solving the above for k, we have in each case

$$k_P^2 = \frac{\omega^2}{c_1^2}\,, \qquad k_S^2 = \frac{1}{2l^2}\left[\pm\sqrt{1 + \frac{4\omega^2l^2}{c_2^2}} - 1\right]\,.$$

Noticing that the quantity inside the square root is always greater than 1 indicates that we should consider only the positive root, while the negative root corresponds to an evanescent wave that should arise under certain boundary conditions. The phase and group speeds are now given by

$$v_P = c_1\,, \qquad g_P = c_1\,,$$
$$v_S(k) = c_2\sqrt{1+k^2l^2}\,, \qquad g_S = c_2\frac{1+2k^2l^2}{\sqrt{1+k^2l^2}}\,.$$

Taking the low and high frequency limits $k \to 0$ and $k \to \infty$ gives

$$\lim_{k\to 0} v_S = \lim_{k\to 0} g_S = c_2\,,$$
$$\lim_{k\to \infty} v_S = \lim_{k\to \infty} g_S \to \infty\,,$$

which shows how the speed of energy flow increases with frequency.

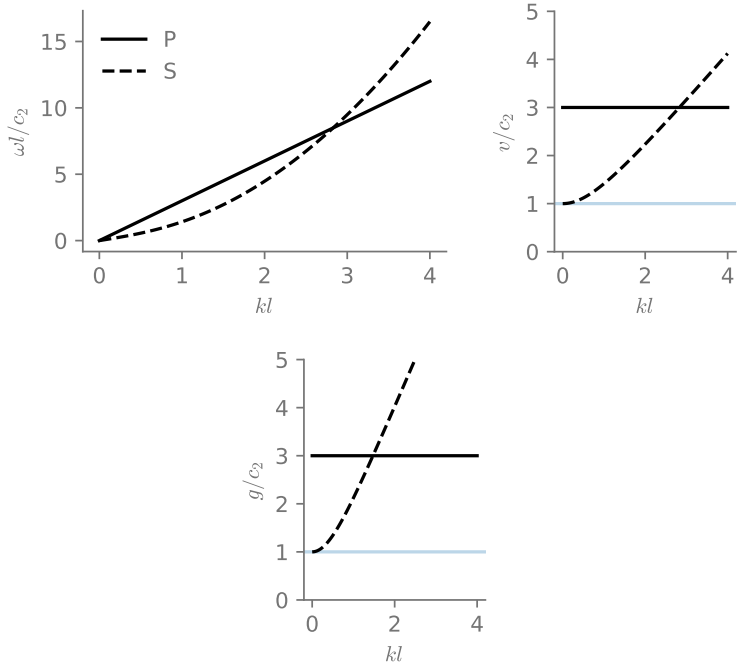

Figure 26: Dispersion relations for a homogeneous C-CST material material with properties: $\rho = 1\times10^5$, $\lambda = 2.8\times10^{10}$, $\eta = 1.62\times10^9$, $\mu = 4\times10^9$. The plot on the left shows the frequency-wave number relation for the non-dispersive P-wave (continuous line) and the dispersive SV (dashed lines). The plots in the middle and right part of the figure show the phase and group speeds for the dispersive modes.

Frequency domain equations

Bloch analysis considering spatial periodicity of the material is naturally conducted in the Fourier domain, involving both the temporal frequencies and spatial wave numbers. After performing a Fourier transform of the linear and angular momentum equations (39) to the

temporal frequency domain, these become

$$\begin{aligned} \tilde{\sigma}_{ji,j} + \tilde{f}_i &= -\rho\omega^2 \tilde{u}_i \,, \\ \tilde{\mu}_{ji,j} + \epsilon_{ijk}\tilde{\sigma}_{jk} &= 0 \,, \end{aligned} \tag{54}$$

where the superposed tilde denotes a complex Fourier amplitude.

After introducing the constitutive equations (44) for centrosymmetric materials into (54) and then combining the angular momentum and linear momentum balance laws into a single set in terms of displacement, one finds:

$$(C_{ijkl}\tilde{u}_{k,l})_{,j} + \frac{1}{4}\epsilon_{pij}\epsilon_{pmn}\{D_{nk}(\tilde{u}_{k,ll} - \tilde{u}_{l,kl})\}_{,mj} + f_i = -\rho\omega^2\tilde{u}_i \tag{55}$$

Substituting (45) and (48) for isotropic materials into (55) provides the corresponding Fourier domain reduced wave equations in the absence of body forces, which can be written

$$c_1^2\nabla(\nabla\cdot\tilde{\mathbf{u}}) - c_2^2(1 - l^2\nabla^2)\nabla\times\nabla\times\tilde{\mathbf{u}} = -\omega^2\tilde{\mathbf{u}}\,. \tag{56}$$

Notice that (56) is the temporal Fourier transform of (49).

Variational principles

We will describe next a variational formulation for the elastodynamic C-CST model. An inherent complexity is the presence of second order displacement gradients arising in the curvatures (43), which requires C^1 continuity of the displacement field.

Let us consider a volume V with boundary S, having specified body forces f_i, force-tractions t_i, and couple-tractions m_i (see fig. 27). The boundary S is split into different segments, where S_u represents the portion of S with specified displacements, S_t represents the surface with prescribed tractions, S_θ represents the segment with enforced rotations, and S_m the boundary with prescribed couple-tractions. Additionally, $S = S_u \cup S_t = S_\theta \cup S_m$ and $S_u \cap S_t = S_\theta \cap S_m = \emptyset$. In general, S_u and S_t might overlap with S_θ and S_m. This is an important aspect of the C-CST model that is relevant in the solution of boundary value problems, as we shall see later.

We begin with the following couple stress elastodynamic action functional in the frequency domain, as an extension of the elastostatic formulations introduced by Hadjesfandiari and Dargush and Darrall et al.:

$$\mathcal{A}[u;\omega] = \mathcal{U}[u;\omega] + \mathcal{T}[u;\omega] + \mathcal{V}[u;\omega], \tag{57}$$

Here, and in the remainder of this paper, the superposed tilde has been suppressed for notational convenience. Meanwhile, the elastic, kinetic

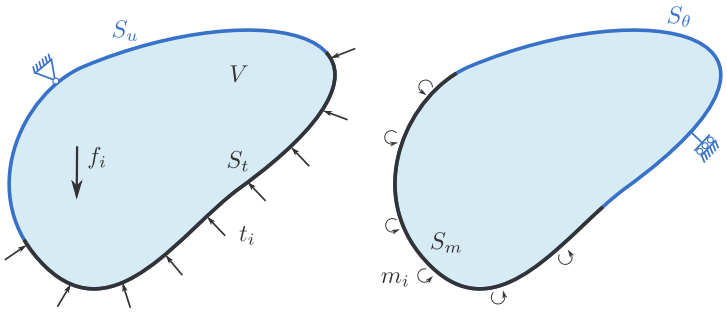

Figure 27: Schematic representation of the domain and boundary conditions for the C-CST model.

and applied load actions can be written in explicit form, respectively, as

$$\mathcal{U}[u;\omega] = \frac{1}{2}\int_V e_{ij}^* C_{ijkl} e_{kl}\,\mathrm{d}V + \frac{1}{2}\int_V \kappa_i^* D_{ij}\kappa_j\,\mathrm{d}V\,, \tag{58}$$

$$\mathcal{T}[u;\omega] = -\frac{\omega^2}{2}\int_V u_i^*\rho u_i\,\mathrm{d}V\,, \tag{59}$$

$$\mathcal{V}[u;\omega] = -\int_V u_i^* f_i\,\mathrm{d}V - \int_{S_t} u_i^* t_i^{(\hat{n})}\,\mathrm{d}S - \int_{S_m} \theta_i^* m_i^{(\hat{n})}\,\mathrm{d}S\,. \tag{60}$$

with the asterisk denoting complex conjugate.

The stationarity of this action becomes

$$\delta\mathcal{A}[u;\omega] = \delta\mathcal{U}[u;\omega] + \delta\mathcal{T}[u;\omega] + \delta\mathcal{V}[u,\omega]) = 0, \tag{61}$$

or

$$\begin{aligned}\delta\mathcal{A}[u;\omega] = &\int_V \delta e_{ij}^* C_{ijkl} e_{kl}\,\mathrm{d}V + \int_V \delta\kappa_i^* D_{ij}\kappa_j\,\mathrm{d}V - \omega^2\int_V \delta u_i^*\rho u_i\,\mathrm{d}V \\ &- \int_V \delta u_i^* f_i\,\mathrm{d}V - \int_{S_t} \delta u_i^* t_i^{(\hat{n})}\,\mathrm{d}S - \int_{S_m} \delta\theta_i^* m_i^{(\hat{n})}\,\mathrm{d}S = 0,\end{aligned} \tag{62}$$

which can serve as the weak form for a finite element formulation in reduced elastodynamics. With the appearance of mean curvature in (62), this would require C^1 spatial continuity of displacements u_i.

Next, let us derive the Euler-Lagrange equations associated with the functional $\mathcal{A}[u;\omega]$. Starting from the first variation in (62), we repeatedly apply integration-by-parts operations and the divergence theorem to shift all of the spatial derivatives from the virtual fields to

the real fields. This leads to the following statement:

$$\begin{aligned}&\int_V \delta u_i^*[(C_{ijkl}u_{k,l})_{,j} + \frac{1}{4}\epsilon_{pij}\epsilon_{pmn}\{D_{nk}(u_{k,ll} - u_{l,kl})\}_{,mj} + f_i + \rho\omega^2 u_i]\,\mathrm{d}V \\ &+ \int_{S_t} \delta u_i^*[t_i^{(\hat{n})} - \sigma_{ji}n_j]\,\mathrm{d}S \\ &+ \int_{S_m} \delta\theta_i^*[m_i^{(\hat{n})} - \epsilon_{ijk}\mu_k n_j]\,\mathrm{d}S = 0.\end{aligned} \tag{63}$$

For arbitrary variations, each set of terms inside the square brackets must be zero. Thus, the Euler-Lagrange equations can be written:

$$(C_{ijkl}u_{k,l})_{,j} + \frac{1}{4}\epsilon_{pij}\epsilon_{pmn}\{D_{nk}(u_{k,ll} - u_{l,kl})\}_{,mj} + f_i = -\rho\omega^2 u_i \quad \text{in } V \tag{64}$$

$$\begin{aligned}t_i^{(\hat{n})} &= \sigma_{ji}n_j \quad \text{on } S_t \\ m_i^{(\hat{n})} &= \epsilon_{ijk}\mu_k n_j \quad \text{on } S_m\end{aligned} \tag{65}$$

Notice that (64) are the reduced wave equations from (55), while (65) represent the corresponding natural boundary conditions for C-CST. In the isotropic case, substituting (45) into (64) produces

$$c_1^2 u_{j,ji} - c_2^2\epsilon_{ijk}\epsilon_{kmn}(u_{n,mj} - l^2 u_{n,mjll}) + f_i = -\omega^2 u_i \quad \text{in } V \tag{66}$$

which is the equivalent of (56) in index notation.

Performing an inverse Fourier transform of individual terms in (57)-(60) back to the time domain, one finds

$$\mathcal{F}^{-1}[u^* v] = (u \star v)(t) \tag{67}$$

where the $\star$ operator denotes convolution over time, such that

$$(u \star v)(t) = \int_{-\infty}^{\infty} u(\tau)v(t+\tau)d\tau. \tag{68}$$

Consequently, we have established the following stationary *Principle of Correlated Action* for couple stress elastodynamics: Of all the possible displacement fields in V that satisfy the frequency domain kinematic boundary conditions on S_u and S_θ, the one that renders the action $\mathcal{A}[u;\omega]$ in (57) stationary corresponds to the solution of the reduced wave equations (64) and traction boundary conditions (65).

We should emphasize that this stationary Principle of Correlated Action also holds for classical theory, if one neglects contributions from mean curvature and moment tractions. Thus, the classical correlated

action for reduced elastodynamics can be written:

$$\begin{aligned}\mathcal{A}_{\mathrm{cl}}[u;\omega] = \frac{1}{2}\int_V e_{ij}^* C_{ijkl} e_{kl}\,\mathrm{d}V - \frac{\omega^2}{2}\int_V u_i^*\rho u_i\,\mathrm{d}V \\ - \int_V u_i^* f_i\,\mathrm{d}V - \int_{S_t} u_i^* t_i^{(\hat{n})}\,\mathrm{d}S\,.\end{aligned} \tag{69}$$

Response of Periodic Materials

This section summarizes the most relevant theoretical aspects for the numerical analysis of periodic materials. An in-depth treatment of the subject can be found in classical textbooks, such as Brillouin and Kittel, while a comprehensive review is provided by Hussein et al.. In our discussion we will use a generalized form of the reduced wave equation, however we will provide the Bloch-Floquet boundary conditions for the particular case of the C-CST model.

Bloch's theorem

Consider a reduced elastodynamic wave equation in the frequency domain of the form

$$\mathcal{L}\mathbf{u}(\mathbf{x}) = -\rho\omega^2\mathbf{u}(\mathbf{x}) \tag{70}$$

valid for a field $\mathbf{u}$ at a spatial point $\mathbf{x}$. Here $\mathcal{L}$ is a positive definite linear differential operator [Reddy, 1991, Kreyszig, 1978, Johnson, 2010], while ρ is the mass density and ω the corresponding angular frequency. Bloch's theorem [Brillouin, 1953] establishes that solutions to (70) are of the form

$$\mathbf{u}(\mathbf{x}) = \mathbf{w}(\mathbf{x})e^{i\mathbf{k}\cdot\mathbf{x}} \tag{71}$$

where $\mathbf{w}(\mathbf{x})$ is a Bloch function carrying with it the same periodicity as the material. Since the spatial period in $\mathbf{w}(\mathbf{x})$ is the lattice parameter $\mathbf{a}$, it follows that

$$\mathbf{w}(\mathbf{x}+\mathbf{a}) = \mathbf{w}(\mathbf{x}).$$

Accordingly, (71) is the product of a spatially periodic function $\mathbf{w}(\mathbf{x})$, with the periodicity of the lattice, and a plane wave (of wave vector $\mathbf{k}$), which is also periodic. As a result, field variables $\mathbf{\Phi}$ at opposite sides of the unit cell and separated by the lattice vector $\mathbf{a}$ are related through

$$\mathbf{\Phi}(\mathbf{x}+\mathbf{a}) = \mathbf{\Phi}(\mathbf{x})e^{i\mathbf{k}\cdot\mathbf{a}}. \tag{72}$$

In this case, $\mathbf{\Phi}$ refers to the principal variable involved in the physical problem, or to any of its spatial derivatives. From a physical point of view, (72) means that a field variable $\mathbf{\Phi}$ at points $\mathbf{x}$ and $\mathbf{x}+\mathbf{a}$ differ only by the phase shift $e^{i\mathbf{k}\cdot\mathbf{a}}$.

In the classical elastodynamic case in which $\mathcal{L}$ is the Navier operator of order 2, the generalized Boundary Value Problem (BVP) considering Bloch boundary conditions (BBCs) takes the form:

$$\mathcal{L}\mathbf{u}(\mathbf{x}) = -\rho\omega^2\mathbf{u}(\mathbf{x})\,, \tag{73a}$$

$$\mathbf{u}(\mathbf{x}+\mathbf{a}) = \mathbf{u}(\mathbf{x})e^{i\mathbf{k}\cdot\mathbf{a}}\,, \tag{73b}$$

$$\sigma(\mathbf{x}+\mathbf{a})\cdot\hat{\mathbf{n}} = -\sigma(\mathbf{x})\cdot\hat{\mathbf{n}}\,e^{i\mathbf{k}\cdot\mathbf{a}}\,, \tag{73c}$$

where $\mathbf{u}(\mathbf{x}+\mathbf{a})$ and $\mathbf{u}(\mathbf{x})$ give the field at $\mathbf{x}+\mathbf{a}$ and $\mathbf{x}$, respectively, and $\sigma(\mathbf{x})$ is the corresponding stress. Meanwhile, $\mathbf{a} = \mathbf{a}_1 n_1 + \mathbf{a}_2 n_2 + \mathbf{a}_3 n_3$ is the lattice translation vector and n_i are the lattice normal parameters.

Note that the BVP encompassed by (73) simultaneously describes the space-time periodicity of the solutions in the cellular material. Time periodicity is present in the frequency-domain nature of the reduced wave equation, while space periodicity explicitly appears in the wave number representation of the boundary conditions. The periodic relationship between opposite sides of the fundamental cell, appearing in the boundary terms, allows characterization of the fundamental properties of the material with the analysis of a single cell. At the same time the wave vector $\mathbf{k}$ in (73) simultaneously describes: (i) the propagation direction of a plane wave traveling through the unit cell and (ii) the spatial periodicity of the plane wave. In consequence, finding solutions to the Bloch-BVP amounts to finding those tuples $(\omega, \mathbf{k}, \mathbf{u})$ satisfying (73) when $\mathbf{k}$ is varied in the dual Fourier based representation of the fundamental material cell. This dual space corresponds to the *reciprocal space* and since it carries with it the periodic character of the physical space it suffices to consider values (and directions) of $\mathbf{k}$ within this reciprocal space representation of the unit cell.

In the case of the C-CST medium, Bloch's theorem states that the eigenfunctions of (19) can be expressed in the form

$$\mathbf{u}(\mathbf{x}) = \mathbf{u}(\mathbf{x}+\mathbf{a})e^{i\mathbf{k}\cdot\mathbf{a}}$$

where $\mathbf{a}$ is a vector that represents the periodicity of the material. That is, the solution is the same at opposite sides of the unit cell, except for a phase shift factor $e^{i\mathbf{k}\cdot\mathbf{a}}$. Due to the linearity of the differential equations we also have Bloch-periodic boundary conditions for the corresponding rotation and traction vectors. Thus, in the case of the C-CST elastic solid, Bloch's theorem reduces to the following set of boundary conditions for displacements, rotations, force-tractions and couple-tractions in index notation:

$$u_i(\mathbf{x}) = u_i(\mathbf{x}+\mathbf{a})e^{i\mathbf{k}\cdot\mathbf{a}}\,, \tag{74a}$$

$$\theta_i(\mathbf{x}) = \theta_i(\mathbf{x}+\mathbf{a})e^{i\mathbf{k}\cdot\mathbf{a}}\,, \tag{74b}$$

$$t_i(\mathbf{x}) = -t_i(\mathbf{x}+\mathbf{a})e^{i\mathbf{k}\cdot\mathbf{a}}\,, \tag{74c}$$

$$m_i(\mathbf{x}) = -m_i(\mathbf{x}+\mathbf{a})e^{i\mathbf{k}\cdot\mathbf{a}}\,. \tag{74d}$$

The set of conditions summarized in (74) will be satisfied in a variational sense using a finite element formulation, where the first two are essential boundary conditions and the other two natural boundary conditions. Subsequently, a numerical model of the unit cell resulting in a generalized eigenvalue problem will be solved for various specifications of the wave vector.

Hermiticity

Our finite element algorithm follows from the action functional formulated in (57). As discussed previously this amounts to the solution of the weak form of the frequency domain reduced wave equations subject to Bloch-periodic boundary conditions, as given by (23). Neglecting body forces in (57), we have:

$$\begin{aligned}\mathcal{A}[u;\omega] =& \frac{1}{2}\int_V e_{ij}^* C_{ijkl} e_{ij}\,\mathrm{d}V + \frac{1}{2}\int_V \kappa_i^* D_{ij}\kappa_i\,\mathrm{d}V - \frac{\omega^2}{2}\int_V u_i^*\rho u_i\,\mathrm{d}V \\ &- \int_{S_t} u_i^* t_i\,\mathrm{d}S - \int_{S_m}\theta_i^* m_i\,\mathrm{d}S\ ,\end{aligned} \tag{75}$$

To obtain real eigenvalues that correspond to propagating waves in the band structure of the material, the matrices resulting from the finite element discretization must be Hermitian. Equivalently, we must prove Hermiticity (self-adjointness) in the action functional. This amounts to showing that the boundary terms in (75) vanish under Bloch periodic boundary conditions.

Substitution of (23) into surface integral terms of (75) yields

$$\begin{aligned}&\int_S u_i^*(\mathbf{x})t_i(\mathbf{x})\,\mathrm{d}S + \int_S \theta_i^*(\mathbf{x})m_i(\mathbf{x})\,\mathrm{d}S = \\ &\sum_q \left\{ \int_{S_q} \left[u_i^*(\mathbf{x})t_i(\mathbf{x}) + u_i^*(\mathbf{x}+\mathbf{a}_q)t_i(\mathbf{x}+\mathbf{a}_q)\right]\mathrm{d}S_q + \right. \\ &\left. \int_{S_q}\left[\theta_i^*(\mathbf{x})m_i(\mathbf{x}) + \theta_i^*(\mathbf{x}+\mathbf{a}_q)m_i(\mathbf{x}+\mathbf{a}_q)\right]\mathrm{d}S_q \right\}\ ,\end{aligned} \tag{76}$$

with the index q referring to each pair of opposite sides of the boundary. Introducing the phase shifts and pulling out the common factors

give:

$$\begin{aligned}
&\int_S u_i^*(\mathbf{x}) t_i(\mathbf{x})\,\mathrm{d}S + \int_S \theta_i^*(\mathbf{x}) m_i(\mathbf{x})\,\mathrm{d}S = \\
&\sum_q \left\{ \int_{S_q} u_i^*(\mathbf{x}) \left[t_i(\mathbf{x}) + e^{i\mathbf{k}\cdot\mathbf{a}} t_i(\mathbf{x}+\mathbf{a}_q) \right] \mathrm{d}S_q + \right. \\
&\left. \int_{S_q} \theta_i^*(\mathbf{x}) \left[m_i(\mathbf{x}) + e^{i\mathbf{k}\cdot\mathbf{a}} m_i(\mathbf{x}+\mathbf{a}_q) \right] \mathrm{d}S_q \right\},
\end{aligned} \tag{77}$$

which after substituting (74c) and (74d) leads to the vanishing of the boundary terms, thus proving the Hermiticity condition.

Positive definiteness

Similarly, the proof for positive (semi)-definiteness reduces to showing that the action functionals are related in such a way that:

$$\omega^2 = \frac{\mathcal{U}[u;\omega]}{\tilde{\mathcal{T}}[u;\omega]} \geq 0\,, \tag{78}$$

where

$$\mathcal{U}[u;\omega] = \frac{1}{2}\int_V e_{ij}^* C_{ijkl} e_{kl}\,\mathrm{d}V + \frac{1}{2}\int_V \kappa_i^* D_{ij} \kappa_j\,\mathrm{d}V$$

and

$$\tilde{\mathcal{T}}[u;\omega] = \frac{1}{2}\int_V u_i^* \rho u_i\,\mathrm{d}V\,,$$

with the latter deriving directly from $\mathcal{T}[u;\omega]$.

Note that we have used the general representation C_{ijkl} and D_{ij} for the constitutive tensors. The functional $\mathcal{U}[u;\omega]$ is positive as long as these constitutive tensors are positive definite, which holds true if they satisfy

$$\begin{aligned}
C_{ijkl} e_{ij} e_{kl} &\geq 0 \quad \forall\, e_{mn}\,, \\
D_{ij} \kappa_i \kappa_j &\geq 0 \quad \forall\, \kappa_m\,.
\end{aligned}$$

For isotropic materials, this implies the following constraints for the material parameters:

$$\mu > 0\,, \quad 3\lambda + 2\mu > 0\,, \quad \eta > 0\,.$$

On the other hand, the condition $u_i \neq 0$, requires $\tilde{\mathcal{T}}$ to be different from zero and thus the condition required by (78). In the case of rigid body motion, $\mathcal{U}$ could be zero implying that the form is positive semi-definite, while the form $\tilde{\mathcal{T}}$ is positive definite.

Finite element formulation

In this section, we derive a consistent finite element formulation for periodic couple stress elastodynamics, as an extension of those formulated by [7] for the corresponding quasistatic problem and by [8] for periodic micropolar Bloch analysis. In particular, the C^1 displacement continuity requirement is avoided by using a Lagrange multiplier approach. Other finite element solutions in C-CST include a penalty method for isotropic elastostatics [Chakravarty et al., 2017], Lagrange multipliers for centrosymmetric anisotropic elastostatics [Pedgaonkar et al., 2021] and mixed variable methods for isotropic elastodynamics [Deng and Dargush, 2016, 2017].

[7] Bradley T. Darrall, Gary F. Dargush, and Ali R. Hadjesfandiari. Finite element lagrange multiplier formulation for size-dependent skew-symmetric couple-stress planar elasticity. *Acta Mechanica*, 225(1):195–212, 2014

[8] Nicolás Guarín-Zapata, Juan Gomez, Camilo Valencia, Gary F. Dargush, and Ali Reza Hadjesfandiari. Finite element modeling of micropolar-based phononic crystals. *Wave Motion*, 92: 102406, January 2020. ISSN 01652125. DOI: 10.1016/j.wavemoti.2019.102406. URL https://linkinghub.elsevier.com/retrieve/pii/S0165212519300526

Lagrange multiplier reformulation

Consider now a modification of the action given in (75) to include Lagrange multipliers λ_i that enforce compatibility between the displacement field u_i and an assumed independent rotation field θ_i. Thus, the modified action becomes

$$\begin{aligned}\hat{\mathcal{A}}[u;\omega] =& \frac{1}{2}\int_V e_{ij}^* C_{ijkl} e_{ij}\,\mathrm{d}V + \frac{1}{2}\int_V \kappa_i^* D_{ij}\kappa_i\,\mathrm{d}V - \frac{\omega^2}{2}\int_V u_i^*\rho u_i\,\mathrm{d}V \\ &- \int_{S_t} u_i^* t_i\,\mathrm{d}S - \int_{S_m}\theta_i^* m_i\,\mathrm{d}S \\ &+ \int_V \lambda_i^*(\epsilon_{ijk}u_{k,j} - 2\theta_i)\,\mathrm{d}V\ .\end{aligned} \tag{79}$$

For stationarity, we require

$$\delta\hat{\mathcal{A}} = \frac{\partial\hat{\mathcal{A}}}{\partial u_i}\,\delta u_i + \frac{\partial\hat{\mathcal{A}}}{\partial\theta_i}\,\delta\theta_i + \frac{\partial\hat{\mathcal{A}}}{\partial\lambda_i}\,\delta\lambda_i = 0\,,$$

which is equivalent to

$$\begin{aligned}&\int_V \delta e_{ij}^* C_{ijkl} e_{ij}\,\mathrm{d}V + \int_V \delta\kappa_i^* D_{ij}\kappa_i\,\mathrm{d}V - \omega^2\int_V \delta u_i^*\rho u_i\,\mathrm{d}V \\ &\quad - \int_{S_t}\delta u_i^* t_i\,\mathrm{d}S - \int_{S_m}\delta\theta_i^* m_i\,\mathrm{d}S \\ &\quad + \int_V \delta\lambda_i^*(\epsilon_{ijk}u_{k,j} - 2\theta_i)\,\mathrm{d}V \\ &\quad + \int_V (\epsilon_{ijk}\delta u_{k,j}^* - 2\delta\theta_i^*)\lambda_i\,\mathrm{d}V\ .\end{aligned} \tag{80}$$

Equation (80) is the modified weak form that will be used here as the basis for the finite element Bloch analysis of an elastic couple stress solid. The Lagrange multiplier terms enforce the required

kinematic constraint between the continuum rotations $\epsilon_{ijk}u_{k,j}$ of the material point and the independent rotational variables θ_i.

From (80), we obtain the following Euler-Lagrange equations

$$\begin{aligned}
&(C_{ijkl}e_{kl} + \epsilon_{ijk}\lambda_k)_{,j} = -\rho\omega^2 u_i \quad \text{in } V,\\
&\epsilon_{ijk}(D_{kl}\kappa_l)_{,j} - 2\lambda_i = 0 \quad \text{in } V,\\
&\theta_i = \frac{1}{2}\epsilon_{ijk}u_{k,j} \quad \text{in } V,\\
&t_i = (C_{ijkl}e_{kl} + \epsilon_{ijk}\lambda_k)n_j \quad \text{on } S_t,\\
&m_i = \epsilon_{ijk}D_{kl}\kappa_l n_j \quad \text{on } S_m\,,
\end{aligned} \tag{81}$$

Comparing this with (40), we can conclude that the Lagrange multipliers equal the skew-symmetric part of the force-stress tensor, i.e.,

$$\lambda_i = s_i\,.$$

Discretization

To discretize (80), we use for the element-based shape functions second-order Lagrange interpolation for the displacements and rotations and constant skew-symmetric stresses. This translates into C^0 inter-element displacement and rotation continuity, and skew-symmetric stresses that are constant within the element but discontinuous between elements. Figure 28 depicts a typical element for the discretization and the degrees of freedom used in two-dimensional idealizations.

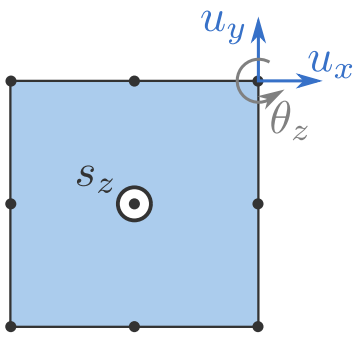

Figure 28: Finite element used for the finite element discretization of the C-CST material model. A second-order Lagrange interpolation is used for displacements and rotations while a constant is used for the skew-symmetric stresses. The nodal degrees of freedom are depicted as black disks while the white disk describes the element skew-symmetric force-stress degree of freedom.

To write the discretized equations, we will use a combined index notation. In this context subscripts will still make reference to scalar components of tensors while capital superscripts will indicate interpolation operations. For instance in the expression

$$u_i = {}_u N_i^Q u^Q$$

subscripts i indicate the scalar components of the vector u. To facilitate further operations this subscript is also placed in the shape function resulting in terms like ${}_u N_i^Q$ and where the term u^Q represents

the nodal point displacement associated to the Qth nodal point. This nodal vector implicitly considers horizontal and vertical rectangular components. To clarify, the displacement interpolation scheme written here as $u_i = {}_u N_i^Q u^Q$ takes the following explicit form for the single nodal point Q:

$$\begin{bmatrix} u_x \\ u_y \end{bmatrix} = \begin{bmatrix} \cdots & N^Q & 0 & \cdots \\ & 0 & N^Q & \end{bmatrix} \begin{Bmatrix} \vdots \\ u_x^Q \\ u_y^Q \\ \vdots \end{Bmatrix} . \tag{82}$$

With this notation we write for the primary variables (u_i, θ_i, s_i) the following interpolated versions

$$u_i = {}_u N_i^Q u^Q, \quad \theta_i = {}_\theta N_i^Q \theta^Q, \quad s_i = {}_s N_i^Q s^Q , \tag{83}$$

and similarly for the secondary kinematic descriptors $e_{ij}, \epsilon_{ijk} u_{i,j}$ and κ_i

$$e_{ij} = {}_e B_{ij}^Q u^Q, \quad \epsilon_{ijk} u_{i,j} = {}_\nabla B_k^Q u^Q, \quad \kappa_i = {}_\kappa B_i^Q \theta^Q , \tag{84}$$

together with the constitutive equations

$$\begin{aligned} \sigma_{ij} &= C_{ijkl} e_{kl} , \\ \mu_i &= D_{ij} \kappa_j . \end{aligned} \tag{85}$$

Substitution of the above relations in (80) gives the discrete version of the first variation of the modified correlated action;

$$\begin{aligned} \delta\hat{\mathcal{A}} = {} & \delta u^{Q*} \int_V ({}_e B_{ij}^Q)(C_{ijkl})({}_e B_{kl}^P)\, \mathrm{d}V\, u^P - \rho\omega^2 \delta u^{Q*} \int_V ({}_u N_i^Q)({}_u N_i^P)\, \mathrm{d}V\, u^P \\ & - \delta u^{Q*} \int_V {}_u N_i^Q f_i\, \mathrm{d}V - \delta u^{Q*} \int_S {}_u N_i^Q t_i\, \mathrm{d}S + \delta\theta^{Q*} \int_V ({}_\kappa B_i^Q)(D_{ij})({}_\kappa B_j^P)\, \mathrm{d}V\, \theta^P \\ & - \delta\theta^{Q*} \int_S {}_\theta N_i^Q m_i\, \mathrm{d}S + \delta s^{Q*} \int_V ({}_s N_k^Q)({}_\nabla B_k^P)\, \mathrm{d}V\, u^P + \delta u^{Q*} \int_V ({}_\nabla B_k^Q)({}_s N_k^P)\, \mathrm{d}V\, s^P \\ & - \delta s^{Q*} \int_V 2({}_s N_k^Q)({}_\theta N_k^P)\, \mathrm{d}V\, \theta^P - \delta\theta^{Q*} \int_V 2({}_\theta N_k^Q)({}_s N_k^P)\, \mathrm{d}V\, s^P = 0 . \end{aligned} \tag{86}$$

The explicit form of the interpolators defined above is given in the appendix.

Discrete equilibrium equations

From the arbitrariness in the variations δu^Q , $\delta\theta^Q$ and δs^Q in (86) it follows that:

$$\int_V ({}_eB^Q_{ij})(C_{ijkl})({}_eB^P_{kl})\,\mathrm{d}V\,u^P - \int_V ({}_uN^Q_i)({}_uN^P_i)\,\mathrm{d}V\,u^P - \int_V {}_uN^Q_i f_i\,\mathrm{d}V - \int_S {}_uN^Q_i t_i\,\mathrm{d}S = 0\,,$$
$$\int_V ({}_\kappa B^Q_i)(D_{ij})({}_\kappa B^P_j)\,\mathrm{d}V\,\theta^P - \int_S {}_\theta N^Q_i m_i\,\mathrm{d}S - \int_V 2({}_\theta N^Q_k)({}_sN^P_k)\,\mathrm{d}V\,s^P = 0\,,$$
$$\int_V ({}_sN^Q_k)(\nabla B^P_k)\,\mathrm{d}V\,u^P - \int_V 2({}_sN^Q_k)({}_\theta N^P_k)\,\mathrm{d}V\,\theta^P = 0\,,$$

which can be written in the standard finite element equilibrium form

$$\begin{bmatrix} K^{QP}_{uu} & 0 & K^{QP}_{us} \\ 0 & K^{QP}_{\theta\theta} & -K^{QP}_{\theta s} \\ K^{QP}_{su} & -K^{QP}_{s\theta} & 0 \end{bmatrix} \begin{Bmatrix} u^P \\ \theta^P \\ s^P \end{Bmatrix} = \omega^2 \begin{bmatrix} M^{QP}_{uu} & 0 & 0 \\ 0 & 0 & 0 \\ 0 & 0 & 0 \end{bmatrix} \begin{Bmatrix} u^P \\ \theta^P \\ s^P \end{Bmatrix} + \begin{Bmatrix} F^Q_u \\ m^Q_\theta \\ 0 \end{Bmatrix} \tag{87}$$

where the individual terms are defined as

$$K^{QP}_{uu} = \int_V ({}_eB^Q_{ij})(C_{ijkl})({}_eB^P_{kl})\,\mathrm{d}V\,, \quad M^{QP}_{uu} = \rho\omega^2 \int_V ({}_uN^Q_i)({}_uN^p_i)\,\mathrm{d}V\,,$$
$$K^{QP}_{us} = \int_V (\nabla B^Q_k)({}_sN^P_k)\,\mathrm{d}V\,, \qquad F^Q_u = \int_V {}_uN^Q_i f_i\,\mathrm{d}V + \int_S {}_uN^Q_i t_i\,\mathrm{d}S\,,$$
$$K^{QP}_{\theta\theta} = \int_V ({}_\kappa B^Q_i)(D_{ij})({}_\kappa B^P_j)\,\mathrm{d}V\,, \quad K^{QP}_{\theta s} = \int_V 2({}_\theta N^Q_k)({}_sN^P_k)\,\mathrm{d}V\,,$$
$$m^Q_\theta = \int_S {}_\theta N^Q_i m_i\,\mathrm{d}S\,, \qquad K^{QP}_{su} = \int_V ({}_sN^Q_k)(\nabla B^P_k)\,\mathrm{d}V\,,$$
$$K^{QP}_{s\theta} = \int_V 2({}_sN^Q_k)({}_\theta N^P_k)\,\mathrm{d}V\,.$$

Equation (87) can be rewritten in the following set of equilibrium equations in terms of nodal forces and couples

$$\begin{aligned} f^Q_{(\sigma)} + f^Q_s - f^Q_I - T^Q = 0\,, \\ m^Q_\mu + m^Q_s - q^Q = 0\,, \\ s(\theta - \hat{\theta}) = 0\,, \end{aligned} \tag{88}$$

where the subindex (σ) refers to the symmetric part of the stress tensor, and I to inertial forces. We also have a third equation reflecting the kinematic restriction, between the rotation θ and the introduced degree of freedom $\hat{\theta}$, imposed via the Lagrange-multiplier term s in each element.

When using a Lagrange multiplier formulation as in (80) the equations are still self-adjoint, as can be seen in the structure of (87). Nev-

ertheless, the stiffness matrix is indefinite and the solution of the problem represents a saddle-point instead of a minimum [Arnold, 1990, Darrall et al., 2014].

Eigenvalue problem

In finding the dispersion relations, we are interested in the free wave motion in the media. This leads to the following eigenvalue problem

$$[K]\{U\} = \omega^2[M]\{U\} \tag{89}$$

with

$$[K] = \begin{bmatrix} K_{uu}^{QP} & 0 & K_{us}^{QP} \\ 0 & K_{\theta\theta}^{QP} & -K_{\theta s}^{QP} \\ K_{su}^{QP} & -K_{s\theta}^{QP} & 0 \end{bmatrix}, \quad [M] = \begin{bmatrix} M_{uu}^{QP} & 0 & 0 \\ 0 & 0 & 0 \\ 0 & 0 & 0 \end{bmatrix}, \quad \{U\} = \begin{Bmatrix} u^P \\ \theta^P \\ s^P \end{Bmatrix}.$$

In (89) Bloch-periodic boundary conditions are yet to be imposed. This can be done in two ways [Valencia et al., 2019a]: (i) modifying the connectivity of the elements; and (ii) assembling the matrices without considering boundary conditions and impose the Bloch-periodicity through row/column operations. In this work, we follow the second approach as it requires the stiffness and mass matrices to be assembled once and the transformation matrices are computed for every wavenumber in the first Brillouin zone. This process results in the following eigenvalue problem

$$[K_R(\mathbf{k})]\{U\} = \omega^2[M_R(\mathbf{k})]\{U\} \tag{90}$$

with

$$[K_R(\mathbf{k})] = [T(\mathbf{k})^H K T(\mathbf{k})], \quad [M_R(\mathbf{k})] = [T(\mathbf{k})^H M T(\mathbf{k})],$$

where $[T(\mathbf{k})]$ represents the transformation matrix for a given $\mathbf{k}$, and the $[T^H]$ refers to the Hermitian transpose of $[T]$. For an explicit form for the matrices $[T]$ refer to Hussein et al. or Guarín-Zapata.

We conducted the implementation on top of the in-house finite element code SolidsPy [Guarín-Zapata and Gómez, 2020] and used SciPy to solve the eigenvalue problem [Virtanen et al., 2020]. To take advantage of the sparsity of the matrices the problem should be written as matrix-vector multiplications, such as

$$\begin{aligned} \{x\} &= [T]\{U\}, \\ \{y\} &= [K]\{x\}, \\ \{z\} &= [T^H]\{y\}, \end{aligned}$$

with $\{z\}$ representing the image of the linear operator $[K_R]$ over $\{U\}$. The same procedure can be applied for the right-hand side of (90).

The Lagrange-multiplier approach leads to the structure of the mass and stiffness matrix in (89). In our implementation we tried first to solve the generalized-eigenvalue problem using the Arnoldi method [Lehoucq et al., 1998] however we obtained negative results. On the other hand, an implementation of the LOBPCG method [Knyazev, 2001], which takes advantage of the sparse structure of the problem yields appropriate solutions.

Results: Dispersion relations for C-CST cellular materials

In this section we conduct a series of dispersion analyses intended to show the effectiveness of our mixed finite element implementation of the C-CST material model in predicting the correct wave propagation properties of the material. All the dispersion graphs use the dimensionless frequency

$$\Omega = \frac{2d\omega}{c_2}\,, \tag{91}$$

for the vertical axis, where $2d$ is the dimension of the unit cell and $c_2^2 = \mu/\rho$ is the speed of the shear wave for a classical elastic material.

As a first instance we find the response of a homogeneous periodic material which has also a closed form solution. We will then continue to study a second classical example corresponding to a homogeneous material with a circular pore. These two problems exhibit two different levels of dispersive behavior. In the homogeneous material cell, dispersion is due to the kinematic enrichment of the model associated to the length scale parameter, while in the porous material model additional dispersion arises due to the explicit microstructural feature.

Homogeneous material

As a test of accuracy and effectiveness of our implementation we consider the case of a homogeneous material cell with the same mechanical properties of the material reported previously and with closed form dispersion relations reported in (52). In this simple model microstructural effects are introduced through the material length parameter. Recall that this parameter is defined by the ratio $\frac{\eta}{\mu}$ where η is the curvature-couple stress module while μ is the shear modulus from Cauchy elasticity. The results in terms of the resulting band structure are shown in fig. 29. For a conceptual description of the reciprocal space and a guide on how to interpret the results in a Bloch analysis the reader is referred to [9]. Note that this set of results is directly comparable with the curves from the closed form solutions from fig. 26. Since the material is isotropic there are no directional effects and, as discussed previously, the only difference between this model and the

[9] Camilo Valencia. *Wave propagation in 2D elastic periodic materials: theoretical and computational analysis*. PhD thesis, Universidad EAFIT, 2019

result from classical elasticity is the dispersive behavior of the shear wave. In contrast with the micropolar model [Guarín-Zapata et al., 2020], the present C-CST model does not exhibit additional rotational waves.

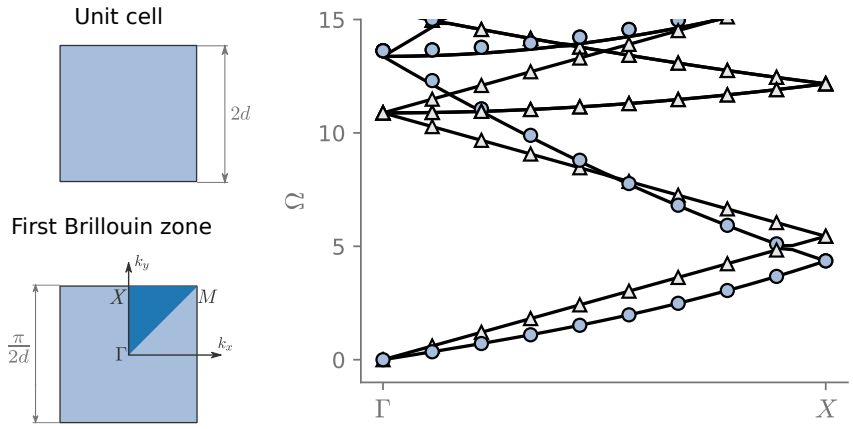

Figure 29: Dispersion relations for a homogeneous material model. Solid lines represent FEM results while markers correspond to the analytic solution. Triangular and filled-dots describe the P and SV wave modes, respectively.

Figure 30 shows the results for the same material cell but now we have considered 4 different values of the length scale parameter corresponding to $\ell \in [0.01, 0.1, 1, 10]$. Notice that, as expected, the increasing value of this parameter only affects the dispersive response of the shear waves while the P-waves retain their classical non-dispersive behavior. As seen in (53) the dispersion increases for higher values of ℓ due to the factor $\sqrt{1 + k^2\ell^2}$ in the dispersion relation, making the shear wave speed increase when the wavenumber increases. This behavior is closely followed by the numerical results presented in fig. 30.

As an additional verification, we also tested the convergence in the calculation of the dispersion relations after considering the first 8 modes for a sequence of meshes of 1×1, 2×2, 4×4, and 8×8 elements. The error in the eigenvalue computation was measured according to

$$e = \frac{\|\boldsymbol{\omega}_{\text{ref}} - \boldsymbol{\omega}_h\|_2}{\|\boldsymbol{\omega}_{\text{ref}}\|_2},$$

where $\boldsymbol{\omega}_h$ is the set of eigenvalues (dispersion relation) for a mesh of characteristic element size h and $\boldsymbol{\omega}_{\text{ref}}$ is the solution corresponding to the finer 16×16 elements mesh, which has been taken as reference. The results for this sequence, together with the variation in the error parameter, are displayed in fig. 31. The estimated convergence rate for the eigenvalues is 2.32.

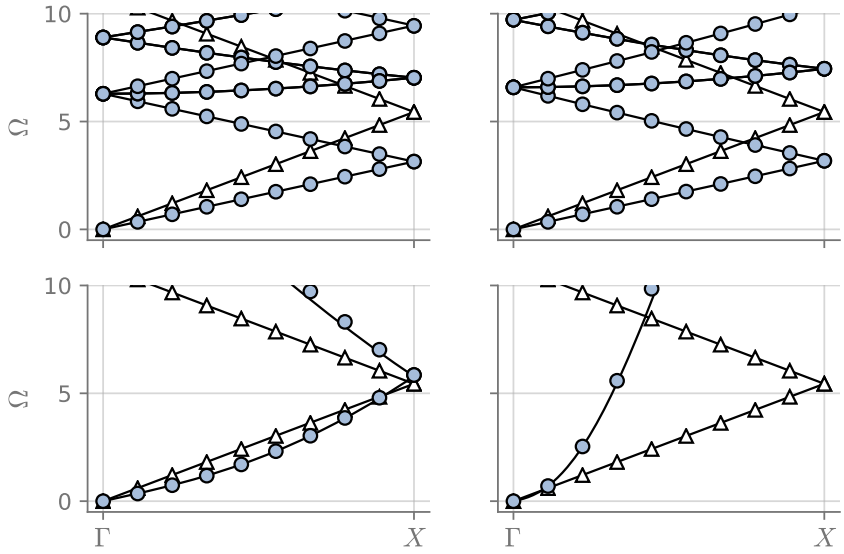

Figure 30: Dispersion relations for a homogeneous material model with varying length scales, $\ell \in [0.01, 0.1, 1, 10]$. Solid lines represent FEM results while markers correspond to analytic solutions. As expected, for increasing ℓ the S-wave presents more dispersion due to the factor $\sqrt{1 + k^2\ell^2}$, as presented in (53).

Dispersion in cellular material with a circular pore

Now, we consider a C-CST composite material cell configured by a circular pore embedded in a homogeneous matrix. The presence of the pore provides the model with a second length-scale due to the microstructure, in addition to the one introduced by the material length-scale parameter ℓ. The resulting band structure for cells with 4 different length parameters are shown in fig. 32. In contrast to the results from the fully homogeneous material cell, this composite model exhibits partial bandgaps along the directions ΓM and $X\Gamma$. The presence of the circular pore introduces scattering effects inside each cell. However as revealed by results based on classical elasticity models for this same material cell, the bandgaps are now the result of the increased dispersive behavior due to the length scale parameter. Figure 32 presents dispersion curves for a cellular material with circular pores for varying length scales, $\ell/a = [0.01, 0.1, 1, 10]$

Conclusions

We have developed a new frequency domain correlated action principle for the consistent couple stress theory (C-CST) of Hadjesfandiari and Dargush and used that to extend the Lagrange multiplier finite element algorithm of Darrall et al. to study periodic cellular materials through Floquet-Bloch theory from solid state physics. Particularly, we have addressed the imposition of Bloch boundary conditions for this material model and within the specific context of the Lagrange

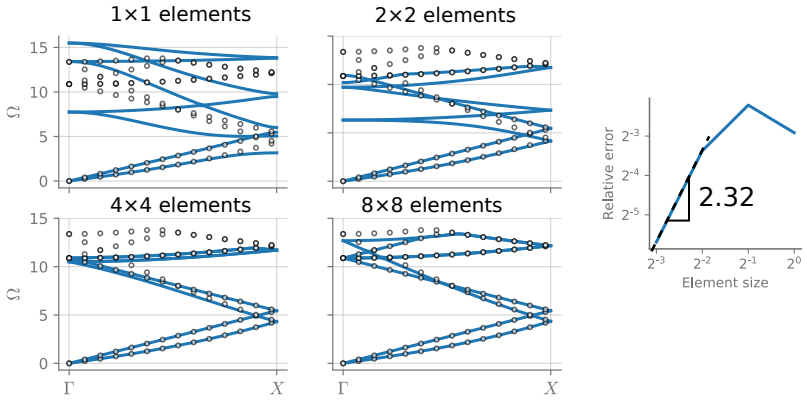

Figure 31: Convergence of the first 12 modes in the dispersion relations for a sequence of meshes with: 1×1, 2×2, 4×4, and 8×8 elements — presented as solid blue lines in the background. The results are compared with a mesh that has 16×16 elements — presented as dots in the foreground. The estimated convergence rate for the eigenvalues in the 2-norm is 2.32.

multiplier finite element implementation, where in addition to force tractions and displacements there are also couple tractions and rotations. We also discussed numerical aspects related to the solution of the wavenumber dependent generalized eigenvalue problem resulting from the imposition of the Bloch periodic boundary conditions. The implementation was shown to give accurate results for homogeneous and porous unit cells and for varying couple stress material length-scale parameters. The analysis of the first cell was used mainly to test the correctness of our implementation as this material has a closed-form dispersion relation. The algorithm was shown to correctly capture the non-dispersive P-wave as well as the dispersive SV-wave. This analysis was complemented by a convergence analysis with four different meshes of increasing refinement for the material cell. The observed convergence rate shows that the Lagrange multiplier algorithm is effective in maintaining continuity by imposing the newly introduced kinematic constraint implicit in the mean curvature tensor definition. Interestingly, the second material cell, corresponding to a circular pore embedded in a homogeneous matrix, reveals the appearance of bandgaps introduced by the kinematic features of C-CST defined in terms of the microstructural length scale parameter.

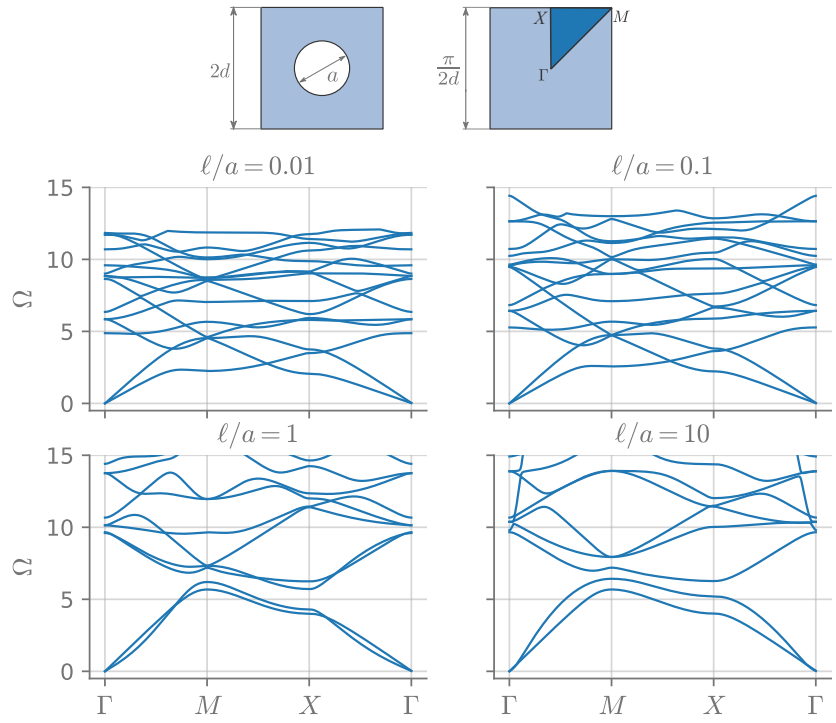

Figure 32: Dispersion for a cellular material with circular pores for varying length scales, $\ell/a = [0.01, 0.1, 1, 10]$.

Explicit form of the finite element interpolators in the C-CST solid

We have the following explicit forms for the interpolation matrices in two dimensions [Bathe, 1995]:

$$ {}_u\mathbf{N}^Q = {}_\theta\,\mathbf{N}^Q = {}_s\mathbf{N}^Q = \begin{bmatrix} \cdots & N^Q & 0 & \cdots \\ \cdots & 0 & N^Q & \cdots \end{bmatrix}, \qquad {}_e\mathbf{B} = \begin{bmatrix} \cdots & \frac{\partial N^Q}{\partial x} & 0 & \cdots \\ \cdots & 0 & \frac{\partial N^Q}{\partial x} & \cdots \\ \cdots & \frac{\partial N^Q}{\partial y} & \frac{\partial N^Q}{\partial x} & \cdots \end{bmatrix}, $$

$$ {}_\kappa\mathbf{B} = \begin{bmatrix} \cdots & -\frac{\partial N^Q}{\partial y} & \cdots \\ \cdots & \frac{\partial N^Q}{\partial x} & \cdots \end{bmatrix}, \qquad \nabla\mathbf{B} = \begin{bmatrix} \cdots & -\frac{\partial N^Q}{\partial y} & \frac{\partial N^Q}{\partial x} & \cdots \end{bmatrix}. $$

In the case of isotropic materials under plane strain idealizations, we have the following constitutive tensor in Voigt notation

$$ \mathbf{C} = \frac{E(1-\nu)}{(1+\nu)(1-2\nu)} \begin{bmatrix} 1 & \frac{\nu}{1-\nu} & 0 \\ \frac{\nu}{1-\nu} & 1 & 0 \\ 0 & 0 & \frac{1-2\nu}{2(1-\nu)} \end{bmatrix}, \qquad \mathbf{D} = 4\eta \begin{bmatrix} 1 & 0 \\ 0 & 1 \end{bmatrix}. $$

Future work

This chapter present some possible lines for future work related to the topics of this document. Specifically:

- the formulation of finite element methods in the time domain; and
- extension to three dimensions.

Time domain formulation

From a wave propagation perspective, a time domain formulation for elastodynamics is essential since wave phenomena are naturally presented as time varying. Furthermore, in the context of metamaterials and phononic crystals it is of interest since it allows the use direct numerical simulations to study the bulk properties (see Hussein et al., Joannopoulos et al., for example).

The equation of equilibrium for an elastic solid after a finite element dicretization reads[10]

$$[M]\{\ddot{U}\} + [C]\{\dot{U}\} + [K]\{U\} = \{R\}\,,$$

where $[M]$, $[C]$, and $[K]$ are the mass, damping, and stiffness matrices; $\{R\}$ is the vector of externally applied loads; and $\{U\}$, $\{\dot{U}\}$, and $\{\ddot{U}\}$ are the generalized displacement, velocity, and acceleration vectors. The specific details for the matrices and vectors vary for the micropolar and consistent couple stress models. In the case of lossless media the equation can be further simplified to

$$[M]\{\ddot{U}\} + [K]\{U\} = \{R\}\,.$$

The most common solution approach is the direct integration method, where the time derivatives are approximated at some discrete times and the solution is achieved in an iterative fashion. In the case of micropolar elasticity the direct integration can be carried without any conceptual differences from classical elasticity.

On the other hand, if we want to use the Lagrange-multiplier finite element proposed before for couple stress elasticity we would end up

[10] Klaus-Jurgen Bathe. *Finite Element Procedures*. Prentice Hall, 2 edition, 6 1995

with a discrete system similar to the following one.

$$\begin{bmatrix} M_{uu} & 0 & 0 \\ 0 & 0 & 0 \\ 0 & 0 & 0 \end{bmatrix} \begin{Bmatrix} \ddot{u} \\ \ddot{\theta} \\ \ddot{s} \end{Bmatrix} + \begin{bmatrix} K_{uu} & 0 & K_{us} \\ 0 & K_{\theta\theta} & -K_{\theta s} \\ K_{su} & -K_{s\theta} & 0 \end{bmatrix} \begin{Bmatrix} u \\ \theta \\ s \end{Bmatrix} = \begin{Bmatrix} F_u \\ m_\theta \\ 0 \end{Bmatrix},$$

that cannot be treated in the same way since the full mass matrix is not invertible. We could rewrite this equation as the following system

$$\begin{aligned} &[M_{uu}]\{\ddot{u}\} + [K_{uu}]\{u\} + [K_{us}]\{s\} = \{F_u\}, \\ &[K_{\theta\theta}]\{\theta\} - [K_{\theta s}]\{s\} = \{m_\theta\}, \\ &[K_{su}]\{u\} + [K_{s\theta}]\{\theta\} = 0, \end{aligned}$$

where we could solve the third equation for θ, the second one for s, and, finally, the first one for u. All of these steps in an iterative process.

Extension to three dimensions

The results presented in this document were related to two-dimensional analysis. These analyses succeed to present the dispersive behavior of the periodic materials under generalized continua. Nevertheless, they neglect some effects that might be only possible in three dimensions, such as torsion. Hence, a prospective line of work is the extension of these models in three dimensions.

Micropolar case

As in the previous section, the micropolar case is straightforward. If we consider the following Voigt-like notation for the kinematic variables

$$e = (\gamma_{xx}, \gamma_{yy}, \gamma_{zz}, \gamma_{zy}, \gamma_{yz}, \gamma_{zx}, \gamma_{xz}, \gamma_{xy}, \gamma_{yx}, \kappa_{xx}, \kappa_{yy}, \kappa_{zz}, \kappa_{zy}, \kappa_{yz}, \kappa_{zx}, \kappa_{xz}, \kappa_{xy}, \kappa_{yx}),$$

we have the following stiffness tensor

$$[C] = \begin{bmatrix} C_1 & 0 & 0 & 0 & 0 & 0 & 0 & 0 \\ 0 & C_2 & 0 & 0 & 0 & 0 & 0 & 0 \\ 0 & 0 & C_2 & 0 & 0 & 0 & 0 & 0 \\ 0 & 0 & 0 & C_2 & 0 & 0 & 0 & 0 \\ 0 & 0 & 0 & 0 & C_3 & 0 & 0 & 0 \\ 0 & 0 & 0 & 0 & 0 & C_4 & 0 & 0 \\ 0 & 0 & 0 & 0 & 0 & 0 & C_4 & 0 \\ 0 & 0 & 0 & 0 & 0 & 0 & 0 & C_4 \end{bmatrix},$$

with

$$C_1 = \begin{bmatrix} \lambda+2\mu & \lambda & \lambda \\ \lambda & \lambda+2\mu & \lambda \\ \lambda & \lambda & \lambda+2\mu \end{bmatrix}, \quad C_2 = \begin{bmatrix} \mu+\alpha & \mu-\alpha \\ \mu-\alpha & \mu+\alpha \end{bmatrix},$$
$$C_3 = \begin{bmatrix} \beta+2\mu & \beta & \beta \\ \beta & \beta+2\mu & \beta \\ \beta & \beta & \beta+2\mu \end{bmatrix}, \quad C_4 = \begin{bmatrix} \gamma+\epsilon & \gamma-\epsilon \\ \gamma-\epsilon & \gamma+\epsilon \end{bmatrix}.$$

If we use Lagrange interpolators for displacements and rotations we get the following generalized displacement to strain matrix ($[B]$)

$$[B] = \begin{bmatrix} N_{i,x} & 0 & 0 & 0 & 0 & 0 \\ 0 & N_{i,y} & 0 & 0 & 0 & 0 \\ 0 & 0 & N_{i,z} & 0 & 0 & 0 \\ 0 & N_{i,z} & 0 & N_i & 0 & 0 \\ 0 & 0 & N_{i,y} & -N_i & 0 & 0 \\ N_{i,z} & 0 & 0 & 0 & -N_i & 0 \\ 0 & 0 & N_{i,x} & 0 & N_i & 0 \\ 0 & N_{i,x} & 0 & 0 & 0 & -N_i \\ N_{i,y} & 0 & 0 & 0 & 0 & N_i \\ 0 & 0 & 0 & N_{i,x} & 0 & 0 \\ 0 & 0 & 0 & 0 & N_{i,y} & 0 \\ 0 & 0 & 0 & 0 & 0 & N_{i,z} \\ 0 & 0 & 0 & 0 & N_{i,z} & 0 \\ 0 & 0 & 0 & 0 & 0 & N_{i,y} \\ 0 & 0 & 0 & N_{i,z} & 0 & 0 \\ 0 & 0 & 0 & 0 & 0 & N_{i,x} \\ 0 & 0 & 0 & 0 & N_{i,x} & 0 \\ 0 & 0 & 0 & N_{i,y} & 0 & 0 \end{bmatrix}$$

C-CST case

In the case of couple stress elasticity we have additional difficulties due to higher order derivatives, as mentioned before. In the present work we used a Lagrange-multiplier approach and this could work in three dimensions as well.

Kwon and Lee used an element with tri-quadratic interpolation for the displacement field, a tri-linear interpolation for the rotation field, (elementwise) constant Lagrange-multpliers, and an additional Lagrange-multiplier to enforce that the trace of the torsion tensor is zero. In the present case, the consistent couple stress theory we could use an additional Lagrange-multiplier to enforce that the trace of the curvature tensor is zero.

Concluding remarks

The present work dealt with wave propagation on periodic materials under generalized continuum models. We used two different generalized continuum models: micropolar and consistent couple stress elasticity. The former includes additional degrees of freedom at each material point, while in the latter the deformation energy depends on higher-order derivatives. We proposed variational statements for both of these models and developed finite element formulations to obtain dispersion relations. The final chapter of this document presents a novel method to study the directionality (or anisotropy) of periodic materials. This method can be used in a general framework such as electrodynamics or acoustics and not just in elastodynamics. Finally, as by-products of this work, we developed open-source Python packages for finite elements (SolidsPy [11]) and continuum mechanics (Continuum_Mechanics[12]), which are presented in the appendix of this document.

[11] Nicolás Guarín-Zapata and Juan Gómez. SolidsPy: 2D-Finite Element Analysis with Python, 2020. URL https://github.com/AppliedMechanics-EAFIT/SolidsPy

[12] Nicolás Guarín-Zapata. continuum_mechanics: Continuum Mechanics calculations in Python, 2020. URL https://github.com/nicoguaro/continuum_mechanics

Bibliography

E.L Aero and E.V Kuvshinski. Fundamental equations of theory of elastic media with rotationally interacting particles. *Soviet Physics Solid State*, 2:1272–1281, 1961.

K. Aki and P. Richards. *Quantitative Seismology*. University Science Books, second edition, 2002.

George B. Arfken, Hans J. Weber, and Frank Harris. *Mathematical Methods for Physicists*. Academic Press, 6 edition, 2005.

Douglas N. Arnold. Mixed finite element methods for elliptic problems. *Computer Methods in Applied Mechanics and Engineering*, 82 (1):281–300, September 1990. ISSN 0045-7825. DOI: 10.1016/0045-7825(90)90168-L. URL http://www.sciencedirect.com/science/article/pii/004578259090168L.

Bertram Alexander Auld. *Acoustic fields and waves in solids*, volume 1. Wiley New York, 1973.

Biswajit Banerjee. *An Introduction to Metamaterials and Waves in Composites*. CRC Press, 2011.

Klaus-Jurgen Bathe. *Finite Element Procedures*. Prentice Hall, 2 edition, 6 1995.

Felix Bloch. Über die quantenmechanik der elektronen in kristallgittern. *Zeitschrift für physik*, 52(7-8):555–600, 1929.

Leon Brillouin. *Wave propagation in periodic structures: Electric filters and crystal lattices*. Dover Publications, 1 edition, 1953.

Léon Brillouin. *Wave propagation in periodic structures: electric filters and crystal lattices*. Courier Dover Publications, 2003.

V. T. Buchwald. Elastic waves in anisotropic media. *Proceedings of the Royal Society of London. Series A. Mathematical and Physical Sciences*, 253(1275):563–580, 1959.

José M. Carcione. *Wave fields in real media: Wave propagation in anisotropic, anelastic, porous and electromagnetic media*. Elsevier, 2007.

F Casadei and JJ Rimoli. Anisotropy-induced broadband stress wave steering in periodic lattices. *International Journal of Solids and Structures*, 50(9):1402–1414, 2013.

Sourish Chakravarty, Ali R. Hadjesfandiari, and Gary F. Dargush. A penalty-based finite element framework for couple stress elasticity. *Finite Elements in Analysis and Design*, 130:65–79, 2017.

E. Cosserat and F. Cosserat. *Théorie des Corps Déformables.* A Hermann et Fils, 1909.

S. C. Cowin. Stress functions for Cosserat elasticity. *International Journal of Solids and Structures*, 6(4):389–398, 1970a.

Stephen C Cowin. An incorrect inequality in micropolar elasticity theory. *Zeitschrift für Angewandte Mathematik und Physik (ZAMP)*, 21(3): 494–497, 1970b.

Bradley T. Darrall, Gary F. Dargush, and Ali R. Hadjesfandiari. Finite element lagrange multiplier formulation for size-dependent skew-symmetric couple-stress planar elasticity. *Acta Mechanica*, 225(1):195–212, 2014.

Guoqiang Deng and Gary F. Dargush. Mixed Lagrangian formulation for size-dependent couple stress elastodynamic response. *Acta Mechanica*, 227(12):3451–3473, 2016.

Guoqiang Deng and Gary F. Dargush. Mixed lagrangian formulation for size-dependent couple stress elastodynamic and natural frequency analyses. *International Journal for Numerical Methods in Engineering*, 109(6):809–836, 2017.

Pierre A. Deymier. *Acoustic metamaterials and phononic crystals*, volume 173. Springer Science & Business Media, 2013.

A Cemal Eringen and ES Suhubi. Nonlinear theory of simple micro-elastic solids—i. *International Journal of Engineering Science*, 2(2):189–203, 1964.

A.C Eringen. Linear theory of micropolar elasticity. *Journal of Mathematics and Mechanics*, 15:909–923, 1966.

NA Fleck and JW Hutchinson. Strain gradient plasticity. *Advances in applied mechanics*, 33:296–361, 1997.

NA Fleck, GM Muller, MF Ashby, and JW Hutchinson. Strain gradient plasticity: theory and experiment. *Acta Metallurgica et Materialia*, 42 (2):475–487, 1994.

Gaston Floquet. Sur les équations différentielles linéaires à coefficients périodiques. In *Annales scientifiques de l'École normale supérieure*, volume 12, pages 47–88, 1883.

Tobias Frenzel, Muamer Kadic, and Martin Wegener. Three-dimensional mechanical metamaterials with a twist. *Science*, 358 (6366):1072–1074, 2017.

Benjamin M Goldsberry and Michael R Haberman. Negative stiffness honeycombs as tunable elastic metamaterials. *Journal of Applied Physics*, 123(9):091711, 2018.

Stefano Gonella and Massimo Ruzzene. Analysis of in-plane wave propagation in hexagonal and re-entrant lattices. *Journal of Sound and Vibration*, 312:125–139, 2008.

Nicolás Guarín-Zapata. Simulación Numérica de Problemas de Propagación de Ondas: Dominios Infinitos y Semi-infinitos. Master's thesis, Universidad EAFIT, 2012.

Nicolás Guarín-Zapata. continuum_mechanics: Continuum Mechanics calculations in Python, 2020. URL https://github.com/nicoguaro/continuum_mechanics.

Nicolás Guarín-Zapata and Juan Gomez. Evaluation of the spectral finite element method with the theory of phononic crystals. *Journal of Computational Acoustics*, 23(02):1550004, 2015.

Nicolás Guarín-Zapata and Juan Gómez. SolidsPy: 2D-Finite Element Analysis with Python, 2020. URL https://github.com/AppliedMechanics-EAFIT/SolidsPy.

Nicolás Guarín-Zapata, Juan Gómez, David Kisailus, and Pablo D. Zavattieri. Bandgap tuning in bioinspired helicoidal composites. *Journal of the Mechanics and Physics of Solids*, 131:344–357, October 2019. ISSN 00225096. DOI: 10.1016/j.jmps.2019.07.003. URL https://linkinghub.elsevier.com/retrieve/pii/S0022509619302431.

Nicolás Guarín-Zapata, Juan Gomez, Camilo Valencia, Gary F. Dargush, and Ali Reza Hadjesfandiari. Finite element modeling of micropolar-based phononic crystals. *Wave Motion*, 92:102406, January 2020. ISSN 01652125. DOI: 10.1016/j.wavemoti.2019.102406. URL https://linkinghub.elsevier.com/retrieve/pii/S0165212519300526.

Ali R Hadjesfandiari and Gary F Dargush. Couple stress theory for solids. *International Journal of Solids and Structures*, 48(18):2496–2510, 2011.

Ali R Hadjesfandiari, Arezoo Hajesfandiari, and Gary F Dargush. Skew-symmetric couple-stress fluid mechanics. *Acta Mechanica*, 226 (3):871–895, 2015.

Soroosh Hassanpour and G. R. Heppler. Step-by-step simplification of the micropolar elasticity theory to the couple-stress and classical elasticity theories. In *ASME 2014 International Mechanical Engineering Congress and Exposition*, pages V009T12A042–V009T12A042. American Society of Mechanical Engineers, 2014.

Soroosh Hassanpour and Glenn R Heppler. Micropolar elasticity theory: a survey of linear isotropic equations, representative notations, and experimental investigations. *Mathematics and Mechanics of Solids*, 22(2):224–242, 2017.

Mahmoud I. Hussein, Michael J. Leamy, and Massimo Ruzzene. Dynamics of phononic materials and structures: Historical origins, recent progress, and future outlook. *Applied Mechanics Reviews*, 66(4): 040802, 2014.

Sokratis N Iliopoulos, Dimitrios G Aggelis, and Demosthenes Polyzos. Wave dispersion in fresh and hardened concrete through the prism of gradient elasticity. *International Journal of Solids and Structures*, 78: 149–159, 2016.

Sokratis N Iliopoulos, Fabian Malm, Christian U Grosse, Dimitrios G Aggelis, and Demosthenes Polyzos. Concrete wave dispersion interpretation through Mindlin's strain gradient elastic theory. *The Journal of the Acoustical Society of America*, 142(1):EL89–EL94, 2017.

John Joannopoulos, Steven Johnson, Joshua Winn, and Robert Meade. *Photonic Crystals: Molding the Flow of Light*. Princeton University Press, 2 edition, 2008.

Steven G. Johnson. Notes on the algebraic structure of wave equations. Technical report, Massachusetts Institute of Technology, 2010.

Toufik Kanit, Franck N'Guyen, Samuel Forest, Dominique Jeulin, Matt Reed, and Scott Singleton. Apparent and effective physical properties of heterogeneous materials: Representativity of samples of two materials from food industry. *Computer Methods in Applied Mechanics and Engineering*, 195(33):3960–3982, 2006.

Charles Kittel. *Introduction to Solid State Physics*. Wiley, 7 edition, 1996.

Andrew V. Knyazev. Toward the optimal preconditioned eigensolver: Locally optimal block preconditioned conjugate gradient method. *SIAM journal on scientific computing*, 23(2):517–541, 2001.

W.T Koiter. Couple stresses in the theory of elasticity. *Proc.K.Ned.Akad.Wet(B)*, 67:17–44, 1964.

Erwin Kreyszig. *Introductory functional analysis with applications*, volume 1. wiley New York, 1978.

M. Kulesh. Waves in linear elastic media with microrotations, part 1: Isotropic full cosserat model. *Bulletin of the Seismological Society of America*, 99(2B):1416–1422, 2009.

Young-Rok Kwon and Byung-Chai Lee. A mixed element based on Lagrange multiplier method for modified couple stress theory. *Computational Mechanics*, 59(1):117–128, January 2017. ISSN 1432-0924. DOI: 10.1007/s00466-016-1338-3. URL https://doi.org/10.1007/s00466-016-1338-3.

Young-Rok Kwon and Byung-Chai Lee. Three dimensional elements with Lagrange multipliers for the modified couple stress theory. *Computational Mechanics*, 62(1):97–110, July 2018. ISSN 1432-0924. DOI: 10.1007/s00466-017-1487-z. URL https://doi.org/10.1007/s00466-017-1487-z.

R. Lakes. Experimental micro mechanics methods for conventional and negative Poisson's ratio cellular solids as Cosserat continua. *Journal of Engineering Materials and Technology*, 113(1):148–155, 1991.

Roderic Lakes. Elastic and viscoelastic behavior of chiral materials. *International Journal of Mechanical Sciences*, 43(7):1579–1589, 2001.

Philippe Langlet. *Analyse de la propagation des ondes acoustiques dans les matériaux périodiques à l'aide de la méthode des éléments finis*. PhD thesis, Valenciennes, 1993.

Hassel Ledbetter and Albert Migliori. A general elastic-anisotropy measure. *Journal of applied physics*, 100(6):063516, 2006.

Richard B. Lehoucq, Danny C. Sorensen, and Chao Yang. *ARPACK users' guide: solution of large-scale eigenvalue problems with implicitly restarted Arnoldi methods*, volume 6. Siam, 1998.

Angela Madeo. *Generalized Continuum Mechanics and Engineering Applications*. Elsevier, 2015.

G. Thomas Mase, Ronald E. Smelser, and George E. Mase. *Continuum mechanics for engineers*. CRC press, 2009.

Gérard A. Maugin. *Continuum mechanics through the twentieth century*, volume 10 of *Solid Mechanics and Its Applications*. Springer, 2013.

Florian Maurin, Claus Claeys, Elke Deckers, and Wim Desmet. Probability that a band-gap extremum is located on the irreducible Brillouin-zone contour for the 17 different plane crystallographic lattices. *International Journal of Solids and Structures*, 135: 26–36, 2018. DOI: 10.1016/j.ijsolstr.2017.11.006. URL https://www.sciencedirect.com/science/article/pii/S0020768317305103.

A. Merkel, Vincent Tournat, and V. Gusev. Experimental evidence of rotational elastic waves in granular phononic crystals. *Physical Review Letters*, 107(22):225502, 2011.

Jean-Claude Michel, Hervé Moulinec, and Pierre Suquet. Effective properties of composite materials with periodic microstructure: a computational approach. *Computer methods in applied mechanics and engineering*, 172(1-4):109–143, 1999.

G. Midya. On love-type surface waves in homogeneous micropolar elastic media. *International Journal of Engineering Science*, 42:1275–1288, 2004.

Graeme W. Milton and Andrej V. Cherkaev. Which elasticity tensors are realizable? *Journal of Engineeering Materials and Technology*, 1995.

Graeme W Milton and John R Willis. On modifications of newton's second law and linear continuum elastodynamics. *Proceedings of the Royal Society A: Mathematical, Physical and Engineering Science*, 463 (2079):855–880, 2007.

R. Mindlin. Micro-structure in linear elasticity. *Archives of Rational Mechanics and Analysis*, 16:51–78, 1964.

R. Mindlin. Second gradient of strain and surface tension in linear elasticity. *International Journal of Solids and Structures*, 1:417–438, 1965.

R. Mindlin and N.N Eshel. On first strain gradient theories in elasticity. *International Journal of Solids and Structures*, 4:119–124, 1965.

R. Mindlin and H. Tiersten. Effects of couple-stresses in linear elasticity. *Archives of Rational Mechanics and Analysis*, 11:415–448, 1962.

Maher Moakher and Andrew N. Norris. The closest elastic tensor of arbitrary symmetry to an elasticity tensor of lower symmetry. *Journal of Elasticity*, 85(3):215–263, 2006. DOI: 10.1007/s10659-006-9082-0. URL http://link.springer.com/article/10.1007/s10659-006-9082-0.

William D Nix and Huajian Gao. Indentation size effects in crystalline materials: a law for strain gradient plasticity. *Journal of the Mechanics and Physics of Solids*, 46(3):411–425, 1998.

AN Norris and AL Shuvalov. Elastic cloaking theory. *Wave Motion*, 48 (6):525–538, 2011.

Andrew N Norris and Michael R Haberman. Introduction to the special issue on acoustic metamaterials. *The Journal of the Acoustical Society of America*, 132(4):2783–2783, 2012.

Andrew N. Norris and Adam J. Nagy. Metal water: A metamaterial for acoustic cloaking. *Proceedings of Phononics, Santa Fe, New Mexico, USA*, pages 112–113, 2011.

Witold Nowacki. *Theory of asymmetric elasticity*. Pergamon Press, Headington Hill Hall, Oxford OX 3 0 BW, UK, 1986., 1986.

John Frederick Nye et al. *Physical properties of crystals: their representation by tensors and matrices*. Oxford university press, 1985.

Akhilesh Pedgaonkar, Bradley T. Darrall, and Gary F. Dargush. Mixed displacement and couple stress finite element method for anisotropic centrosymmetric materials. *European Journal of Mechanics-A/Solids*, 85:104074, 2021.

Yan Pennec, Jérôme O. Vasseur, Bahram Djafari-Rouhani, Leonard Dobrzyński, and Pierre A. Deymier. Two-dimensional phononic crystals: Examples and applications. *Surface Science Reports*, 65(8):229–291, 2010.

Shivakumar I. Ranganathan and Martin Ostoja-Starzewski. Universal elastic anisotropy index. *Physical Review Letters*, 101(5):055504, 2008.

J.N. Reddy. *Applied Functional Analysis and Variational Methods in Engineering*. Krieger Publishing, 1 edition, 1991.

M Ruzzene and F Scarpa. Directional and band-gap behavior of periodic auxetic lattices. *physica status solidi (b)*, 242(3):665–680, 2005.

Massimo Ruzzene, Fabrizio Scarpa, and Francesco Soranna. Wave beaming effects in two-dimensional cellular structures. *Smart materials and structures*, 12(3):363, 2003.

Nico Schlömer. meshzoo. https://github.com/nschloe/meshzoo, 2020.

David Schurig, JJ Mock, BJ Justice, Steven A Cummer, JB Pendry, AF Starr, and DR Smith. Metamaterial electromagnetic cloak at microwave frequencies. *Science*, 314(5801):977–980, 2006.

Anthony Scopatz and Kathryn D. Huff. *Effective computation in physics: Field guide to research with Python*. O'Reilly Media, Inc., 2015. URL http://physics.codes/.

M. M. Sigalas and Nicolas Garcıa. Theoretical study of three dimensional elastic band gaps with the finite-difference time-domain method. *Journal of Applied Physics*, 87(6):3122–3125, 2000.

Sophia Sklan, Ronald YS Pak, and Baowen Li. Seismic invisibility: elastic wave cloaking via symmetrized transformation media. *New Journal of Physics*, 2018.

Ankit Srivastava. Elastic metamaterials and dynamic homogenization: a review. *International Journal of Smart and Nano Materials*, 6(1):41–60, 2015.

J S Stolken and AG Evans. A microbend test method for measuring the plasticity length scale. *Acta Materialia*, 46(14):5109–5115, 1998.

N. Sukumar and J. E. Pask. Classical and enriched Finite element formulations for Bloch-periodic boundary conditions. *International Journal of Numerical Methods in Engineering*, 77(8):1121–1138, 2 2009.

M. Takeo. Ground rotational motions recorder in near-source region of earthquakes. *Geophysical Research Letters*, 25:789–792, 1998a.

M. Takeo. Ground rotational motions recorder of earthquakes. *Geophysical Research Letters.*, Vol 26:789–792, 1998b.

M. Takeo and H. Ito. What can be learned from rotational motions excited by earthquakes? *International journal of Geophyisics*, 129:319–329, 1997.

Leon Thomsen. Weak elastic anisotropy. *Geophysics*, 51(10):1954–1966, 1986.

Toupin. Elastic materials with couple-stresses. *Archives of Rational Mechanics and Analysis*, 11:385–414, 1962.

Patrizia Trovalusci, Martin Ostoja-Starzewski, Maria Laura De Bellis, and Agnese Murrali. Scale-dependent homogenization of random composites as micropolar continua. *European Journal of Mechanics-A/Solids*, 49:396–407, 2015.

C. Truesdell and R. Toupin. *Principles of Classic Mechanics and Field Theory*. Encyclopedia of Physics. Springer-Verlag, 1960.

Camilo Valencia. *Wave propagation in 2D elastic periodic materials: theoretical and computational analysis*. PhD thesis, Universidad EAFIT, 2019.

Camilo Valencia, Juan Gomez, and Nicolás Guarín-Zapata. A General-Purpose Element-Based Approach to Compute Dispersion Relations in Periodic Materials with Existing Finite Element Codes. *Journal of Theoretical and Computational Acoustics*,

page 1950005, July 2019a. ISSN 2591-7285, 2591-7811. DOI: 10.1142/S2591728519500051. URL https://www.worldscientific.com/doi/abs/10.1142/S2591728519500051.

Camilo Valencia, David Restrepo, Nilesh D Mankame, Pablo D Zavattieri, and Juan Gomez. Computational characterization of the wave propagation behavior of multi-stable periodic cellular materials. *Extreme Mechanics Letters*, 33:100565, 2019b.

Pauli Virtanen, Ralf Gommers, Travis E. Oliphant, Matt Haberland, Tyler Reddy, David Cournapeau, Evgeni Burovski, Pearu Peterson, Warren Weckesser, Jonathan Bright, et al. SciPy 1.0: fundamental algorithms for scientific computing in Python. *Nature methods*, 17(3): 261–272, 2020.

W. Voigt. *Lehrbuch der Kristalphysik*. Teubner, B, 1910.

John R Willis. Negative refraction in a laminate. *Journal of the Mechanics and Physics of Solids*, 97:10–18, 2016.

Fan Yang, ACM Chong, David Chuen Chun Lam, and Pin Tong. Couple stress based strain gradient theory for elasticity. *International Journal of Solids and Structures*, 39(10):2731–2743, 2002.

Arash Yavari and Ashkan Golgoon. Nonlinear and linear elastodynamics transformation cloaking. *arXiv preprint arXiv:1807.10403*, 2018.

Clarence Zener. *Elasticity and anelasticity of metals*. University of Chicago press, 1948.

Xiangdong Zhang and Zhengyou Liu. Negative refraction of acoustic waves in two-dimensional phononic crystals. *Applied Physics Letters*, 85(2):341–343, 2004.

Wave propagation in generalized continua

Introduction

A generalized continuum is one that goes beyond the *standard* Euler-Cauchy definition that involves only a symmetric Cauchy stress tensor. There are three possibilities for this generalization [13]:

- Considering microstructural effects at each material point as additional degrees of freedom, besides the traditional degree of freedom;
- A richer description of the displacement field at each material point by considering higher order gradients of the displacement in the energy density; or
- Using a nonlocal approach that uses spatial functionals as constitutive equations.

[13] Gérard A. Maugin. *Continuum mechanics through the twentieth century*, volume 10 of *Solid Mechanics and Its Applications*. Springer, 2013; and Angela Madeo. *Generalized Continuum Mechanics and Engineering Applications*. Elsevier, 2015

In the classical theory the stress tensor is symmetric. This is a consequence of the balance of angular momentum. This hypothesis works as long as there are no applied couples in the volume or surface and there exists no microstructure described by internal degrees of freedom at each material point. It is not obvious to imagine an applied couple per unit volume while the notion of a force per unit volume is more natural because we know the effects of gravitational or electromagnetic fields. Some of the consequences of the use of a generalized continuum theory is the appearance of a lenght-scale—that does not exit in the case of classical continua—, dispersive behavior of waves, and the need for more material constants.

This chapter discusses general aspects related to wave propagation in micropolar and C-CST solids. The starting point are the equations in terms of displacements that are expressed in Helmholtz potentials to obtain dispersion relations for homogeneous unbounded domains. Furthermore, we present the reflection of plane waves in a free surface (half-space) and its behavior is summarized in terms of reflection coefficients.

Equations of equilibrium and motion

Let us consider a body B of volume V bounded by a surface A as displayed in Figure 33. And consider that this continuum has translational and rotational mechanical interactions between material points in terms of force-traction $t_i^{(\hat{n})}$ and couple-traction $m_i^{(\hat{n})}$ vectors defined through a generalized Cauchy's postulate as [14]:

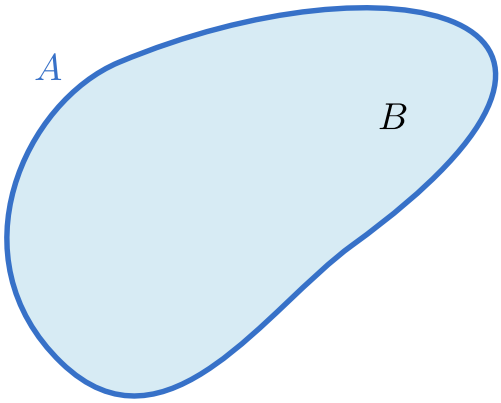

Figure 33: Schematic of a body B of volume V bounded by a surface A.

$$t_i^{(\hat{n})} = \lim_{\Delta S(\hat{n})\to 0} \frac{\Delta R_i}{\Delta S(\hat{n})}\,, \tag{92}$$

$$m_i^{(\hat{n})} = \lim_{\Delta S(\hat{n})\to 0} \frac{\Delta M_i}{\Delta S(\hat{n})}\,, \tag{93}$$

where $\Delta S(\hat{n}))$ is a small element of area oriented with $\hat{n}$, ΔR_i is the resultant force, and ΔM_i is the resultant moment (see Figure 34). Force-tractions and couple-tractions are described by the non-symmetric force-stress σ_{ij} and couple-stress μ_{ij} tensor, written as

$$t_i^{(\hat{n})} = \sigma_{ji} n_j\,,$$
$$m_i^{(\hat{n})} = \mu_{ji} n_j\,.$$

The equations of equilibrium are given by

$$\int_A \mathbf{t}\,\mathrm{d}A + \int_V \mathbf{f}\,\mathrm{d}V = 0\,,$$
$$\int_A (\mathbf{r}\times\mathbf{t}+\mathbf{m})\,\mathrm{d}A + \int_V (\mathbf{r}\times\mathbf{f}+\mathbf{c})\,\mathrm{d}V = 0\,.$$

[14] G. Thomas Mase, Ronald E. Smelser, and George E. Mase. *Continuum mechanics for engineers*. CRC press, 2009

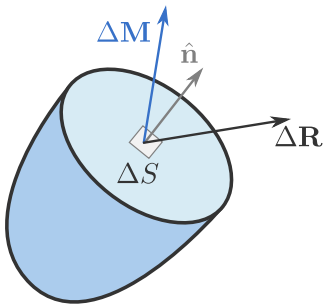

Figure 34: Depiction of the generalized Cauchy principle. We can see the force and moment acting at the surface element ΔS over a plane whose normal is $\hat{n}$.

In Cartesian coordinates these read

$$\int_A t_i \, \mathrm{d}A + \int_V f_i \, \mathrm{d}V = 0 \,,$$
$$\int_A (\epsilon_{ijk} x_j t_k + m_i) \, \mathrm{d}A + \int_V (\epsilon_{ijk} x_j f_k + c_i) \, \mathrm{d}V = 0 \,,$$

using the definitions for the stresses, we obtain

$$\int_A \sigma_{ji} n_j \, \mathrm{d}A + \int_V f_i \, \mathrm{d}V = 0 \,,$$
$$\int_A (\epsilon_{ijk} \sigma_{lk} n_l + \mu_{ji} n_j) \, \mathrm{d}A + \int_V (\epsilon_{ijk} f_k x_j + c_i) \, \mathrm{d}V = 0 \,.$$

After applying the divergence theorem, we get

$$\int_V (\sigma_{ji,j} + f_i) \, \mathrm{d}V = 0 \,,$$
$$\int_V (\epsilon_{ijk} \sigma_{jk} + \mu_{ji,j} + c_i) \, \mathrm{d}V = 0 \,.$$

Since the volume B was arbitrary, we end up with the following equations

$$\sigma_{ji,j} + f_i = 0 \,, \tag{94}$$
$$\epsilon_{ijk} \sigma_{jk} + \mu_{ji,j} + c_i = 0 \,. \tag{95}$$

Similarly, when we have additional degrees of freedom in each material point we end up with the following balance equations for the dynamic case

$$\sigma_{ji,j} + f_i = \rho \ddot{u}_i \tag{96a}$$
$$\sigma_{jk} \epsilon_{ijk} + \mu_{ji,j} + c_i = J \ddot{\theta}_i \tag{96b}$$

where the right-hand-side is different since it now includes translational and rotational inertial terms. In other cases, as the consistent couple-stress theory the balance equations read [15]

[15] Ali R Hadjesfandiari and Gary F Dargush. Couple stress theory for solids. *International Journal of Solids and Structures*, 48(18):2496–2510, 2011

$$\sigma_{ji,j} + f_i = \rho \ddot{u}_i \tag{97a}$$
$$\sigma_{jk}\epsilon_{ijk} + \mu_{ji,j} = 0 \tag{97b}$$

notice that we do not have couples per unit volume or rotational inertia in this case.

Waves in micropolar solids

Displacements equations of motion

The equations of motion for the micropolar are the following[16]:

[16] Witold Nowacki. *Theory of asymmetric elasticity*. Pergamon Press, Headington Hill Hall, Oxford OX 3 0 BW, UK, 1986., 1986

$$(\lambda + 2\mu)\boldsymbol{\nabla}\boldsymbol{\nabla}\cdot\mathbf{u} - (\mu + \alpha)\boldsymbol{\nabla}\times\boldsymbol{\nabla}\times\mathbf{u} + 2\alpha\boldsymbol{\nabla}\times\boldsymbol{\varphi} + \mathbf{f} = \rho\frac{\partial^2\mathbf{u}}{\partial t^2},$$
$$(\beta + 2\gamma)\boldsymbol{\nabla}\boldsymbol{\nabla}\cdot\boldsymbol{\varphi} - (\gamma + \varepsilon)\boldsymbol{\nabla}\times\boldsymbol{\nabla}\times\boldsymbol{\varphi} + 2\alpha\boldsymbol{\nabla}\times\mathbf{u} - 4\alpha\boldsymbol{\varphi} + \mathbf{c} = J\frac{\partial^2\boldsymbol{\varphi}}{\partial t^2}.$$

Equations in terms of potentials

To identify types of propagating waves that can arise in the micropolar medium it is convenient to expand the displacement and rotation vectors in terms of scalar and vector potentials

$$\mathbf{u} = \boldsymbol{\nabla}\phi + \boldsymbol{\nabla}\times\boldsymbol{\Gamma},$$
$$\boldsymbol{\varphi} = \boldsymbol{\nabla}\tau + \boldsymbol{\nabla}\times\mathbf{E},$$

subject to the conditions:

$$\boldsymbol{\nabla}\cdot\boldsymbol{\Gamma} = 0$$
$$\boldsymbol{\nabla}\cdot\mathbf{E} = 0.$$

Using the above in the displacements equations of motion yields, after some manipulations:

$$c_1^2\nabla^2\phi = \frac{\partial^2\phi}{\partial t^2} \tag{98a}$$
$$c_3^2\nabla^2\tau - 2Q^2\tau = \frac{\partial^2\tau}{\partial t^2} \tag{98b}$$
$$\begin{bmatrix} c_2^2\nabla^2 & K^2\boldsymbol{\nabla}\times \\ Q^2\boldsymbol{\nabla}\times & c_4^2\nabla^2 - 2Q^2 \end{bmatrix}\begin{Bmatrix}\boldsymbol{\Gamma}\\ \mathbf{E}\end{Bmatrix} = \frac{\partial^2}{\partial t^2}\begin{Bmatrix}\boldsymbol{\Gamma}\\ \mathbf{E}\end{Bmatrix}. \tag{98c}$$

where we can see that the equations for the scalar potentials are uncoupled, while the ones for the vector potentials are coupled.

To arrive at (98a) we have neglected body forces and body couples and have written the displacement equations of motions in the alternative form:

$$c_1^2\boldsymbol{\nabla}\boldsymbol{\nabla}\cdot\mathbf{u} - c_2^2\boldsymbol{\nabla}\times\boldsymbol{\nabla}\times\mathbf{u} + K^2\boldsymbol{\nabla}\times\boldsymbol{\varphi} = \frac{\partial^2\mathbf{u}}{\partial t^2}, \tag{99a}$$
$$c_3^2\boldsymbol{\nabla}\boldsymbol{\nabla}\cdot\boldsymbol{\varphi} - c_4^2\boldsymbol{\nabla}\times\boldsymbol{\nabla}\times\boldsymbol{\varphi} + Q^2\boldsymbol{\nabla}\times\mathbf{u} - 2Q^2\boldsymbol{\varphi} = \frac{\partial^2\boldsymbol{\varphi}}{\partial t^2}, \tag{99b}$$

where we have used the following relations:

$$c_1^2 = \frac{\lambda + 2\mu}{\rho}, \quad c_3^2 = \frac{\beta + 2\gamma}{J},$$
$$c_2^2 = \frac{\mu + \alpha}{\rho}, \quad c_4^2 = \frac{\gamma + \varepsilon}{J},$$
$$K^2 = \frac{2\alpha}{\rho}, \quad Q^2 = \frac{2\alpha}{J},$$

Dispersion relations

Writing the vector potentials as plane waves of amplitude **A** and **B**, wave number κ and circular frequency ω that propagate along the x axis,

$$\boldsymbol{\Gamma} = \mathbf{A}\exp(i\kappa x - i\omega t)$$
$$\mathbf{E} = \mathbf{B}\exp(i\kappa x - i\omega t),$$

and using these in the equations of motion yields:

$$\begin{bmatrix} M_{11} & M_{12} \\ M_{21} & M_{22} \end{bmatrix} \begin{Bmatrix} \mathbf{A} \\ \mathbf{B} \end{Bmatrix} = \mathbf{0},$$

where

$$M_{11} = (c_2^2\kappa^2 - \omega^2)\begin{bmatrix} 1 & 0 & 0 \\ 0 & 1 & 0 \\ 0 & 0 & 1 \end{bmatrix},$$
$$M_{12} = \begin{bmatrix} 0 & 0 & 0 \\ 0 & 0 & iK^2\kappa \\ 0 & -iK^2\kappa & 0 \end{bmatrix},$$
$$M_{21} = \begin{bmatrix} 0 & 0 & 0 \\ 0 & 0 & iQ^2\kappa \\ 0 & -iQ^2\kappa & 0 \end{bmatrix},$$
$$M_{22} = (2Q^2 + c_4^2\kappa^2 - \omega^2)\begin{bmatrix} 1 & 0 & 0 \\ 0 & 1 & 0 \\ 0 & 0 & 1 \end{bmatrix}.$$

For non-trivial solutions to exist it is required that

$$\det \begin{bmatrix} M_{11} & M_{12} \\ M_{21} & M_{22} \end{bmatrix} = 0,$$

which leads to the following frequency-wave number (or dispersion) relations for the coupled waves

$$\omega^2 = Q^2 + \frac{c_2^2\kappa^2}{2} + \frac{c_4^2\kappa^2}{2} \mp \frac{1}{2}\sqrt{4K^2Q^2\kappa^2 + 4Q^4 - 4Q^2c_2^2\kappa^2 + 4Q^2c_4^2\kappa^2 + c_2^4\kappa^4 - 2c_2^2c_4^2\kappa^4 + c_4^4\kappa^4},$$

and where the minus signs corresponds to the transverse wave while the plus sign corresponds to the rotational wave.

The dispersion relations for the different propagating waves are given by

$$\omega_P = c_1\kappa\,, \tag{100}$$

$$\omega_{RL} = \sqrt{2Q^2 + c_3^2\kappa^2}\,, \tag{101}$$

$$\omega_S = \sqrt{Q^2 + \frac{(c_2^2+c_4^2)}{2}\kappa^2 - \frac{1}{2}\sqrt{4Q^4 + 4Q^2[(c_4^2-c_2^2)+K^2]\kappa^2 + (c_4^2-c_2^2)^2\kappa^4}}\,, \tag{102}$$

$$\omega_{RT} = \sqrt{Q^2 + \frac{(c_2^2+c_4^2)}{2}\kappa^2 + \frac{1}{2}\sqrt{4Q^4 + 4Q^2[(c_4^2-c_2^2)+K^2]\kappa^2 + (c_4^2-c_2^2)^2\kappa^4}}\,, \tag{103}$$

Notice that the only wave that is not dispersive is the P-wave, since the relationship between wavenumber and frequency is linear.

Wave speeds

We can write the phase speeds $v_i \equiv \omega_i/\kappa$, to obtain

$$v_P = c_1\,, \tag{104}$$

$$v_{RL} = \sqrt{\frac{2Q^2}{\kappa^2} + c_3^2}\,, \tag{105}$$

$$v_S = \sqrt{\frac{Q^2}{\kappa^2} + \frac{(c_2^2+c_4^2)}{2} - \frac{1}{2}\sqrt{\frac{4Q^4}{\kappa^4} + \frac{4Q^2}{\kappa^2}[(c_4^2-c_2^2)+K^2] + (c_4^2-c_2^2)^2}}\,, \tag{106}$$

$$v_{RT} = \sqrt{\frac{Q^2}{\kappa^2} + \frac{(c_2^2+c_4^2)}{2} + \frac{1}{2}\sqrt{\frac{4Q^4}{\kappa^4} + \frac{4Q^2}{\kappa^2}[(c_4^2-c_2^2)+K^2] + (c_4^2-c_2^2)^2}}\,, \tag{107}$$

if we take the limit $\kappa \to 0$, we obtain

$$\lim_{\kappa\to 0} v_S = \sqrt{c_2^2 - \frac{K^2}{2}} = \sqrt{\frac{\mu}{\rho}}\,,$$

that corresponds to the phase speed of the shear wave in classical media. And, if we take the high frequency limit ($\kappa \to \infty$), we find that

$$\lim_{\kappa\to\infty} v_{RL} = c_3\,,$$
$$\lim_{\kappa\to\infty} v_S = c_2\,,$$
$$\lim_{\kappa\to\infty} v_{RT} = c_4\,.$$

We can also compute the group speed $g_i = \partial\omega_i/\partial\kappa$, to obtain

$$g_P = c_1\,, \tag{108}$$

$$g_{RL} = \frac{c_3^2\kappa}{\omega_{RL}}\,, \tag{109}$$

$$g_S = \frac{1}{2\omega_S}\left[(c_2^2+c_4^2)\kappa - \frac{2Q^2[(c_4^2-c_2^2)+K^2]\kappa + (c_4^2+c_2^2)^2\kappa^3}{\sqrt{4Q^4+4Q^2[(c_4^2-c_2^2)+K^2]\kappa^2+(c_4^2-c_2^2)^2\kappa^4}}\right]\,, \tag{110}$$

$$g_{RT} = \frac{1}{2\omega_{RT}}\left[(c_2^2+c_4^2)\kappa + \frac{2Q^2[(c_4^2-c_2^2)+K^2]\kappa + (c_4^2+c_2^2)^2\kappa^3}{\sqrt{4Q^4+4Q^2[(c_4^2-c_2^2)+K^2]\kappa^2+(c_4^2-c_2^2)^2\kappa^4}}\right]\,, \tag{111}$$

if we take the limit $\kappa \to 0$, we obtain

$$\begin{aligned}
&\lim_{\kappa\to 0} g_{RL} = 0\,,\\
&\lim_{\kappa\to 0} g_S = \lim_{\kappa\to 0} v_S = \sqrt{c_2^2 - \frac{K^2}{2}} = \sqrt{\frac{\mu}{\rho}}\,,\\
&\lim_{\kappa\to 0} g_{RT} = 0\,.
\end{aligned}$$

And in the high frequency limit ($\kappa \to \infty$), we find that

$$\begin{aligned}
\lim_{\kappa\to\infty} g_{RL} &= \lim_{\kappa\to\infty} v_{RL} = c_3\,,\\
\lim_{\kappa\to\infty} g_S &= \lim_{\kappa\to\infty} v_S = c_2\,,\\
\lim_{\kappa\to\infty} g_{RT} &= \lim_{\kappa\to\infty} v_{RT} = c_4\,.
\end{aligned}$$

The dispersion relation can be exemplified in Figure 35. Where we can see the cut-off frequency for the rotational wave and the limit cases for the phase and group speeds.

Dispersion relations as functions of frequency

In some applications it is useful to have the dispersion relations as functions of frequency instead of wavenumber. In this case they are given by

$$\kappa_P = \frac{\omega}{c_1}\,, \tag{112}$$

$$\kappa_{RL} = \frac{\sqrt{\omega^2 - 2Q^2}}{c_3}\,, \tag{113}$$

$$\kappa_S = \sqrt{\frac{D}{2} + \frac{1}{2}\sqrt{D^2-4E}}\,, \tag{114}$$

$$\kappa_{RT} = \sqrt{\frac{D}{2} - \frac{1}{2}\sqrt{D^2-4E}}\,, \tag{115}$$

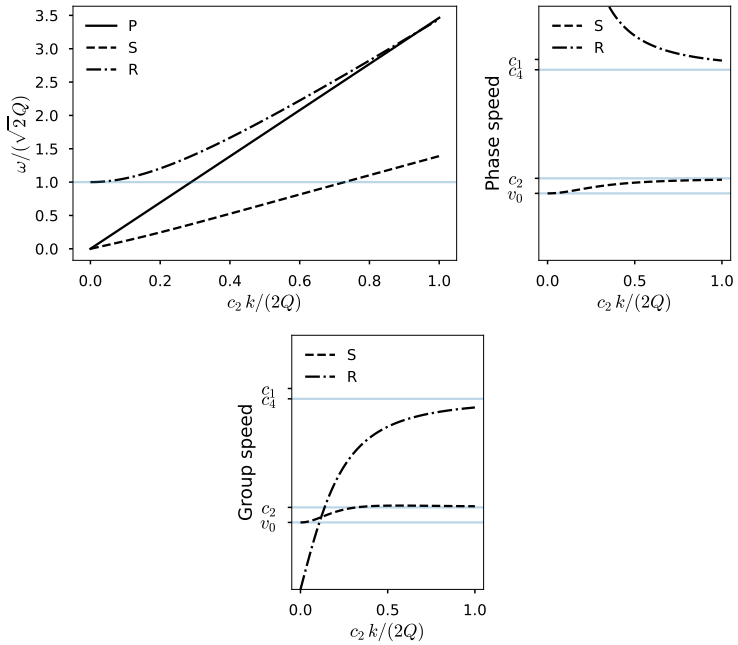

Figure 35: Dispersion relations for a material with properties: $\rho = 1 \times 10^5$, $J = 1 \times 10^4$, $\lambda = 2.8 \times 10^{10}$, $\gamma + \epsilon = 1.62 \times 10^9$, $\mu = 4 \times 10^9$, $\alpha = 2 \times 10^9$.

with

$$D = \frac{1}{2c_2^2c_4^2}\left[(c_2^2+c_4^2)\omega^2 - 2Q^2\left(c_2^2 - \frac{K^2}{2}\right)\right],$$
$$E = \frac{2Q^2\omega^2}{c_2^2c_4^2} - \frac{\omega^4}{c_2^2c_4^2}.$$

We can also write the slowness for each wave as

$$s_P(\omega) \equiv \frac{1}{v_P(\omega)} = \frac{1}{c_1}, \tag{116}$$
$$s_{RL}(\omega) \equiv \frac{1}{v_{RL}(\omega)} = \sqrt{\frac{1}{c_3} - \frac{2Q^2}{\omega^2 c_3^2}}, \tag{117}$$
$$s_S(\omega) \equiv \frac{1}{v_S(\omega)} = \frac{\kappa_S}{\omega}, \tag{118}$$
$$s_{RT}(\omega) \equiv \frac{1}{v_{RT}(\omega)} = \frac{\kappa_R}{\omega}. \tag{119}$$

Reflection of a plane wave on a plane boundary

Let us consider now the problem of a plane boundary, as shown in the following schematic.

If we consider waves lying on the zx plane, the equations of motions

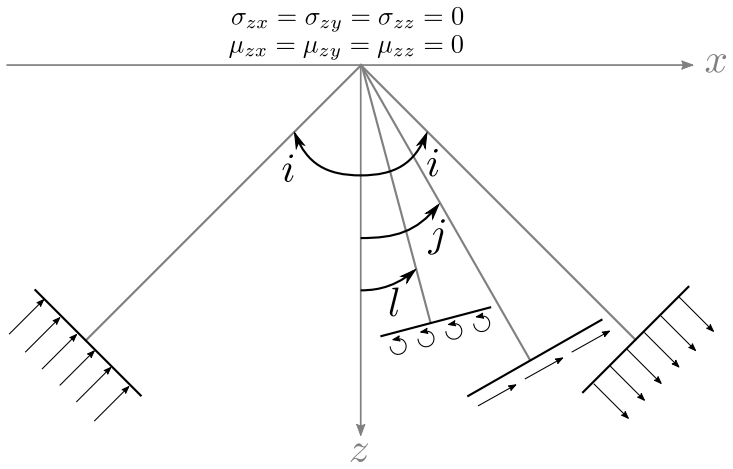

Figure 36: Schematic for analysis of reflected waves set up by a plane P-wave incident on the free surface of a micropolar half-space.

reduce to

$$c_1^2\left[\frac{\partial^2 u_x}{\partial x^2}+\frac{\partial^2 u_z}{\partial x \partial z}\right]-c_2^2\left[\frac{\partial^2 u_z}{\partial x \partial z}-\frac{\partial^2 u_x}{\partial z^2}\right]-K^2\frac{\partial \phi_y}{\partial z}=\ddot{u_x}\,,$$
$$c_1^2\left[\frac{\partial^2 u_x}{\partial x \partial z}+\frac{\partial^2 u_z}{\partial z^2}\right]-c_2^2\left[\frac{\partial^2 u_x}{\partial x \partial z}-\frac{\partial^2 u_z}{\partial z^2}\right]+K^2\frac{\partial \phi_y}{\partial x}=\ddot{u_z}\,,$$
$$Q^2\left[\frac{\partial u_x}{\partial z}-\frac{\partial u_z}{\partial x}\right]+c_4^2\left[\frac{\partial^2 \phi_y}{\partial x^2}+\frac{\partial^2 \phi_y}{\partial z^2}\right]-2Q^2\phi_y=\ddot{\phi}_y\,.$$

And the strain and curvature tensors are

$$\gamma=\begin{bmatrix}\frac{\partial u_x}{\partial x} & 0 & \frac{\partial u_z}{\partial x}+\phi_y\\ 0 & 0 & 0\\ \frac{\partial u_x}{\partial z}-\phi_y & 0 & \frac{\partial u_z}{\partial z}\end{bmatrix},$$
$$\kappa=\begin{bmatrix}0 & \frac{\partial \phi_y}{\partial x} & 0\\ 0 & 0 & 0\\ 0 & \frac{\partial \phi_y}{\partial z} & 0\end{bmatrix}.$$

While the force-stress and couple-stress tensor read

$$\sigma=\begin{bmatrix}(\lambda+2\mu)\frac{\partial u_x}{\partial x}+\lambda\frac{\partial u_x}{\partial z} & 0 & (\mu+\alpha)\frac{\partial u_x}{\partial z}+(\mu-\alpha)\frac{\partial u_z}{\partial x}-2\alpha\phi_y\\ 0 & \lambda\left(\frac{\partial u_x}{\partial x}+\frac{\partial u_z}{\partial z}\right) & 0\\ (\mu-\alpha)\frac{\partial u_x}{\partial z}+(\mu+\alpha)\frac{\partial u_z}{\partial x}+2\alpha\phi_y & 0 & \lambda\frac{\partial u_x}{\partial x}+(\lambda+2\mu)\frac{\partial u_z}{\partial z}\end{bmatrix},$$
$$\mu=\begin{bmatrix}0 & (\gamma-\epsilon)\frac{\partial \phi_y}{\partial x} & 0\\ (\gamma+\epsilon)\frac{\partial \phi_y}{\partial x} & 0 & (\gamma+\epsilon)\frac{\partial \phi_y}{\partial z}\\ 0 & (\gamma-\epsilon)\frac{\partial \phi_y}{\partial z} & 0\end{bmatrix}.$$

For this problem the following boundary conditions should be sat-

isfied

$$\sigma_{zx} = \sigma_{zz} = \mu_{zy} = 0\,,$$

with

$$\begin{aligned}
\sigma_{zx} &= (\mu - \alpha)\frac{\partial u_x}{\partial z} + (\mu + \alpha)\frac{\partial u_z}{\partial x} + 2\alpha\phi_y\,,\\
\sigma_{zz} &= \lambda\frac{\partial u_x}{\partial x} + (\lambda + 2\mu)\frac{\partial u_z}{\partial z}\,,\\
\mu_{zy} &= (\gamma - \epsilon)\frac{\partial \phi_y}{\partial z}\,.
\end{aligned}$$

Since the problem is limited to the zx plane, all the waves can be described by 3 scalar potentials, namely:

- For P:
$$u^P = \left(\frac{\partial \psi^P}{\partial x}, 0, \frac{\partial \psi^P}{\partial z}\right)\,.$$
- For SV:
$$u^S = \left(-\frac{\partial \psi^S}{\partial z}, 0, \frac{\partial \psi^S}{\partial x}\right)\,.$$
- For RT:
$$\phi^R = \left(0, \frac{\partial \psi^R}{\partial z}, 0\right)\,.$$

Leading to the following (partial) traction vectors

$$\begin{aligned}
T^P &= \left(2\mu\frac{\partial^2 \psi^P}{\partial z \partial x} + 2\alpha\frac{\partial \psi^R}{\partial z}, 0, \lambda\nabla^2\psi^P + 2\mu\frac{\partial^2 \psi^P}{\partial z^2}\right)\,,\\
T^S &= \left(\mu\left(\frac{\partial^2 \psi^S}{\partial x^2} - \frac{\partial^2 \psi^S}{\partial z^2}\right) + \alpha\nabla^2\psi^S + 2\alpha\frac{\partial \psi^{RT}}{\partial z}, 0, 2\mu\frac{\partial^2 \psi^S}{\partial z \partial x}\right)\,,\\
M^R &= \left(0, (\gamma - \epsilon)\frac{\partial^2 \psi^R}{\partial z^2}, 0\right)\,.
\end{aligned}$$

The potentials can be written as

$$\begin{aligned}
\psi^P &= \psi^{P,i} + \psi^{P,r}\,,\\
\psi^S &= \psi^{R,r}\,,\\
\psi^R &= \psi^{R,r}\,,
\end{aligned}$$

where the superscripts i and r refer to the incident and reflected waves. They can be written as plane waves

$$\begin{aligned}
\psi^{P,i} &= A\exp\left[i\omega(px - p_1 z - t)\right]\,,\\
\psi^{P,r} &= B\exp\left[i\omega(px + p_1 z - t)\right]\,,\\
\psi^{S,r} &= C\exp\left[i\omega(px + p_2 z - t)\right]\,,\\
\psi^{R,r} &= D\exp\left[i\omega(px + p_4 z - t)\right]\,,
\end{aligned}$$

with

$$p = \frac{\sin i}{v_1} = \frac{\sin j}{v_2} = \frac{\sin l}{v_4},$$

the horizontal components of the slowness vectors, and,

$$p_1 = \frac{\cos i}{v_1}, \quad p_2 = \frac{\cos j}{v_2}, \quad p_4 = \frac{\cos l}{v_4},$$

the vertical components of the slowness vectors.

Taking into account that

$$\begin{aligned} \lambda &= \rho c_1^2 - \rho c_2^2, & p_1^2 &= \frac{1}{c_1^2} - p^2, \\ \mu &= \rho c_2^2, & p_2^2 &= \frac{1}{v_2^2} - p^2, \\ 2\alpha &= \rho K^2, & p_4^2 &= \frac{1}{v_4^2} - p^2, \end{aligned}$$

we get

$$\begin{aligned} v_2^2 p p_1 (A - B) + (1 - 2v_2^2 p^2) C - \frac{K^2}{2c_2^2} C = 0\,, \\ (1 - 2c^2 p^2)(A + B) + 2c_2 p p_2 C = 0\,, \end{aligned}$$

and

$$D\omega^2 p_4^2 (\gamma - \epsilon) = 0\,.$$

The last equation implies $D = 0$, meaning that an incident P-wave does not generate a reflected RT-wave.

If we solve the last two equation for the ratios B/A and C/A, we get

$$\begin{aligned} \frac{B}{A} &= \frac{4c_2^4 p^2 p_1 p_2 - \left[\frac{c_2^2}{v_2^2}(1 - 2c_2^2 p^2)(1 - 2v_2^2 p^2) - \frac{K^2}{2v_2^2}(1 - 2c_2 p^2)\right]}{4c_2^4 p^2 p_1 p_2 + \left[\frac{c_2^2}{v_2^2}(1 - 2c_2^2 p^2)(1 - 2v_2^2 p^2) - \frac{K^2}{2v_2^2}(1 - 2c_2 p^2)\right]}, \\ \frac{C}{A} &= \frac{4c_2^2 p p_1 (1 - 2c_2^2 p^2)}{4c_2^4 p^2 p_1 p_2 + \left[\frac{c_2^2}{v_2^2}(1 - 2c_2^2 p^2)(1 - 2v_2^2 p^2) - \frac{K^2}{2v_2^2}(1 - 2c_2 p^2)\right]}, \end{aligned}$$

where the limits $v_2 \to c_2$ and $K \to 0$ clearly lead to the classical version of the coefficients [Aki and Richards, 2002]. And, we can obtain the reflection coefficients for the displacements multiplying the amplitude of the potential by the slowness of each wave.

The reflection coefficients for displacements for an incident P-wave

are (following the notation of [Aki and Richards, 2002])

$$\acute{P}\grave{P} = \frac{-\left[\left(\frac{1}{c_2^2}-2p^2\right)\left(\frac{1}{v_2^2}-2p^2\right)-\frac{K^2}{2c_2^2v_2^2}\left(\frac{1}{c_2^2}-2p^2\right)\right]+4p^2p_1p_2}{\left[\left(\frac{1}{c_2^2}-2p^2\right)\left(\frac{1}{v_2^2}-2p^2\right)-\frac{K^2}{2c_2^2v_2^2}\left(\frac{1}{c_2^2}-2p^2\right)\right]+4p^2p_1p_2}, \tag{120}$$

$$\acute{P}\grave{S} = \frac{4\frac{c_1}{v_2}pp_1\left(\frac{1}{c_2^2}-2p^2\right)}{\left[\left(\frac{1}{c_2^2}-2p^2\right)\left(\frac{1}{v_2^2}-2p^2\right)-\frac{K^2}{2c_2^2v_2^2}\left(\frac{1}{c_2^2}-2p^2\right)\right]+4p^2p_1p_2}. \tag{121}$$

Similarly, the reflection coefficients for displacements for an incident S-wave are

$$\acute{S}\grave{S} = \frac{\left[\left(\frac{1}{c_2^2}-2p^2\right)\left(\frac{1}{v_2^2}-2p^2\right)-\frac{K^2}{2c_2^2v_2^2}\left(\frac{1}{c_2^2}-2p^2\right)\right]-4p^2p_1p_2}{\left[\left(\frac{1}{c_2^2}-2p^2\right)\left(\frac{1}{v_2^2}-2p^2\right)-\frac{K^2}{2c_2^2v_2^2}\left(\frac{1}{c_2^2}-2p^2\right)\right]+4p^2p_1p_2}, \tag{122}$$

$$\acute{S}\grave{P} = \frac{4\frac{v_2}{c_1}pp_2\left(\frac{1}{v_2^2}-2p^2\right)-\frac{2pp_2K^2}{v_2^2c_2^2}}{\left[\left(\frac{1}{c_2^2}-2p^2\right)\left(\frac{1}{v_2^2}-2p^2\right)-\frac{K^2}{2c_2^2v_2^2}\left(\frac{1}{c_2^2}-2p^2\right)\right]+4p^2p_1p_2}. \tag{123}$$

where the limits $v_2 \to c_2$ and $K \to 0$ also lead to the classical version of the coefficients.

If we repeat the same process for the incident RT-wave we obtain the following coefficients

$$\acute{R}\grave{R} = -1, \tag{124}$$

$$\acute{R}\grave{P} = -\frac{3ic_1p_4K^2}{2\omega c_2^2v_4pp_1}, \tag{125}$$

$$\acute{R}\grave{S} = \frac{3iv_2p_4K^2\left(\frac{1}{c_2^2}-2p^2\right)}{4\omega c_2^2v_4^2pp_1}, \tag{126}$$

where we highlight that the coefficients $\acute{R}\grave{P}$ and $\acute{R}\grave{S}$ have units of length and represent evanescent waves that decay with z.

In the general case we have the following scattering matrix

$$\begin{pmatrix} \acute{P}\grave{P} & \acute{S}\grave{P} & \acute{R}\grave{P} \\ \acute{P}\grave{S} & \acute{S}\grave{S} & \acute{R}\grave{S} \\ 0 & 0 & \acute{R}\grave{R} \end{pmatrix}.$$

Waves in Corrected Couple-Stress Theory

Wave speeds

As presented in Hadjesfandiari and Dargush, the equations of motion in terms of displacements for the Corrected Couple-Stress Theory (C-CST) are

$$c_1^2 \nabla(\nabla \cdot \mathbf{u}) - c_2^2 \nabla \times \nabla \times \mathbf{u} + l^2 c_2^2 \nabla^2 \nabla \times \nabla \times \mathbf{u} = \ddot{\mathbf{u}} \,,$$

with

$$\begin{aligned} c_1^2 &= \frac{\lambda + 2\mu}{\rho} \,, \\ c_2^2 &= \frac{\mu}{\rho} \,, \\ l^2 &= \frac{\eta}{\mu} \,. \end{aligned}$$

For this model the dispersion relations are simpler, i.e.,

$$\begin{aligned} \omega_P^2 &= c_1^2 \kappa^2 \,, \\ \omega_S^2 &= c_2^2 \kappa^2 (1 + \kappa^2 l^2) \,, \end{aligned}$$

or, isolating κ,

$$\begin{aligned} \kappa_P^2 &= \frac{\omega^2}{c_2^2} \,, \\ \kappa_S^2 &= \frac{1}{2l^2} \left[\pm \sqrt{1 + \frac{4\omega^2 l^2}{c_2^2}} - 1 \right] \,, \end{aligned}$$

we can see that the number inside the square root is always greater than 1. We should, then, only consider the positive root. The other root presents an evanescent wave that should arise when satisfying boundary conditions.

The phase speeds are given by

$$\begin{aligned} v_P &= c_1 \,, \\ v_S(\kappa) &= c_2 \sqrt{1 + \kappa^2 l^2} \,, \end{aligned}$$

or as a function of frequency

$$\begin{aligned} v_P &= c_1 \,, \\ v_S(\omega) &= c_2 \sqrt{1 + \frac{1}{2} \left[\sqrt{1 + \frac{4\omega^2 l^2}{c_2^2}} - 1 \right]} \,. \end{aligned}$$

If we take the limit $\kappa \to 0$, we obtain

$$\lim_{\kappa \to 0} v_S = c_2 \,,$$

and, taking the limit $\kappa \to \infty$, we obtain

$$\lim_{\kappa \to \infty} v_S \to \infty \,.$$

Group speeds are given by

$$g_P = c_1 \,,$$
$$g_S = c_2 \frac{1 + 2\kappa^2 l^2}{\sqrt{1 + \kappa^2 l^2}} \,,$$

taking the same limits, we obtain

$$\lim_{\kappa \to 0} g_S = c_2 \,,$$

and

$$\lim_{\kappa \to \infty} g_S \to \infty \,,$$

meaning that the speed of energy flow increases as the frequency increases.

As in the case micropolar media, we can summarize these results graphically as in Figure 37.

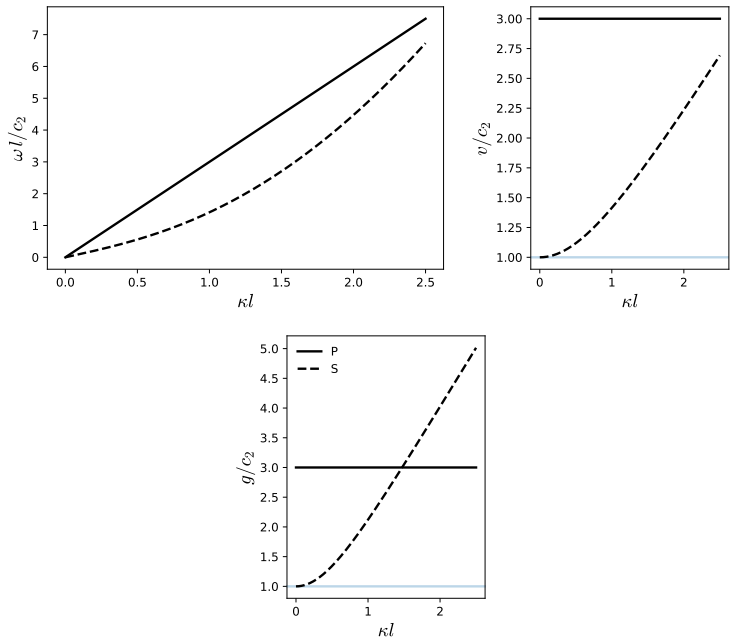

Figure 37: Dispersion relations for a material with properties: $\rho = 1 \times 10^5$, $\lambda = 2.8 \times 10^{10}$, $\mu = 4 \times 10^9$, $\eta = 1.6 \times 10^9$.

Reflection of a plane wave on a plane boundary

We can repeat the process followed before to obtain reflection coefficients for the case of the C-CST. For completeness some of the steps will be repeated in this section.

The motion is constrained to the plane zx plane, what gives the following displacement vector

$$\mathbf{u} = (u_x, 0, u_z)\,,$$

the following infinitesimal strain and rotation tensor

$$\epsilon = \begin{bmatrix} \frac{\partial u_x}{\partial x} & 0 & \frac{1}{2}\left(\frac{\partial u_x}{\partial z} + \frac{\partial u_z}{\partial x}\right) \\ 0 & 0 & 0 \\ \frac{1}{2}\left(\frac{\partial u_x}{\partial z} + \frac{\partial u_z}{\partial x}\right) & 0 & \frac{\partial u_z}{\partial z} \end{bmatrix},$$

$$\omega = \begin{bmatrix} 0 & 0 & \frac{1}{2}\left(\frac{\partial u_x}{\partial z} - \frac{\partial u_z}{\partial x}\right) \\ 0 & 0 & 0 \\ \frac{1}{2}\left(\frac{\partial u_z}{\partial x} - \frac{\partial u_x}{\partial z}\right) & 0 & 0 \end{bmatrix},$$

and the following stress tensor

$$\sigma = \begin{bmatrix} (\lambda + 2\mu)\frac{\partial u_x}{\partial x} + \lambda\frac{\partial u_z}{\partial z} & 0 & \mu\left(\frac{\partial u_x}{\partial z} + \frac{\partial u_z}{\partial x}\right) + \frac{\eta}{2}\nabla^2\left(\frac{\partial u_x}{\partial z} - \frac{\partial u_z}{\partial x}\right) \\ 0 & 0 & 0 \\ \frac{\mu}{2}\left(\frac{\partial u_x}{\partial z} + \frac{\partial u_z}{\partial x}\right) - \eta\nabla^2\left(\frac{\partial u_x}{\partial z} - \frac{\partial u_z}{\partial x}\right) & 0 & (\lambda + 2\mu)\frac{\partial u_z}{\partial z} + \lambda\frac{\partial u_x}{\partial x} \end{bmatrix}.$$

In this case the traction-free boundary conditions imply $\sigma_{zx} = \sigma_{zy} = \sigma_{zz} = 0$, that is

$$\sigma_{zx} = \frac{\mu}{2}\left(\frac{\partial u_x}{\partial z} + \frac{\partial u_z}{\partial x}\right) - \eta\nabla^2\left(\frac{\partial u_x}{\partial z} - \frac{\partial u_z}{\partial x}\right) = 0$$
$$\sigma_{zz} = (\lambda + 2\mu)\frac{\partial u_z}{\partial z} + \lambda\frac{\partial u_x}{\partial x} = 0\,,$$

and we know that

$$\mathbf{u}^P = \left(\frac{\partial \psi^P}{\partial x}, 0, \frac{\partial \psi^P}{\partial z}\right),$$
$$\mathbf{u}^S = \left(-\frac{\partial \psi^S}{\partial z}, 0, \frac{\partial \psi^S}{\partial x}\right),$$

where the superscript refer to the type of wave and ψ^i is a scalar potential.

Thus, we have the following tractions

$$T^P = \left(\mu\frac{\partial^2 \psi^P}{\partial z \partial x}, 0, \lambda\frac{\partial^2 \psi^P}{\partial x^2} + (\lambda + 2\mu)\frac{\partial^2 \psi^P}{\partial z^2}\right),$$
$$T^S = \left(\frac{\mu}{2}\left(\frac{\partial^2 \psi^S}{\partial x^2} - \frac{\partial^2 \psi^S}{\partial z^2}\right) + \eta\nabla^2\nabla^2\psi^S, 0, 2\mu\frac{\partial^2 \psi^S}{\partial z \partial x}\right).$$

If we solve the resulting system of equations we obtain the following

reflection coefficients for displacements

$$\acute{P}\grave{P} = \frac{-\left(\frac{1}{c_2^2}-2p^2\right)\left(\frac{1}{v_2^2}-2p^2+\frac{2l^2\omega^2}{v_2^4}\right)+4p^2p_1p_2}{\left(\frac{1}{c_2^2}-2p^2\right)\left(\frac{1}{v_2^2}-2p^2+\frac{2l^2\omega^2}{v_2^4}\right)+4p^2p_1p_2},$$

$$\acute{P}\grave{S} = \frac{4\frac{c_1}{v_2}pp_1\left(\frac{1}{c_2^2}-2p^2\right)}{\left(\frac{1}{c_2^2}-2p^2\right)\left(\frac{1}{v_2^2}-2p^2+\frac{2l^2\omega^2}{v_2^4}\right)+4p^2p_1p_2},$$

$$\acute{S}\grave{S} = \frac{\left(\frac{1}{c_2^2}-2p^2\right)\left(\frac{1}{v_2^2}-2p^2+\frac{2l^2\omega^2}{v_2^4}\right)-4p^2p_1p_2}{\left(\frac{1}{c_2^2}-2p^2\right)\left(\frac{1}{v_2^2}-2p^2+\frac{2l^2\omega^2}{v_2^4}\right)+4p^2p_1p_2},$$

$$\acute{S}\grave{P} = \frac{4\frac{v_2}{c_1}pp_2\left(\frac{1}{v_2^2}-2p^2+\frac{2l^2\omega^2}{v_2^4}\right)}{\left(\frac{1}{c_2^2}-2p^2\right)\left(\frac{1}{v_2^2}-2p^2+\frac{2l^2\omega^2}{v_2^4}\right)+4p^2p_1p_2},$$

where the limits $v_2 \to c_2$ and $K \to 0$ clearly lead to the classical version of the coefficients [Aki and Richards, 2002].

Figure 38: Reflection of an incident P-wave on a halfspace for different length scales. The angle of incidence is $\pi/6$ rad, the P-wave speed is $c_1 = 2$, the (classical) S-wave speed is $c_2 = 1$, and the length scales are $l = \{0.01, 0.03, 0.1\}$ (from top to bottom). It is clearly seen how the dispersion increases while the length scale parameter increases.

Software developed

As part of the present work the following Python packages were developed:

- SolidsPy
- Continuum Mechanics

SolidsPy

SolidsPy is a simple finite element analysis code for 2D elasticity problems. The code uses as input simple-to-create text files defining a model in terms of nodal, element, material and load data.[17]

Some of SolidsPy's features are:

- It is based on an open-source environment.
- It is easy to use.
- The code allows to find displacement, strain and stress solutions for arbitrary two-dimensional domains discretized into finite elements and subject to point loads.
- The code is organized in independent modules for pre-processing, assembly and post-processing allowing the user to easily modify it or add features like new elements or analyses pipelines.
- It was created with academic and research purposes.
- It has been used to tech the following courses:
  - Computational Modeling.
  - Introduction to the Finite Element Methods.

[17] Nicolás Guarín-Zapata and Juan Gómez. SolidsPy: 2D-Finite Element Analysis with Python, 2020. URL https://github.com/AppliedMechanics-EAFIT/SolidsPy

How to run a simple model

Let's suppose that we have a simple model represented by the following files:

```
import numpy as np
from solidspy.solids_GUI import solids_auto

### Define the data
nodes = np.array([
[0, 0.00, 0.00],
[1, 2.00, 0.00],
[2, 2.00, 2.00],
[3, 0.00, 2.00],
[4, 1.00, 0.00],
[5, 2.00, 1.00],
[6, 1.00, 2.00],
[7, 0.00, 1.00],
[8, 1.00, 1.00]])

cons = np.array([
[0, -1],
[0, -1],
[0,  0],
[0,  0],
[-1, -1],
[0,  0],
[0,  0],
[0,  0],
[0,  0]])

elements = np.array([
[0, 1, 0, 0, 4, 8, 7],
[1, 1, 0, 4, 1, 5, 8],
[2, 1, 0, 7, 8, 6, 3],
[3, 1, 0, 8, 5, 2, 6]])

mats = np.array([[1.0, 0.3]])

loads = np.array([
[2, 0.0, 1.0],
[3, 0.0, 1.0],
[6, 0.0, 2.0]])

data = {"nodes": nodes,
```

```
    "cons": cons,
    "elements": elements,
    "mats": mats,
    "loads": loads}

### Run the simulation
disp = solids_auto(data)
plt.show()
```

Save it as `example_solidspy.py` and run it in your terminal:

```
python example_solidspy.py
```

Continuum Mechanics

Continuum Mechanics provides utilities for doing calculations in continuum mechanics[18]. Some of its features are:

- Make long vector calculus calculations simple.
- Support different coordinate systems.
- Visualize entities such as second rank tensors.

[18] Nicolás Guarín-Zapata. continuum_mechanics: Continuum Mechanics calculations in Python, 2020. URL https://github.com/nicoguaro/continuum_mechanics

Dispersion relations in a micropolar medium

We are interested in computing the dispersion relations in a homogeneous micropolar solid. The equations of motion for a micropolar solid are given by [19]

$$c_1^2 \nabla\nabla\cdot\mathbf{u} - c_2^2 \nabla\times\nabla\times\mathbf{u} + K^2\nabla\times\boldsymbol{\theta} = -\omega^2\mathbf{u}\,,$$
$$c_3^2 \nabla\nabla\cdot\boldsymbol{\theta} - c_4^2 \nabla\times\nabla\times\boldsymbol{\theta} + Q^2\nabla\times\mathbf{u} - 2Q^2\boldsymbol{\theta} = -\omega^2\boldsymbol{\theta}$$

[19] Witold Nowacki. *Theory of asymmetric elasticity*. Pergamon Press, Headington Hill Hall, Oxford OX 3 0 BW, UK, 1986., 1986

where $\mathbf{u}$ is the displacement vector and $\boldsymbol{\theta}$ is the microrrotations vector, and where: c_1 represents the phase/group speed for the longitudinal wave (P) that is non-dispersive as in the classical case, c_2 represents the high-frequency limit phase/group speed for a transverse wave (S) that is dispersive unlike the classical counterpart, c_3 represents the high-frequency limit phase/group speed for a longitudinal-rotational wave (LR) with a corkscrew-like motion that is dispersive and does not have a classical counterpart, c_4 represents the high-frequency limit phase/group speed for a transverse-rotational wave (TR) that is dispersive and does not have a classical counterpart, Q represents the cut-off frequency for rotational waves appearance, and K quantifies the difference between the low-frequency and high-frequency phase/group

speed for the S-wave. These parameters are defined by:

$$
\begin{aligned}
c_1^2 &= \frac{\lambda + 2\mu}{\rho}, \quad c_3^2 = \frac{\beta + 2\eta}{J}, \\
c_2^2 &= \frac{\mu + \alpha}{\rho}, \quad c_4^2 = \frac{\eta + \varepsilon}{J}, \\
Q^2 &= \frac{2\alpha}{J}, \quad K^2 = \frac{2\alpha}{\rho},
\end{aligned}
$$

To identify types of propagating waves that can arise in the micropolar medium it is convenient to expand the displacement and rotation vectors in terms of scalar and vector potentials

$$
\begin{aligned}
\mathbf{u} &= \nabla\phi + \nabla \times \mathbf{\Gamma}, \\
\boldsymbol{\theta} &= \nabla\tau + \nabla \times \mathbf{E},
\end{aligned}
$$

subject to the conditions:

$$
\begin{aligned}
\nabla \cdot \mathbf{\Gamma} &= 0 \\
\nabla \cdot \mathbf{E} &= 0.
\end{aligned}
$$

Using the above in the displacements equations of motion yields the following equations, after some manipulations

$$
\begin{aligned}
c_1^2 \nabla^2 \phi &= \frac{\partial^2 \phi}{\partial t^2}, \\
c_3^2 \nabla^2 \tau - 2Q^2 \tau &= \frac{\partial^2 \tau}{\partial t^2}, \\
\begin{bmatrix} c_2^2 \nabla^2 & K^2 \nabla \times, \\ Q^2 \nabla \times & c_4^2 \nabla^2 - 2Q^2 \end{bmatrix} \begin{Bmatrix} \mathbf{\Gamma} \\ \mathbf{E} \end{Bmatrix} &= \frac{\partial^2}{\partial t^2} \begin{Bmatrix} \mathbf{\Gamma} \\ \mathbf{E} \end{Bmatrix},
\end{aligned}
$$

where we can see that the equations for the scalar potentials are uncoupled, while the ones for the vector potentials are coupled.

Writing the vector potentials as plane waves of amplitude $\mathbf{A}$ and $\mathbf{B}$, wave number κ and circular frequency ω that propagate along the (x) axis,

$$
\begin{aligned}
\mathbf{\Gamma} &= \mathbf{A} \exp(i\kappa x - i\omega t) \\
\mathbf{E} &= \mathbf{B} \exp(i\kappa x - i\omega t).
\end{aligned}
$$

We can do these calculations using some the functions available functions in the package.

```
from sympy import Matrix, diff, symbols, exp, I, sqrt
from sympy import simplify, expand, solve, limit
from sympy import init_printing, pprint, factor
from continuum_mechanics.vector import lap_vec, curl, div

A1, A2, A3, B1, B2, B3 = symbols("A1 A2 A3 B1 B2 B3")
kappa, omega, t, x = symbols("kappa omega t x")
c1, c2, c3, c4, K, Q = symbols("c1 c2 c3 c4 K Q", positive=True)
```

We define the vector potentials $\mathbf{\Gamma}$ and $\mathbf{E}$.

```
Gamma = Matrix([A1, A2, A3]) * exp(I*kappa*x - I*omega*t)
E = Matrix([B1, B2, B3]) * exp(I*kappa*x - I*omega*t)
```

And compute the equations using the vector operators. Namely, the Laplace (`vector.lap_vec`) and curl (`vector.curl`) operators.

```
eq1 = c2**2 * lap_vec(Gamma) + K**2*curl(E) - Gamma.diff(t, 2)
eq2 = Q**2 * curl(Gamma) + c4**2*lap_vec(E) - 2*Q**2*E - E.diff(t, 2)
eq1 = simplify(eq1/exp(I*kappa*x - I*omega*t))
eq2 = simplify(eq2/exp(I*kappa*x  - I*omega*t))
eq = eq1.col_join(eq2)
```

We can compute the matrix for the system using `.jacobian()`

```
M = eq.jacobian([A1, A2, A3, B1, B2, B3])
M
```

$$\begin{bmatrix} -c_2^2\kappa^2+\omega^2 & 0 & 0 & 0 & 0 & 0 \\ 0 & -c_2^2\kappa^2+\omega^2 & 0 & 0 & 0 & -iK^2\kappa \\ 0 & 0 & -c_2^2\kappa^2+\omega^2 & 0 & iK^2\kappa & 0 \\ 0 & 0 & 0 & -2Q^2-c_4^2\kappa^2+\omega^2 & 0 & 0 \\ 0 & 0 & -iQ^2\kappa & 0 & -2Q^2-c_4^2\kappa^2+\omega^2 & 0 \\ 0 & iQ^2\kappa & 0 & 0 & 0 & -2Q^2-c_4^2\kappa^2+\omega^2 \end{bmatrix}$$

And, we are interested in the determinant of the matrix M.

```
factor(M.det())
```

$$(c_2\kappa-\omega)\,(c_2\kappa+\omega)\left(2Q^2+c_4^2\kappa^2-\omega^2\right)\left(-K^2Q^2\kappa^2+2Q^2c_2^2\kappa^2-2Q^2\omega^2+c_2^2c_4^2\kappa^4-c_2^2\kappa^2\omega^2-c_4^2\kappa^2\omega^2+\omega^4\right)^2$$

The roots for this polynomial (in ω^2) represent the dispersion relations. We can show them with the following snippet

```
disps = solve(M.det(), omega**2)
for disp in disps:
display(disp)
```

with the following result.

$$c_2^2\kappa^2$$

$$2Q^2 + c_4^2\kappa^2$$

$$Q^2 + \frac{c_2^2\kappa^2}{2} + \frac{c_4^2\kappa^2}{2} - \frac{1}{2}\sqrt{4K^2Q^2\kappa^2 + 4Q^4 - 4Q^2c_2^2\kappa^2 + 4Q^2c_4^2\kappa^2 + c_2^4\kappa^4 - 2c_2^2c_4^2\kappa^4 + c_4^4\kappa^4}$$

$$Q^2 + \frac{c_2^2\kappa^2}{2} + \frac{c_4^2\kappa^2}{2} + \frac{1}{2}\sqrt{4K^2Q^2\kappa^2 + 4Q^4 - 4Q^2c_2^2\kappa^2 + 4Q^2c_4^2\kappa^2 + c_2^4\kappa^4 - 2c_2^2c_4^2\kappa^4 + c_4^4\kappa^4}$$